UNIVERSITÁ DEGLI STUDI DI CATANIA

Facoltà di Scienze Matematiche, Fisiche e Naturali
Dipartimento di Matematica ed Informatica

Tesi di Dottorato di Ricerca in Matematica
per la Tecnologia
(XXII Ciclo)

DANILA SCANDURA

Physical-Mathematical modeling and numerical simulations of stress-strain state in seismic and volcanic regions

Coordinator:
Prof. Giovanni Russo

Tutors:
Prof. Giovanni Russo
Dr. Ciro Del Negro

To my family

Acknowledgements

A sincere thank goes to my tutor and Ph.D. school coordinator Prof. Giovanni Russo who, first, gave me the chance to spread my wings toward research and who always represents for me a sample of scientific rigor and devotion.

I would like to express my gratitude to my tutor Dr. Ciro Del Negro for giving me the opportunity to work in the interesting area of Volcano Geophysics and for his guidance, support, and advice throughout these studies.

I am indebted to “Istituto Nazionale di Geofisica e Vulcanologia” for providing the financial support throughout the Ph.D..

I can not forget the professional and personal support that Dr. Paul Lundgren and the Solid Earth Group staff gave me at Jet Propulsion. Laboratory. They represented a strong stimulus and inspiration in this research activity.

I am grateful to the members of the research groups of the the “Unità Funzionale Gravimetria e Magnetismo” at INGV for their support and their comradeship; especially to Eng. Gilda Currenti for her useful

assistance. Whenever I had problems in my research she was always there to help me.

I would like to thanks my family; my parents Giovanni and Rosa, and my brother Giuseppe to be always ready to encourage me.
A very special thanks to Salvo, my boyfriend.

Contents

List of tables

List of Figures

Chapter 1

Foreword

The strain-stress state generated by faulting or cracking and influenced by the strong heterogeneity of the internal earth structure precedes and accompanies volcanic and seismic activity. Particularly, volcanic eruptions are the culmination of long and complex geophysical processes and physical processes which involve the generation of magmas in the mantle or in the lower crust, its ascent to shallower levels, its storage and differentiation in shallow crustal chambers, and, finally, its eruption at the Earth's surface. Instead, earthquakes are a frictional stick-slip instability arising along pre-existing faults within the brittle crust of the Earth. Long-term tectonic plate motion causes stress to accumulate around faults until the frictional strength of the fault is exceeded.

The study of these processes has been traditionally carried out through different geological disciplines, such as petrology, structural geology, geochemistry or sedimentology. Nevertheless, during the last two decades, the development of physical of earth as well as the introduction of new powerful numerical techniques has progressively converted geophysics into a multidisciplinary science. Nowadays,

scientists with very different background and expertises such as geologist, physicists, chemists, mathematicians and engineers work on geophysics. As any multidisciplinary field, it has been largely benefited from these collaborations. The different ways and procedures to face the study of volcanic and seismic phenomena do not exclude each other and should be regarded as complementary.

Nowadays, numerical modeling in volcanology covers different pre-eruptive, eruptive and post-eruptive aspects of the general volcanic phenomena. Among these aspects, the pre-eruptive process, linked to the continuous monitoring, is of special interest because it contributes to evaluate the volcanic risk and it is crucial for hazard assessment, eruption prediction and risk mitigation at volcanic unrest. large faults. The knowledge of the actual activity state of these sites is not only an academic topic but it has crucial importance in terms of public security and eruption and earthquake forecast.

However, numerical simulation of volcanic and seismic processes have been traditionally developed introducing several simplifications: homogeneous half-space, flat topography and elastic rheology. These simplified assumptions disregards effects caused by topography, presence of medium heterogeneity and anelastic rheology, while they could play an important role in Moreover, frictional sliding of a earthquake generates seismic waves that travel through the earth, causing major damage in places nearby to the modeling procedure

This thesis presents mathematical modeling and numerical simulations of volcanic and seismic processes. The subject of major interest has been concerned on the developing of mathematical formulations to describe seismic and volcanic process. The interpretation of geophysical parameters requires numerical models and algorithms to define the optimal source parameters which justify

observed variations. In this work we use the finite element method that allows the definition of real topography into the computational domain, medium heterogeneity inferred from seismic tomography study and the use of complex rheologies. Numerical forward method have been applied to obtain solutions of ground deformation expected during volcanic unrest and post-seismic phases, and an automated procedure for geodetic data inversion was proposed for evaluating slip distribution along surface rupture.

1.1 Objectives

The main goal of geophysical modeling is to deduce information about the subsurface distribution of physical properties taking advantage from physical measurements: this represents the Geophysical Inverse Problem. A crucial point in the geophysical inverse problem is to derive a mathematical relationship that relates observations and model (forward model). In this thesis, we deal with two main classes of forward model: the analytical and the numerical models.

Elaborated inverse methods typically combine forward models with appropriate algorithms to find the best parameter set that minimizes the misfit between the model values and the observations by means of an objective function. This turns the inversion problem in an optimization problem. Since considered models are highly non-linear and characterized by several parameters, the geophysical

inverse problem requires sophisticated identification techniques to be solved.

Analytical forward model, because of the low computational cost, are well suitable for identifications techniques allowing the simultaneous inversion of combined models hence the joint interpretation of multimethod geophysical data. The drawbacks of the analytical formulations for modeling volcanic and seismic activities are the assumption of simple geometries for the sources embedded in homogeneous elastic half-space. Nevertheless natural characteristics of volcanic and seismic areas such as topography or lateral variations of rheological properties may have great influence on the observed signals: such complexities can be treated using numerical methods.

Over the last decades numerical modeling of many kinds of volcanic and tectonic processes has been applied on a wide range of geological problems (Cloetingh et al. 1998). This range covers among others stress, strain, extension, compression, basin evolution, sedimentation. Depending on the purpose of the study, different numerical concepts and techniques have been applied. The most adequate method to calculate stress and strain and hence deriving associated geophysical signals changes in a given material is the finite element method (FEM).

The aim of this thesis is, starting from the simplified analytical geophysical problem, to reach the more realistic numerical geophysical forward and inverse problem. To this purpose the analytical studies are a precious resource to retrieve position and shape of volcanic sources. Then these results are used for the calibration and application of the FE numerical model. Indeed the FEM should provide a more precise description including realistic

features for the source shape, the topographic relief, the elastic medium heterogeneities and the anelastic rheologies.

The preferred scenario for volcanic studies is Mt. Etna being among the most intensively monitored volcano in the world, so offering a lot of case studies for the application of the proposed models. A good setting for seismic analysis is instead the tectonically active eastern California shear zone, that is believed to accommodate about 15% of the relative motion between the North American and Pacific plates. If proffer the application of the ground deformation models thanks to the dense remote measurement networks that form high-resolution maps of earthquake-induced surface deformation .

1.2 Structure of the Thesis

This is an interdisciplinary thesis and, therefore, deals with topics that are commonly treated within different scientific disciplines. The idea is to write a modular thesis in which each chapter could be read as an independent self-consistent unit, avoiding unnecessary crossed references between chapters.

The work is organized as follows:

Chapter 2. *Governing equations for ground deformation*

This chapter develops the governing equations that describe different behaviours of medium stress response. It provide an overview of the principal rheologies, elastic, viscoelastic and elastoplastic one, with the aim to establish basic relationship between

kinematic and dynamic quantities for continuous media, to analyse their meaning and implications, and to make use of their consequences.

Chapter 3. *Numerical Methods*

This chapter is an overview of several numerical method: the Finite Element Method (FEM), the Finite Volume Method (FVM), and the Boundary Element Method (BEM). Particularly this different numerical approaches were shown by the investigation of an elliptic boundary value problem that hold the mechanic and thermal equations we will found in this thesis. For each of these methods, we illustrated some specific advantages and disadvantages.

Chapter 4. *Forward FE Modeling*

This chapter presents the advantages within the usage of numerical forward models. A comparison between analytical approaches and numerical solutions is performed. The comparison allows to quantify the error implicit in the analytical solutions and constrains the range of applicability of these widely used procedures. Several numerical models were also conducted to appreciate how the complex distribution of elastic medium parameters, the topography and rheological properties make the numerical results differ from the simple analytical solutions.

Chapter 5. *Modeling of ground deformation*

This model presents some numerical simulations of ground deformation in volcanic and seismic areas. It first reviews some fundamental concepts of volcanology and seismology then goes

through several real cases study. Firstly, the numerical modeling procedure is applied into a volcanic area to study the ground deformation observed during the 2001 Etna eruption and during the 1993-1997 inflation phase occurred on Etna volcano. Secondly, the procedure was applied in a seismic area to analyze the long term deformation following both the M. 7.3 1992 Landers and M. 7.1 1999 Hector Mine Californian earthquakes.

Chapter 6. *FEM-based inversion procedure*

In this chapter a geodetic inversion procedure for the estimate of the slip distribution along a fault is presented. This algorithm employs the Green's function computations in a 3D FE model and account for topographic effects as well as a complicated distribution of material properties. A number of tests on synthetically generated data were presented to assess the performance and the implication of the inversion procedure.

Chapter 7. *A Fem-based fault slip inversion using InSAR data*

A case study for the FEM inversion scheme was reported to better characterize the Pernicana fault movement, one of the most active structures at Mt Etna, and its role in the 2002-2003 Etna eruption. The method allows to invert geodetic data through a FE model giving a very detailed picture of the heterogeneous slip distribution on fault planes involved in volcanic and tectonic events.

Chapter 8. *Conclusion*

The last chapter points out which are the original contributions of this thesis, summarizes the conclusions, and indicates which should be the future lines of research.

Chapter 2

Governing equations for ground deformation

The motion and deformation of rocks are processes of fundamental importance in shaping the Earth, from the outer crustal layers to the deep mantle. Reconstructions of the behaviour of the earth therefore require detailed knowledge of the geometry of deformation structures and their relative timing, of the motions leading to deformation structures and of the mechanism governing these motions. Since 1960s, the emphasis has been more on the mechanisms behind structure development and on the role of the rheological of rocks during deformation with the framework of large-scale tectonics. An understanding of rheology is therefore a prerequisite for the quantitative study of several geological and geophysical phenomena. Indeed, mechanical and thermal processes in geology cannot be unravelled without an appreciation of rheology, and

consequently the latter forms a fundamental part of geophysics and geodynamics.

This chapter provides a mathematical formulation of the basic laws of continuum mechanics. These equations reflect three fundamental physical principles: mass conservation, Newton's second law and the first law of the thermodynamics. As applications of these laws, the behaviors of certain material idealizations (models) including the elastic, viscoelastic and materials, are presented with the aim to establish basic relationship between kinematic and dynamic quantities, to analyse their meaning and implications, and to make use of their consequences.

2.1 Governing equations

Continuum mechanics deals with the behavior of materials that can be approximated as continuous for certain length and time scales. The equations that govern the mechanics of such materials include the balance laws for mass, momentum, and energy (Fung, 1977). This section presents the equations founded by applying the law of conservation of linear momentum, that is, Newton's second law, to the rock.

2.1.1 Equations of stress equilibrium

In order to find the state of stress and displacement that results from the application of certain loads or boundary displacement, it is necessary to solve a set of three coupled partial differential equations

known as “equations of stress equilibrium”. These equations are found by using the Newton’s second law.

Newton’s second law states that the total force applied to a body in a given direction is equal to the mass of the body multiplied by its acceleration in that direction. As there are three mutually orthogonal directions at any point in a rock mass, there will be three independent equations of motion. To derive the mathematical form of these the laws of motion/equilibrium, consider an arbitrarily shaped body of finite size. We denote the region of three-dimensional space occupied by the body by $\boldsymbol{B}$ and the outer boundary of the body by $\partial\boldsymbol{B}$. The total force acting on this body in, say, the x direction, consists of the sum of all the body forces that act over the internal portions of the body, plus the resultant force due to all of the surface tractions that act over the outer boundary of the body.

If we let F_x be the body force, per unit mass, which acts at each element of the rock, then ρF_x is the body force per unit of volume, and so the total body force is found by integrating the local body force over the entire body:

$$\iiint_B \rho F_{\mathbf{x}} dV \,. \tag{2.1}$$

To be consistent with the traditional rock mechanics sign conventions, the components of F_x, namely $(F_x, F_y, F_z)_x$, must be considered to be positive numbers if they act in the negative coordinate directions.

The total resultant of all of the surface tractions that are applied over the outer boundary of the body is found by integrating the surface tractions over the outer boundary:

$$\iint_{\partial B} p_{\mathbf{x}}\, dA. \tag{2.2}$$

The x-component of the acceleration of each small element of rock is given by the second derivative with respect to time u_x, the x-component of the displacement. The mass of each small element of rock is given by ρdV, where dV is the incremental volume. The total x-component of the inertia term is therefore found by integrating the product of mass and acceleration over the entire body:

$$\iiint_{B} \rho \frac{\partial^2 u}{\partial t^2}\, dV\,. \tag{2.3}$$

Equating the total force to the total inertia term yields

$$\iiint_{B} \rho F_{\mathbf{x}}\, dV + \iint_{\partial B} p_{\mathbf{x}}\, dA = \iiint_{B} \rho \frac{\partial^2 u}{\partial t^2}\, dV\,. \tag{2.4}$$

Equation (2.4) expresses Newton's law of motion in the x-direction, in an integral form. To derive the more useful differential form of this equation, we first convert the surface integral into a volume integral over the entire body. To do this, we invoke the divergence theorem , which states that (Kellogg, 1970, Lang, 1973) for any vector $\mathbf{f}_x$ with components $(f_x, f_y, f_z)_x$

$$\iint_{\partial B} (f_x n_x + f_y n_y + f_z n_z)\, dA = \iiint_{B} \left(\frac{\partial f_x}{\partial x} + \frac{\partial f_y}{\partial x} + \frac{\partial f_z}{\partial x} \right) dV\,. \tag{2.5}$$

Where (n_x, n_y, n_z) are the components of the outward unit normal vector to the surface. The applicability of the divergence theorem requires certain assumptions about the differentiability of the functions in the integrand and smoothness of the outer boundary $\partial \boldsymbol{B}$; we will always assume that these conditions hold.

To apply the divergence theorem to the surface integral in Equation (2.4), we first express the traction in terms of the stress components:

$$\iint_{\partial B} p_{\mathbf{x}} dA = \iint_{\partial B} (\sigma_{xx} n_x + \sigma_{yx} n_y + \sigma_{zx} n_z) dA \tag{2.6}$$

Application of the divergence theorem to (2.6) now yields

$$\begin{aligned} &\iint_{\partial B} p_{\mathbf{x}} dA = \iint_{\partial B} (\sigma_{xx} n_x + \sigma_{yx} n_y + \sigma_{zx} n_z) dA = \\ &= \iiint_B \left(\frac{\partial \sigma_{xx}}{\partial x} + \frac{\partial \sigma_{yx}}{\partial y} + \frac{\partial \sigma_{zx}}{\partial z} \right) \end{aligned} \tag{2.7}$$

Substitution of Equation (2.7) into Equation (2.4) gives

$$\begin{aligned} &\iiint_B \rho F_x dV + \iiint_B \left(\frac{\partial \sigma_{xx}}{\partial x} + \frac{\partial \sigma_{yx}}{\partial y} + \frac{\partial \sigma_{zx}}{\partial z} \right) \\ &= \iiint_B \rho \frac{\partial^2 u}{\partial t^2} dV \end{aligned} , \tag{2.8}$$

Which can be written as

$$\iiint_B \left[\frac{\partial \sigma_{xx}}{\partial x} + \frac{\partial \sigma_{yx}}{\partial y} + \frac{\partial \sigma_{zx}}{\partial z} + \rho F_x - \rho \frac{\partial^2 u}{\partial t^2} \right] dV = 0 , \tag{2.9}$$

Equation (2.9) must hold for any arbitrary subregion of the rock mass, because Newton's law of motion applies to any arbitrary region, the integrand must be identically zero at all points of the rock mass. To prove this, assume that there is some point x at which the integrand is positive rather than zero. By continuity, it would then also be positive in some small neighborhood of x. We could then chose this small neighborhood as our region of integration, in which case the integral will be positive (in contradiction to Equation (2.9)). Hence, our assumption that the integrand is positive at point x must have been incorrect. We conclude that, at all points of the rock mass,

$$\frac{\partial \sigma_{xx}}{\partial x} + \frac{\partial \sigma_{yx}}{\partial y} + \frac{\partial \sigma_{zx}}{\partial z} + \rho F_x = \rho \frac{\partial^2 u}{\partial t^2} , \tag{2.10}$$

Similar applications of Newton's second law in the *y* and *z* directions yield

$$\frac{\partial \sigma_{xy}}{\partial x} + \frac{\partial \sigma_{yy}}{\partial y} + \frac{\partial \sigma_{zy}}{\partial z} + \rho F_y = \rho \frac{\partial^2 v}{\partial t^2} , \tag{2.11}$$

$$\frac{\partial \sigma_{xz}}{\partial x} + \frac{\partial \sigma_{yz}}{\partial y} + \frac{\partial \sigma_{zz}}{\partial z} + \rho F_z = \rho \frac{\partial^2 w}{\partial t^2} \tag{2.12}$$

These three equations of motion are coupled together, since each of the shear stresses appears in two of the equations.

The equations of motion, (2.10)-(2.12) can be expressed in vector/matrix form by first recognizing that the gradient operator can be thought of as a 3 × 1 column vector, that is,

$$\nabla = \begin{bmatrix} \dfrac{\partial}{\partial x} \\ \dfrac{\partial}{\partial y} \\ \dfrac{\partial}{\partial z} \end{bmatrix}. \tag{2.13}$$

If we premultiply the stress matrix by the transpose of this gradient vector, the result is a 1 × 3 vector whose three components are given by the derivative terms in Equations (2.10)-(2.12), as can easily verify. Hence, Equations (2.10)-(2.12) can also be written as

$$\nabla \cdot \boldsymbol{\sigma} + \rho \mathbf{F} = \rho \frac{\partial^2 \mathbf{u}}{\partial t^2}, \tag{2.14}$$

Where we identify F and u as 1 × 3 row vectors, rather than 3 × 1 column vectors. The term $\nabla\boldsymbol{\sigma}$ is often referred to as "div$\boldsymbol{\sigma}$". If we let a superposed dot denoted differentiation with respect to time, the equations of motion can be written succinctly as

$$div\boldsymbol{\sigma} + p\mathbf{F} = \rho\ddot{\mathbf{u}}, \tag{2.15}$$

The set of three equations expressed by Equations (2.10)-(2.12), (2.14), or Equation (2.15), must be satisfied at all times, at all points in

the rock mass, and are therefore the governing equations for rock deformation.

However, six unknown stresses components and three unknown displacements appear in these equations, so these three equations are in themselves not sufficient to enable the stresses and displacements to be found. In order to have a mathematically well-posed problem, there must be an equal number of equations and unknowns. The strain-displacement relations provide six additional equations, but also introduce six additional unknowns, the six independent components of the strain tensor. An additional six equations are then supplied by the stress-strain law, which may be of any form: linearly elastic, viscoelastic, plastic, etc. The equations of motion, along with the strain-displacement relations and the stress-strain relations, constitute a set of equations in which the number of unknowns is equal to the number of equations. This is a necessary, but not sufficient, condition for a problem in rock mechanics to be mathematically well posed.

In the frequently occurring case in which the rock is in static equilibrium, or in which the displacements are occurring very slowly, the right-hand sides of Equations (2.10)-(2.12) can be neglected. In this cases, the equations of motion reduce to the equations of equilibrium (Jaeger et al., 2007):

$$\frac{\partial \sigma_{xx}}{\partial x}+\frac{\partial \sigma_{yx}}{\partial y}+\frac{\partial \sigma_{zx}}{\partial z}+\rho F_x=0, \tag{2.16}$$

$$\frac{\partial \sigma_{xy}}{\partial x}+\frac{\partial \sigma_{yy}}{\partial y}+\frac{\partial \sigma_{zy}}{\partial z}+\rho F_y=0, \tag{2.17}$$

$$\frac{\partial \sigma_{xz}}{\partial x}+\frac{\partial \sigma_{yz}}{\partial y}+\frac{\partial \sigma_{zz}}{\partial z}+\rho F_z=0 \tag{2.18}$$

2.2 Material modeling.

Governing equations of continuous medium need to be complemented with additional constitutive equations and state laws in order to fully describe the physics of any particular continuous medium. We analyzed the physics of elastic, viscoelastic and elastoplastic medium.

2.2.1 Linear elastic material

One of the most important rheological classes is elasticity, in which the stress is linearly proportional to the strain and the latter is fully recoverable. Rocks are approximately elastic at low pressure and temperature and also in the bulk of the Earth for stresses at seismic frequencies.

If we assume that rocks is a linear elastic material equations of stress equilibrium (2.16)-(2.18) can be expressed in terms of the displacements. We first combine the elastic strain-displacement relations

$$\varepsilon = \frac{1}{2}\left[\nabla \cdot \mathbf{u} + (\nabla \cdot \mathbf{u})^T\right], \tag{2.19}$$

and the elastic stress-strain relations, namely Hooke's law

$$\sigma_{ij} = 3K\left(\frac{1}{3}\varepsilon_{kk}\delta_{ij}\right) + 2G\left(\varepsilon_{ij} - \frac{1}{3}\varepsilon_{kk}\delta_{ij}\right), \tag{2.20}$$

where K is the bulk modulus and G is the shear modulus.
Then, substituting the result into the equations of motion, (2.10)-(2.12), to find

$$\lambda\left(\frac{\partial^2 u}{\partial x^2} + \frac{\partial^2 v}{\partial x \partial y} + \frac{\partial^2 w}{\partial x \partial z}\right) + G\left(\frac{\partial^2 u}{\partial x^2} + \frac{\partial^2 v}{\partial x \partial y} + \frac{\partial^2 w}{\partial x \partial z} + \right.$$
$$\left. + \frac{\partial^2 u}{\partial x^2} + \frac{\partial^2 u}{\partial y^2} + \frac{\partial^2 u}{\partial z^2}\right) + \rho F_x = 0 \tag{2.21}$$
$$\lambda\left(\frac{\partial^2 u}{\partial x \partial y} + \frac{\partial^2 v}{\partial y^2} + \frac{\partial^2 w}{\partial y \partial z}\right) + G\left(\frac{\partial^2 u}{\partial x \partial y} + \frac{\partial^2 v}{\partial x^2} + \frac{\partial^2 w}{\partial y x \partial z} + \right.$$
$$\left. + \frac{\partial^2 v}{\partial x^2} + \frac{\partial^2 v}{\partial y^2} + \frac{\partial^2 v}{\partial z^2}\right) + \rho F_y = 0, \tag{2.22}$$
$$\lambda\left(\frac{\partial^2 u}{\partial x \partial z} + \frac{\partial^2 v}{\partial y \partial z} + \frac{\partial^2 w}{\partial z^2}\right) + G\left(\frac{\partial^2 u}{\partial z \partial x} + \frac{\partial^2 v}{\partial y \partial z} + \frac{\partial^2 w}{\partial z^2} + \right.$$
$$\left. + \frac{\partial^2 w}{\partial x^2} + \frac{\partial^2 w}{\partial y^2} + \frac{\partial^2 w}{\partial z^2}\right) + \rho F_z = 0 \tag{2.23}$$

Equations (2.21)-(2.23), known as the Navier equations, embody the equations of stress equilibrium, the stress-strain equations, and the strain-displacement identities. Assuming that the body forces are known these are equations for the three unknown displacements. As such, they form a set of differential equations that can be used to solve elasticity problems.

The displacement form of the equilibrium equations can also be expressed in a more compact vector-matrix notation. Identities (2.21)-(2.23) can be written in the following hybrid form involving both scalar and vector notation:

$$(\lambda + G)\frac{\partial}{\partial x}(\nabla \cdot \mathbf{u}) + G\nabla^2 u + \rho F_x = 0 \tag{2.24}$$

$$(\lambda + G)\frac{\partial}{\partial y}(\nabla \cdot \mathbf{u}) + G\nabla^2 u + \rho F_y = 0 \tag{2.25}$$

$$(\lambda + G)\frac{\partial}{\partial z}(\nabla \cdot \mathbf{u}) + G\nabla^2 u + \rho F_z = 0 \tag{2.26}$$

From Equation (2.13), we see that the three partial derivative operators appearing in these three equations form the components of the gradient row vector. Furthermore,

$$(\nabla^2 u, \nabla^2 v, \nabla^2 w) = \nabla^2 (u, y, z) = \nabla^2 \mathbf{u}\,, \tag{2.27}$$

hence, (2.24)-(2.26) can be written as

$$(\lambda + G)\nabla(\nabla \cdot u) + G\nabla^2 u + \rho F = 0 \tag{2.28}$$

This form of the Navier equations not only has the advantage of compactness, but can also be generalized to any non Cartesian coordinate system, such as cylindrical coordinates, in which the explicit representation of the gradient, divergence and Laplacian operators are known.

Various important and useful general results can be found from the Navier equations. In situations in which there are no body forces,

taking the partial derivative of Equation (2.24) with respect to *x*, adding the results, and interchanging the order of partial differentiation when appropriate, leads to

$$(\lambda + 2G)\nabla^2(\nabla \cdot u) = 0 \tag{2.29}$$

Regarding that

$$\nabla \cdot u = \varepsilon_x \tag{2.30}$$

hence, in the absence of body forces, the volumetric strain satisfies Laplace's equation, that is,

$$\nabla^2 \varepsilon_x = 0 \tag{2.31}$$

Also the relationship

$$\sigma_m = \kappa \varepsilon_x \tag{2.32}$$

in which case Equation (2.31) implies that the mean normal stress also satisfies Laplace's equation:

$$\nabla^2 \sigma_m = 0 \tag{2.33}$$

Differentiation of (2.26) with respect to *x*, again with the body force taken to be zero, gives after interchanging the orders of some of the derivatives,

$$(\lambda + G)\frac{\partial^2 \varepsilon_x}{\partial x^2} + G\nabla^2 \varepsilon_{xx} = 0 \tag{2.34}$$

Invoking Equations (2.31), (2.33), and (2.20) leads to

$$\nabla^2 \tau_{xx} = -\frac{6(\lambda + G)}{3(\lambda + 2G)}\frac{\partial^2 \tau_m}{\partial x^2} = \frac{-3}{(1+\nu)}\frac{\partial^2 \tau_m}{\partial x^2} \tag{2.35}$$

With similar equations holding for the other two normal stresses. Likewise, it can be shown that

$$\nabla^2 \tau_{xy} + \frac{3}{(1+\nu)}\frac{\partial^2 \tau_m}{\partial x \partial y} = 0 \tag{2.36}$$

As well as two similar equations for the other two shear stresses. These six equations, known as the Behrami-Michell equations, are equivalent to the strain-compatibility equations, although they are expressed in terms of the stresses. If a purely stress-based formulation is desired for the elasticity equations, which is useful in cases where the boundary conditions are known in terms of stresses rather than displacement, the Behrami-Michell equations give a complete set of six equations for the six stresses. If a nonconstant body forces act on the rock, additional terms involving the derivates of the body force vector **F** appear on the right-hand sides of Equations (2.35) and (2.36). In situations in which the displacement components u and v depends only on x and y, and the strain in the z direction is constant with z, the stress equilibrium equations (2.16)-(2.18) reduce to the following pair of equations (Jaeger et al., 2007):

$$\frac{\partial \sigma_{xx}}{\partial x} + \frac{\partial \sigma_{yx}}{\partial y} + \rho F_x = 0\,, \tag{2.37}$$

$$\frac{\partial \sigma_{xy}}{\partial x} + \frac{\partial \sigma_{yy}}{\partial y} + \rho F_y = 0\,. \tag{2.38}$$

2.2.2 Linear viscoelastic material

Many material show time effects with a stage of transient creep between instantaneous (elastic) and steady-state (viscous) deformation. This behaviour can be modelled by linear rheological bodies, which can account for elastic afterworking and stress relaxation.

Most structural metals are nearly linear elastic under small strain, as measurement of load-displacement relationship reveal. The existence of normal modes of free vibrations which are simple harmonic in time, is often quoted as a indication of the linear elastic character of the material. However, when one realizes that the vibration of metal instruments does not last forever, even in the vacuum, it becomes clear that metals deviate somewhat from Hooke's law. Thus, other constitutive laws must be considered. For the classes of material which retains linearity between load and deflection, but the linear relationship depends on the time, the present state of deformation cannot be determined completely unless the entire history of loading is known. A linear elastic solid may be said to have a simple memory: it remembers only one configuration; namely, the unstrained natural state of the body. Many materials do not behave

this way: they remember the past. Among such materials with memory there is one class that is relatively simple in behaviour. This is the class of materials, named linear viscoelastic material, for which the cause and the effect are linearly related because the stress linearly depends on the strain and its time derivatives. In such a case, the rheological constitutive equation can be written as:

$$P(\sigma) = Q(\varepsilon) \tag{2.39}$$

where σ and ε are the stress and strain deviators respectively (Ivins and Sammis, 1996). P and Q are differential operators expressed as:

$$P = a_m \frac{\partial^m}{\partial t^m} + a_{m-1} \frac{\partial^{m-1}}{\partial t^{m-1}} + ... + a_0 \tag{2.40}$$

$$Q = b_m \frac{\partial^m}{\partial t^m} + b_{m-1} \frac{\partial^{m-1}}{\partial t^{m-1}} + ... + b_0 \tag{2.41}$$

where a_i and b_i come from the assumed material constants for $i = 0,...,m$.

For linear viscoelastic material is usually assumed that the viscous part of the deformation is incompressible, so that the volumetric strain is completely elastic and the viscoelastic deformation may be expressed purely in terms of deviatoric components.

To discuss the foregoing in concrete terms, let us consider a simple bar fixed at one end and subjected to a force in the direction of

the axis at the other end. Let the force on the bar at time t be $F(t)$ and A is its cross sectional area, then the stress is given by

$$\sigma(t) = \frac{F(t)}{A}. \tag{2.42}$$

Let $u(t)$ be the total elongation on the bar caused by the total history of the loading up to the time t. If the bar is extended by an amount $u(x)$ where $x = 0$ at one end of the bar, then the one-dimensional strain is defined as

$$\varepsilon = \frac{du}{dx}. \tag{2.43}$$

Therefore, the displacement in the bar can be expressed in terms of the strain as

$$u(x) = \varepsilon x \ \Rightarrow \varepsilon = \frac{u(l)}{l} = \frac{\Delta l}{l}, \tag{2.44}$$

where l is the length of the bar.

If the function $\sigma(t)$ is continuous and differentiable, then in a small time interval $d\tau$ at time τ the increment of stress is $(d\sigma/dt)d\tau$. This increment remains acting on the bar and contributes an element $d\varepsilon(t)$ to the strain at the time t, with a proportionality constant c depending on the time interval $t - \tau$. Hence, we may write

$$d\varepsilon(t) = c(t-\tau)\frac{dF}{dt}(\tau)d\tau . \tag{2.45}$$

Let the origin of time be taken at the beginning of motion and loading. Then, on summing over the entire history, we have

$$\varepsilon(t) = \int_0^t c(t-\tau)\frac{d\sigma}{dt}(\tau)d\tau . \tag{2.46}$$

A similar argument, with the role of F and u interchanged, gives

$$\sigma(t) = \int_0^t G(t-\tau)\frac{d\varepsilon}{dt}(\tau)d\tau . \tag{2.47}$$

These laws are linear, since a doubling of the load doubles the elongation, and viceversa.

Equations (2.43) and (2.44) are Boltzmann's formulation of the constitutive equation, in the case of a simple bar, for a material which has a linear load-deflection relationship. The function $G(t)$ is called relaxation function and can be measured as the stress when a material is held at a constant strain. This function is often approximated in a Prony series as shown in Equation (2.48)

$$G(t) = G_0\left[\mu_0 + \sum_{m=1}^{M}\mu_m e^{\frac{-t}{\tau_m}}\right], \tag{2.48}$$

$$\sum_{m=1}^{M} \mu_m = 1. \tag{2.49}$$

Here G_0, μ_m and τ_m are material constants.

The function $c(t)$ is called the creep function. They are characteristic functions of the material. Physically, $c(t)$ is the elongation produced by a sudden application at $t = 0$ of a constant force of magnitude unity.

It is generally accepted that the deformation at the present time t is due to stress that act in the past, and not in the future. This concept is expressed by the requirement that

$$c(t) = 0 \quad \text{for } t<0 \tag{2.50}$$

Similarly, by the same axiom

$$G(t) = 0 \quad for \;\; t < 0 \tag{2.51}$$

Of course, this non retroactivity is implied already when we write t for the upper limits of the integrals in Equations (2.46) and (2.47).

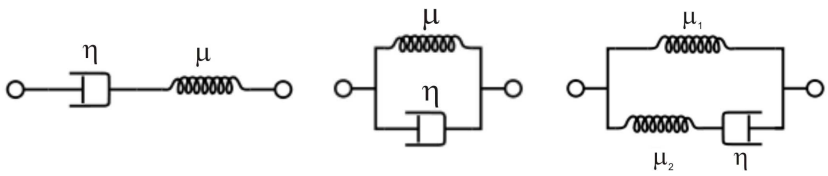

(a) (b) (c)

Figure 2.1. Analogical models of linear viscoelasticity: (a) Maxwell, (b) Voigt and (c) standard linear solid.

In Figure 2.1 are shown three mechanical models of material behaviour, namely, the Maxwell model, the Voigt model, and the standard linear model, all of which are composed of combinations of linear springs with spring constant μ and dashpots with coefficient of viscosity η. A linear spring is supposed to produce instantaneously a deformation proportional to the load. A dashpot is supposed to produce a velocity proportional to the load at any instant. The constitutive equations for these models are:

(i) Maxwell model

$$\dot{u} = \frac{\dot{F}}{\mu} + \frac{F}{\eta}, \tag{2.52}$$

(ii) Voigt model

$$F = \mu u + \eta \dot{u}, \tag{2.53}$$

(iii) Standard linear model

$$F + \tau_\varepsilon \dot{F} = E_R(u + \tau_\sigma \dot{u}),\ \tau_e F(0) = E_R \tau_\sigma u(0) \tag{2.54}$$

where τ_ε, τ_σ are two constants. When these equations are to be integrated, the initial conditions at $t = 0$ must be prescribed as indicated above.

The creep functions can be easily derived by solving Equations (2.34)-(2.36) for $u(t)$ when $F(t)$ is a unit-step function $\mathbf{1}(t)$. They are:

(i) Maxwell solid

$$c(t) = \left(\frac{1}{\mu} + \frac{1}{\eta}\right)\mathbf{1}(t), \tag{2.55}$$

(ii) Voigt solid

$$c(t) = \frac{1}{\mu}(1 - e^{-(\mu/\eta)t})\mathbf{1}(t), \tag{2.56}$$

(iii) Standard linear solid

$$c(t) = \frac{1}{E_R}\left[1 - \left(1 - \frac{\tau_\varepsilon}{\tau_\sigma}\right)e^{-t/\tau_\sigma}\right]\mathbf{1}(t), \tag{2.57}$$

where the unit-step function $\mathbf{1}(t)$ is defined as

$$\mathbf{1}(t)=\begin{cases}1 & when \quad t>0\\ 1/2 & when \quad t=0\\ 0 & when \quad t<0\end{cases}. \tag{2.58}$$

A body which obeys a load-deflection relation like that given by Maxwell's model is said to be a Maxwell solid, etc. Since a dashpot behaves as a piston moving in a viscous fluid, the above-named models are called models of viscoelasticity.

Interchanging the roles of σ and ε, we obtain the relaxation function as a response $\sigma(t)=G(t)$ corresponding to an elongation $u(t)=\mathbf{1}(t)$.

(i) Maxwell solid:

$$G(t)=\mu e^{-(\mu/\eta)t}\mathbf{1}(t) \tag{2.59}$$

(ii) Voigt solid:

$$G(t)=\eta\boldsymbol{\delta}(t)+\mu\mathbf{1}(t) \tag{2.60}$$

(iii) Standard linear solid:

$$G(t)=E_R\left[1-\left(1-\frac{\tau_\sigma}{\tau_\varepsilon}\right)e^{-t/\tau_\varepsilon}\right]\mathbf{1}(t). \tag{2.61}$$

Here we have used the symbol $\boldsymbol{\delta}$(t) to indicate the unit-impulse function, or Dirac-delta function, which is defined as a function with a singularity at the origin:

$$\boldsymbol{\delta}(t) = 0 \ \ for \ t < 0, \ and \ t > 0, \tag{2.62}$$

$$\int_{-\varepsilon}^{\varepsilon} f(t)\boldsymbol{\delta}(t)dt = f(0) \ \varepsilon > 0, \tag{2.63}$$

where *f(t)* is an arbitrary function continuous at t=0. These functions, *c(t)* and *G(t)*, are illustrated in Figures 2.2 and 2.3, respectively.

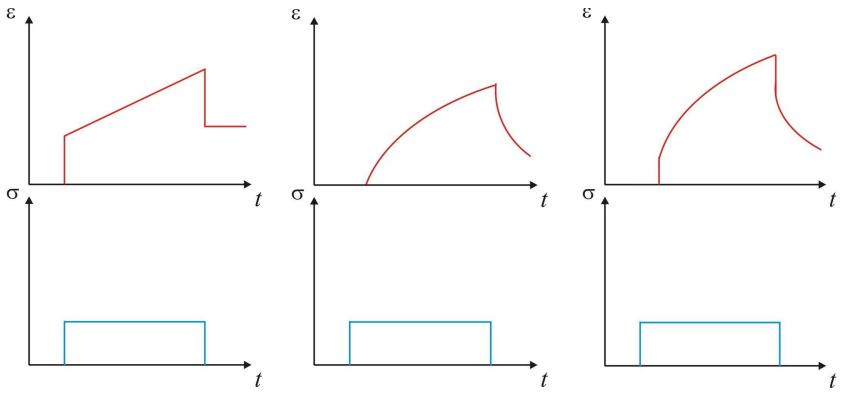

(a) (b) (c)

Figure 2.2. Creep function of (a) Maxwell, (b) Voigt, (c) standard linear solid. A negative phase is superposed at the time of unloading.

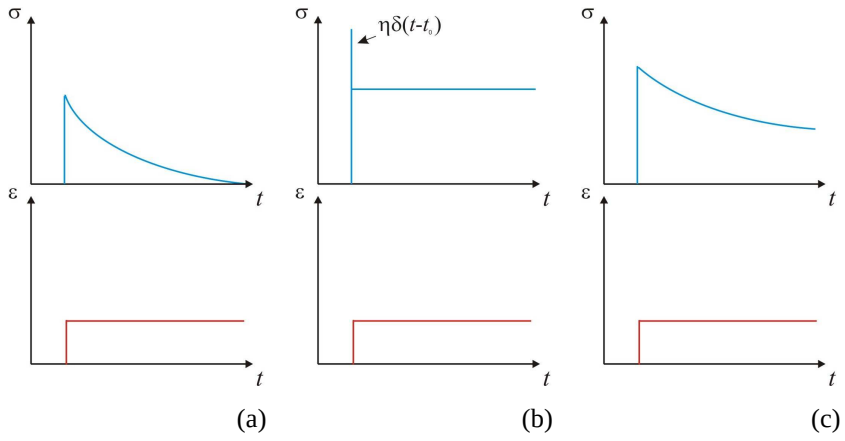

Figure 2.3. Relaxation function of (a) Maxwell, (b) Voigt, (c) standard linear solid.

For the Maxwell solid, a sudden application of a load induces an immediate deflection by the elastic spring, which is followed by creep of the dashpot. On the other hand, a sudden deformation produces an immediate reaction by the spring, which is followed by stress relaxation according to an exponential law (Equation (2.59) and Figure 2.2a). The factor η/μ, with dimensions of time, may be called a relaxation time: it characterized the rate of decay of the force.

For a Voigt solid, a sudden application of force will produce no immediate deflection because the dashpot, arranged in parallel with the spring, will not move instantaneously. Instead, as shown by Equation (2.60) and Figure 2.2b, a deformation will be gradually built up, while the spring takes a greater and greater share of the load. The dashpot displacement relaxes exponentially. Here the ratio η/μ is again a relaxation time: it characterizes the rate of decay of the deflection.

For the standard linear solid, a similar interpretation is applicable. The constant τ_ε is the time of relaxation of load under the condition of constant deflection (Equation 2.61), whereas the constant τ_σ is the time of relaxation of deflection under the condition of constant load (Equation 2.57). As $t \to \infty$, the dashpot is completely relaxed, and the load-deflection relation becomes that of the springs, as is characterized by the constant E_R in Equations (2.57) and (2.61). Therefore, E_R is called the relaxed elastic modulus.

Constitutive relations such as (2.62)-(2.54) were proposed to extend the classical theory of elasticity to include anelastic phenomena. The model shown in Figure 2.2c indentified with Equation (2.54) is called the standard linear model.

The most general form of the models described above is the Generalized Maxwell model also known as the Maxwell-Wiechert model. It takes into account that relaxation does not occur at a single time, but at a distribution of times. Due to molecular segments of different lengths with shorter ones contributing less than longer ones, there is a varying time distribution. The Generalized Maxwell model shows this by having as many spring-dashpot Maxwell elements as are necessary to accurately represent the distribution. Commonly the generalized Maxwell model is represented by a set of M Maxwell models in parallel (Figure 2.4).

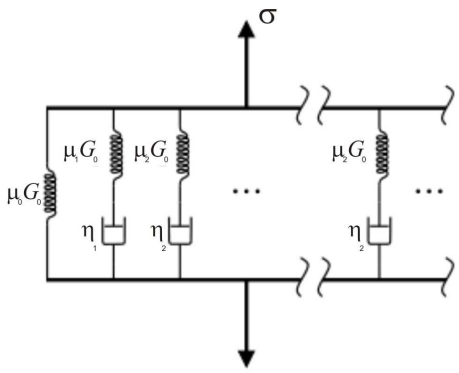

2

Figure 2.4. Analogical representation of Generalized Maxwell Model.

In this case, the constitutive equation may be written as

$$\sigma = 2G_0\left(\mu_0\varepsilon + \sum_{i=1}^{M}\mu_i q_i\right), \tag{2.64}$$

$$\sum_{i=0}^{M}\mu_i = 1, \tag{2.65}$$

where the variable q_i is the solution of differential equation:

$$\dot{q}_i + \frac{1}{\tau_i}q_i = \dot{e} \tag{2.66}$$

and where the instantaneous shear modulus is G_0, the long term shear modulus is $\mu_0 G_0$. The coefficient μ_i can be interpreted as the relative stiffness of the spring in branch i of the generalized Maxwell model.

Each time constant τ_i is the time constant of the spring-dashpot pair in the same branch. Following the analogy, the abstract variable q_i is the extension of the corresponding spring.

The material is completely defined by assigning the total shear modulus $G = E/2(1+\upsilon)$ (which is identical to the elastic shear modulus), the fractional shear moduli μ_i and the viscosity η_i for each spring element, leading to the relaxation times $\tau_i = \eta_i / G\mu_i$. It is not necessary to specify the fractional modulus μ_0, since it is obtained by subtracting the sum of the other ratios from one. A number of common material models may be obtained from the generalized Maxwell model by setting the shear moduli of various springs to zero, such as the Maxwell model (Fung, 1965; Ranalli, 1995, Zienkiewicz and Taylor, 1998).

2.2.3 Ideal plastic material

The rheological behaviour of solids depends on the level of deviatoric stress. When a critical stress is reached, the material fails, in either a brittle or a ductile manner. Failure can result either in discontinuous deformation (fracture), when the material shows loss of continuity along an approximately well-defined fracture surface, or an irrecoverable continuous deformation (plastic flow), when the material yields without any apparent loss of continuity. The critical stress (yield strength) and the mode of failure are functions of intrinsic and extrinsic rheological parameters. We examine the phenomenon of brittle shear failure with attendant plastic flow and present the ideal plastic model obeying von Mises' yielding criterion.

Metals obey Hooke's law only in a certain range of small strain. When a metal is strained beyond an elastic limit, Hooke's law no longer applies. The behaviour of metals beyond their elastic limit is rather complicated.

Generally, when the stress exceeds a critical value (the yield strength), the material will undergo plastic deformation. During an infinitesimal increment of stress, strain changes ε can be split up into elastic $\varepsilon^{(e)}$ and plastic $\varepsilon^{(p)}$ components:

$$d\varepsilon = d\varepsilon^{(e)} + d\varepsilon^{(p)} \tag{2.67}$$

The plastic strain increments are related to the yield function or yield surface F (Figure 2.5) that specifies the stress conditions required for plastic flow and prescribes the relations among stress components during flow. The yield surface F depends on the state of stress and strain and on the history of loading. Plastic strain can occur only if the stresses satisfy the general yield criterion:

$$F(\boldsymbol{\sigma}, \boldsymbol{\varepsilon}^p, \kappa) = 0 \tag{2.68}$$

where κ is a work hardening parameter defining the plastic deformation history of the material. If yielding occurs, we need further information concerning the increment or rate of deformation in order to complete the description of the material behavior. Drucker (1951) proved that the plastic strain increment vector must be normal to the yield surface at a regular point. The normality principle leads to the associated flow rule (i.e., the stress/strain relation):

$$d\varepsilon_{ij}^{\ p} = G\frac{\partial F}{\partial \sigma_{ij}}\frac{\partial F}{\partial \sigma_{kl}}d\sigma_{kl} \tag{2.69}$$

where

$$G = -\frac{1}{\left(\dfrac{\partial F}{\partial \varepsilon_{mn}^{p}} + \dfrac{\partial F}{\partial \kappa}\dfrac{\partial \kappa}{\partial \varepsilon_{mn}^{p}}\right)\dfrac{\partial F}{\partial \sigma_{mn}}} . \tag{2.70}$$

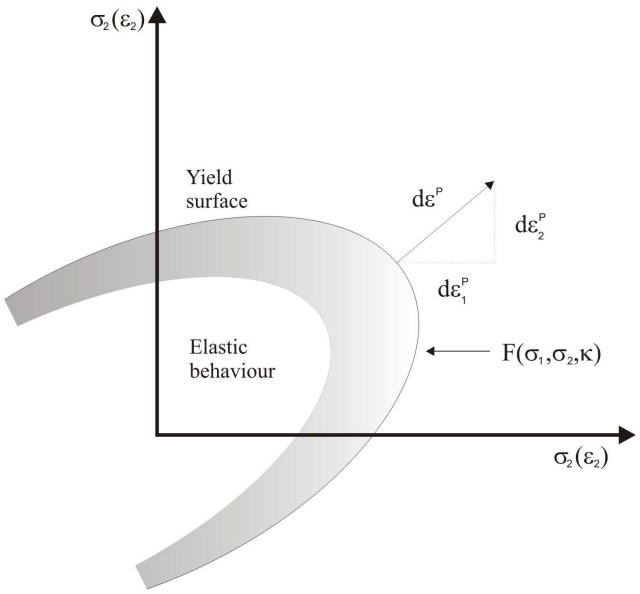

Figure 2.5. Yield surface and normality criterion in two-dimensional stress space

.

Different work hardening functions can be assumed on the basis of stress-strain relations fitting to experimental measurements on rocks. A few of the more common forms of hardening functions are the perfect plastic solid, the linear strain hardening solid and the power-law hardening solid (Figure 2.6).

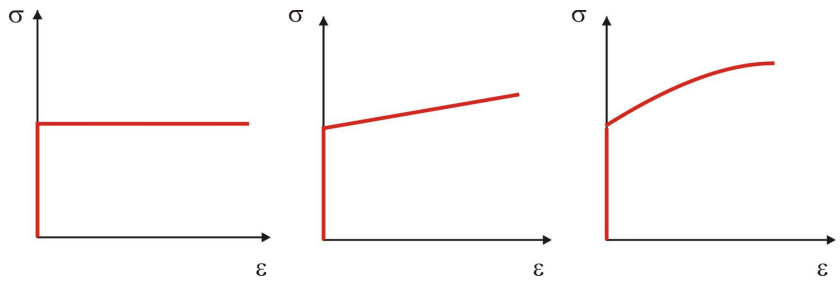

Figure 2.6. Examples of common types of hardening functions in the elastoplastc rheology: a) perfect plastic solid, b) Linear strain hardening solid and c) Power-law hardening solid.

We discuss the set of laws which defines the simplest of plastic materials: an ideal plastic solid obeying von Mises' yielding criterion. A perfectly plastic material neglects the effect of work hardening and the stress increments should lie on the yield surface. Among the several yield criteria that can be used to model plastic effects, a more general criterion has been proposed by von Mises. This criterion assumes that isotropic deformation is always related elastically to the mean pressure, while the deviatoric strain is elastically related to deviatoric stress until yielding is not reached, then plastic strain takes place at constant deviatoric stress.

Let J_2 the second invariant of the stress deviation σ'_{ij}

$$J_2 = \frac{1}{2}\sigma'_{ij}\,\sigma'_{ij}\,. \tag{2.71}$$

In a similar way, the strain deviation ε'_{ij} is defined by subtracting the mean strain from the strain tensor ε_{ij},

$$\varepsilon'_{ij} = \varepsilon_{ij} - \frac{1}{3}\varepsilon_{\alpha\alpha}\delta_{ij}\,. \tag{2.72}$$

If the material is isotropic and obeys Hooke's law, then

$$\varepsilon'_{ij} = \frac{1}{2G}\varepsilon'_{ij}\,. \tag{2.73}$$

When the elastic limit is reached, ε'_{ij} is no longer given by Hooke's law. In this case we define the plastic strain deviation as the actual strain deviation minus the strain deviation that would be computed if Hooke's law still applied. Let the plastic strain deviation be denoted by $\varepsilon^{(p)}_{ij}$,

$$\varepsilon^{(p)}_{ij} = \varepsilon'_{ij} - \frac{1}{2G}\sigma'_{ij}\,. \tag{2.74}$$

Then the total strain deviation may be written as

$$\varepsilon'_{ij} = \varepsilon_{ij}^{(p)} + \frac{1}{2G}\sigma'_{ij} . \tag{2.75}$$

If at each instant of time the rate of plastic deformation is $\dot{\varepsilon}_{ij}^{(p)}$, then the increment of plastic strain in the time interval dt is $\dot{\varepsilon}_{ij}^{(p)}dt$, and the total plastic strain deviation after successive stages of yielding will be the algebraic sum of the deformations that occur at all stages:

$$\varepsilon_{ij}^{(p)} = \varepsilon_{ij}^{(p)}(0) + \int_0^t \dot{\varepsilon}_{ij}^{(p)}(t)dt \tag{2.76}$$

where $\varepsilon_{ij}^{(p)}(0)$ is the initial value of $\varepsilon_{ij}^{(p)}$ at time *t=0*. A theory of plasticity is formulated by specifying how $\dot{\varepsilon}_{ij}^{(p)}$ can be computed.

For an ideal plastic solid obeying von Mises' yielding criterion and flow rule our specifications are as follows.

(a) Hooke's law holds for the mean stress and the mean strain at all times.

$$\sigma_{\alpha\alpha} = 3K\varepsilon_{\alpha\alpha} . \tag{2.77}$$

Hence, the plastic strain is compressible ($\varepsilon_{ij}^{(p)} = 0$) and the plastic strain deviation tensor is the same as the plastic strain tensor.

(b) The material is elastic and obeys Hooke's law as long as the second invariant J_2 is less than a constant k^2. In other words, no change in plastic strain can occur as long as $J_2<k^2$.

$$\dot{\varepsilon}_{ij}^{(p)} = 0 \ when \ J_2 < k^2 . \tag{2.78}$$

(c) Yielding can occur when and only when $J_2 = k^2$. When the yielding condition $J_2 - k^2 = 0$ prevails, the rate of change of the plastic strain is proportional to the stress deviation.

$$\dot{\varepsilon}_{ij}^{(p)} = \frac{1}{\mu}\sigma'_{ij}, \mu > 0 \tag{2.79}$$

where μ is a positive factor of proportionality which has the dimensions of the coefficient of viscosity of a fluid.

(d) Any stress state corresponding to $J_2 > k^2$ cannot be realized in the material.

The set of laws above contains two essential parts: the criterion for yielding, and the stress-strain relation in the elastic and plastic regimes. In the specifications above, the yielding condition is based on the second invariant of the stress deviation tensor, while the first invariant of deviatoric stress $I_1^{'} = \sigma'_{kk}$ is identically zero. The constant k can be identified with the yield stress of the material in simple shear and is independent of strain history (For a work hardening material, κ will be allowed to change with strain history) (Fung, 1965; Ranalli, 1995, Zienkiewicz and Taylor, 1998).

Chapter 3

Numerical methods

Differential equations are of vast interest in science and engineering since they provide mathematical models to a wide range of real world phenomena, such as mechanic deformations, heat transfer, and electromagnetic waves. Thus it is very appealing to try to gain insight into the world around us simply by solving various differential equations. Unfortunately solutions to differential equations can rarely be expressed by closed formulas. The differential equations that describe the physical phenomena can only be solved analytically for a very limited class of problems and even there only for simple geometries. More complex tasks require numerical approaches. Among these approaches, we should mention the Finite Element Method (FEM), the Finite Volume Method (FVM), and the Boundary Element Method (BEM), each of these methods with some specific advantages and disadvantages.

We will illustrate the different techniques by the investigation of an elliptic boundary value problem that hold the mechanic and thermal equations we will found in this thesis.

3.1. The Finite Element Method

FEM is a numerical technique which gives approximate solutions to differential equations that model problems arising in science and engineering. The FEM requires a problem defined in geometrical space (or domain) to be subdivided into a finite number of small regions (a mesh) (Figure 3.1). Over each finite element, the unknown variables are approximated using known functions; these functions can be linear or higher-order polynomial expansions that depend on the geometrical locations (nodes) used to define the finite element shape. The governing equations in FEM are integrated over each finite element and the solutions summed over the entire problem domain. As a consequence of these operations, a set of finite linear equations is obtained in terms of a set of unknown parameters over each element. Solution of these equations is achieved using linear algebra techniques.

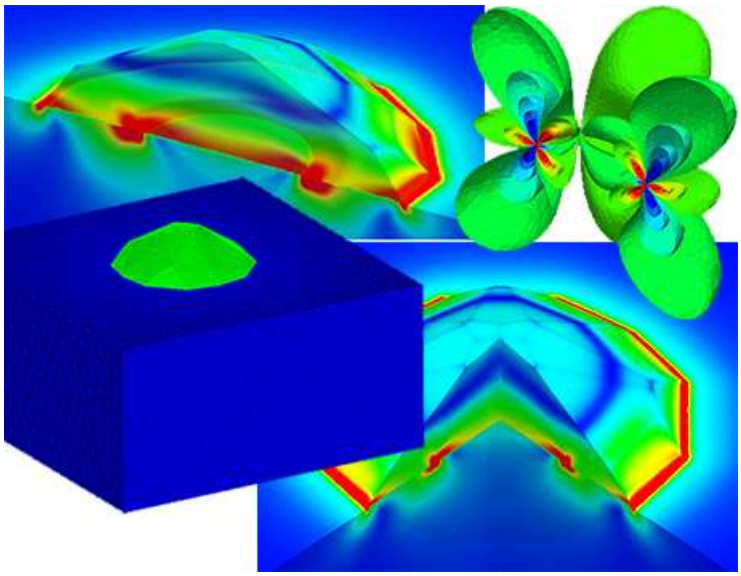

Figure 3.1. Examples of FEM meshes.

3.1.1 Weak or Variational Form

A FEM is always derived from the weak or variational formulation of the problem at hand. The variational formulation is obtained by multiplying the original equation by a “test function”. The continuous unknown is then approximated by a linear combination of “shape” functions; these shape functions are the test functions for the discrete variational formulation (this is the so called “Galerkin expansion”); the resulting equation is integrated over the domain.

Let us consider the derivation and implementation of a FEM Dirichelet homogenous problem, namely,

$$\begin{cases} -\Delta u(x,y) = f(x,y) \quad in \quad \Omega \\ \quad u(x,y) = 0 \quad on \quad \partial\Omega \end{cases} \tag{3.5}$$

where u is the sought solution, $f(x,y)$ a given function, $\Omega \subset \Re^2$ (the three dimensional case is similar) is a imitated domain and $\partial\Omega$ its boundary. In order to applies the Finite Element Model we need to introduce the weak formulation.

Multiplying the Poisson equation by an arbitrary function $v(x,y) \in H_0^1$ (test function) and integrating on Ω:

$$-\int_{\Omega} \Delta u(x,y) v(x,y) d\Omega = \int_{\Omega} f(x,y) v(x,y) d\Omega \,. \tag{3.6}$$

Applying the divergence theorem we obtain the Green formula for the Laplacian:

$$-\int_{\Omega} \Delta u(x,y) v(x,y) d\Omega = \int_{\Omega} \nabla u(x,y) \cdot \nabla v(x,y) d\Omega + \\ -\int_{\partial\Omega} \frac{\partial u(x,y)}{\partial n} v(x,y) d(\partial\Omega) \tag{3.7}$$

where $\dfrac{\partial u(x,y)}{\partial n} = \nabla u(x,y) \cdot \mathbf{n}$ and $\mathbf{n}$ is normal unit vector external to Ω.

Let us define the vector Sobolev space,

$$H^1(\Omega) \equiv$$

$$\equiv \left\{ v(x,y) : \Omega \to \Re \mid v(x,y) \in L^2(\Omega), \frac{\partial v}{\partial x_i} \in L^2(\Omega), i = 1,2 \right\} \tag{3.8}$$

and the Sobolev space $H_0^1(\Omega)$ with boundaries conditions,

$$H_0^1(\Omega) \equiv \left\{ v(x,y) \in H^1(\Omega) : v(x,y) = 0 \quad su \quad \partial\Omega \right\}. \tag{3.9}$$

If we choose $v(x,y) \in H_0^1(\Omega)$, then the weak formulation of the homogenous Dirichlet problem read: find the function $u(x,y) \in H_0^1(\Omega)$ such that

$$\int_\Omega \nabla u(x,y) \cdot \nabla v(x,y) d\Omega = \int_\Omega f(x,y) v(x,y) d\Omega, \tag{3.10}$$

for all $v \in H_0^1(\Omega)$. Under the hypothesis $f \in L^2(\Omega)$, integrals of Equation 3.10 are well defined.

For simplicity, in the following we will refer with V to the Sobolev space $H_0^1(\Omega)$.

We define the bilinear form $a : V \times V \to \Re$,

$$a(u,v) := \int_\Omega \nabla u(x,y) \cdot \nabla v(x,y) d\Omega, \tag{3.11}$$

and the linear functional $F : V \to \Re$,

$$F(v) := \int_{\Omega} f(x,y)v(x,y)d\Omega . \tag{3.12}$$

Then a compact formulation of the weak formulation reads: Find $u(x,y) \in V$, such that

$$a(u,v) = F(v) \tag{3.13}$$

for all $v \in H_0^1$.

The Lax-Milgram Lemma assert the existence and uniqueness of the solution of the weak formulation Dirichlet homogenous problem (3.13).

3.1.2 Finite element approximation

The space H_0^1 is very big and contains many functions and it is therefore just as hard to find a function $u(x,y) \in H_0^1$ which satisfies the variational equation (3.13) as it is to solve the original problem (3.5). The approximation of the FEM (Galerkin method) is therefore to look for a solution approximation Ψ_h, dependent on a positive parameter h, within a small, finite dimensional, subspace V_h of H_1^0 typically consisting of piecewise polynomials,

$$\Psi_h \in V_h \subset V \text{ with } \dim V_h = N_h < \infty \tag{3.14}$$

The Galerkin method consist on founding a function Ψ_h such that

$$a(u_h, v) = F(v) \tag{3.15}$$

for all $v(x, y) \in V_h$.

Let $\{\psi_k\}$, $k = 1,..., N_h$ be the set of hat basis functions of V_h, then

$$v = \sum_{k=1}^{N_h} c_k \psi_k \in V_h . \tag{3.16}$$

Therefore is satisfactory that Equation (3.15) is satisfied for each basis function,

$$a(u_h, \psi_k) = F(\psi_k) \tag{3.17}$$

with $1 \le k \le N_h$.

Because of $\Psi_h \in V_h$, then

$$\psi_h = \sum_{k=1}^{N_h} \gamma_k \psi_k , \tag{3.18}$$

therefore the problem (3.15) can be solved finding the coefficients $\Gamma = [\gamma_1,..., \gamma_{N_h}]^T$ that satisfied the linear system

$$\sum_{k=1}^{N_h} \gamma_k a(\psi_k, \psi_i) = F(\psi_i) \qquad (3.19)$$

$i = 1,2,..., N_h$.

The matrix $A = [\alpha_{ki}]_{k,i=1}^{N_h}$ is the so-called stiffness matrix, with entries

$$\alpha_{ki} := a(\psi_k, \psi_i). \qquad (3.20)$$

The vector $B = [b_1,..., b_{N_h}]^T$, called the load vector, contains the unknown coefficients

$$b_i := F(\psi_i). \qquad (3.21)$$

Is possible to demonstrated that the matrix A, associated to Poisson problem with homogenous conditions, is symmetric and positive definite. Therefore, the solution of the linear system $A\Gamma = B$ exists and is unique, then exists and is unique the approximate solution Ψ_h.

3.2. The Finite Volume Method

FVM is a discretization method which is well suited for the numerical simulation of various types (elliptic, parabolic or hyperbolic, for instance) of conservation laws; it has been extensively used in several engineering fields, such as fluid mechanics, heat and mass transfer or petroleum engineering.

Some features are equal to the Finite Element methods as arbitrary geometries, using structured grids, unstructured meshes and robust schemes. An additional feature is the local conservativity on the numerical fluxes, the numerical flux is conserved from one discretization cell to its neighbour. This makes the finite volume scheme attractive, when modeling problems for which the flux is of importance, such as in fluid mechanics, semi-conductor device simulation, heat and mass transfer.

The FVM is locally conservative because it is based on a balance approach: a local balance is written on each discretization cell which is often called control volume; by the divergence formula, an integral formulation of the fluxes over the boundary of the control volume is then obtained. The fluxes on the boundary are discretized with respect to the discrete unknowns.

The grid of control volumes, is the dual grid of the triangulation, which can be either a Voronoi or Barycentric grid. In a Voronoi grid, the edges are perpendicular to the edges of the

triangulation and intersect them at their midpoints, whereas in a barycentric grid, the edges go from the intersection of the median lines of the triangles of the triangulation to the midpoint of the edges of the triangulation (Figure 3.2).

(a) (b)

Figure 3.2. Example for a triangle with (a) barycentric grid and (b) Voronoi grid.

3.2.1 Formulation of a finite volume scheme

The principle of the finite volume method will be shown here on the Dirichlet problem, namely a second order differential operator without time dependent terms and with homogeneous Dirichlet boundary conditions. Let us consider here the following elliptic equation

$$-\Delta u(x,y) = f(x,y), \quad (x,y) \in \Omega \tag{3.22}$$

with Dirichlet boundary condition:

$$u(x,y) = 0, \quad (x,y) \in \partial\Omega \tag{3.23}$$

where Ω is an open bounded polygonal subset of $\Re^d$ and $f \in C^2(\Omega, \Re)$ with $d = 2$ (the three dimensional case is similar).

In order to perform a space finite volume discretization of Equation (3.22), we considered an admissible mesh $\mathrm{T} = (K_{i,j})_{1=1,...,N_1;\, j=1,...,N_2}$ of the domain Ω of $\Re^d$, over which Equation (3.22) is introduced. The mesh is such that $\overline{\Omega} = U_{k \in \mathrm{T}} \overline{K}$, where an element of T, denoted by K, is an open subset of Ω and is called a control volume. Assumptions on the meshes will be needed for the definition of the schemes (Appendix A); they also depend on the type of equation to be discretized.

The finite volume schemes is found by integrating Equation (3.22) over each control volume $K_{i,j}$, which yields

$$\begin{cases} -\int_{y_{j-\frac{1}{2}}}^{y_{j+\frac{1}{2}}} u_x(x_{i+\frac{1}{2}}, y)dy + \int_{y_{j-\frac{1}{2}}}^{y_{j+\frac{1}{2}}} u_x(x_{i-\frac{1}{2}}, y)dy \\ \int_{x_{i-\frac{1}{2}}}^{x_{i+\frac{1}{2}}} u_y(x, y_{j-\frac{1}{2}})dx + \int_{x_{i-\frac{1}{2}}}^{x_{i+\frac{1}{2}}} u_y(x, y_{j+\frac{1}{2}})dx = \int_{K_{ij}} f(x, y)dxdy \end{cases} . \tag{3.24}$$

The fluxes are then approximated by differential quotients with respect to the discrete unknowns $(u_{i,j}, i = 1,..., N_1, j = 1,..., N_2)$, hence the numerical scheme writes

$$F_{i+\frac{1}{2},j} - F_{i+-\frac{1}{2},j} + F_{i,j+\frac{1}{2}} - F_{i,j-\frac{1}{2}} = h_{i,j} f_{i,j}, \tag{3.25}$$

$$\forall (i,j) \in \{1,...,N_1\} \times \{1,...,N_2\},$$

where $h_{i,j} = h_i \times k_j$, $f_{i,j}$ is the mean value of f over $K_{i,j}$, and

$$F_{i+\frac{1}{2},j} = -\frac{k_j}{h_{i+\frac{1}{2}}}(u_{i+1,j} - u_{i,j}), \tag{3.26}$$

for $i = 0,...,N_1, j = 1,...,N_2$,

$$F_{i,j+\frac{1}{2}} = -\frac{h_i}{k_{j+\frac{1}{2}}}(u_{i,j+1} - u_{i,j}), \tag{3.27}$$

for $i = 1,...,N_1, j = 0,...,N_2$,

$$u_{0,j} = u_{N_1+1,j} = u_{i,0} = u_{i,N_2+1} = 0, \tag{3.28}$$

for $i = 1,...,N_1, j = 0,...,N_2$.

The numerical scheme (3.25)-(3.28) is therefore clearly conservative and the numerical approximations of Equation (3.22) can easily be shown to be consistent.

3.3. The Boundary Volume Method

BEM has emerged as one of the most powerful computational tools for solving a wide variety of problems in science and engineering. It brings the feature of being simple in geometric data preparation. This particular feature of BEM derives from the fact that the discretization of the problem domain is confined to the boundary alone, the unknowns to be solved for are only on the boundary (Figure 3.3).The solution inside the domain can be computed as a post-processing step after the unknowns on the boundary points have been solved for. Since the BEM reduces the problem dimension by one, it leads to dramatic reductions in mesh generation efforts, resulting in significant savings in processing time. The BEM is an integral-type of numerical analysis procedure in which the integration of the governing differential equations is performed before the numerical analysis has been carried out. The BEM is a global numerical analysis procedure. The solution of the problem is found by superposing singular solutions distributed over the entire boundary of the problem. When this influence of a single source for a discretized boundary is summed over all the boundary segments/elements, it fills the entire row of the final algebraic matrix equation. The equilibrium is globally satisfied at once for the whole domain.

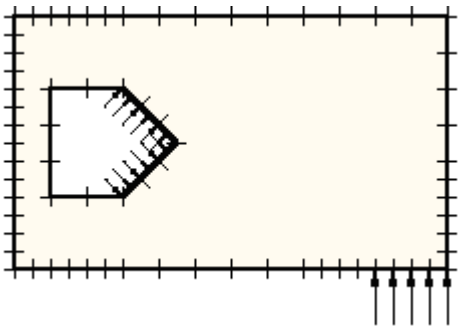

Figure 3.3: BEM discretization of problem domain.

3.3.1 Weak formulation of the differential equation

The Boundary Element Method relies on an integral representation of the solution of an elliptic problem.

Let Ω be a bounded, open domain in $\Re^d$ with a boundary $\partial\Omega$ (generalization to the second and third dimensional case is similar). At any point $\vec{x} \in \partial\Omega$ the inner unit normal vector is denoted by $\mathbf{n}$. We will consider the following boundary value problem:

$$\begin{cases} \Delta u(\vec{x}) = 0 \quad in \quad \Omega \\ u(\vec{x}) = f(\vec{x}) \quad on \quad \partial\Omega \end{cases} \tag{3.25}$$

Starting point for the boundary element formulation is the weighted residual (or weak) statement of the differential equation. For Laplace's Equation (3.25), it is given by

$$\int_{\Omega} \Delta u(\vec{x}) w(\vec{x}) d\Omega = 0 \tag{3.17}$$

with $w(\vec{x}) \in C^2$ a test function.

The step of transformation of boundary corresponds in 1-D to the partial integration of the differential operator. It requires the application of special integral theorems depending on the problem dimension. These theorems reduce domain integrals in boundary integrals. The transformation of the differential operator to the boundary is done by applying Green's theorem twice to the weighted residual statement. In index notation this reads

$$\int_\Omega u_{,ii} w d\Omega = \int_\Gamma u_{,i} n_i w d\Gamma - \int_\Omega \frac{\partial u}{\partial x_i}\frac{\partial w}{\partial x_i} d\Omega =$$
$$= \int_\Gamma (u_{,i} w - w_{,i} u) n_i d\Gamma + \int_\Omega w_{,ii} u d\Omega . \qquad (3.18)$$

Let consider the Green's function $u^*(\vec{x},\vec{\xi})$ for the unbounded space of the Laplacian operator $\nabla^2 u$,

$$L^* u^*(\vec{x},\vec{\xi}) = \nabla^2 u^*(\vec{x},\vec{\xi}) = -\delta(\vec{x}-\vec{\xi}) \qquad (3.19)$$

where L^* is a linear differential operator.

The minus sign of the Dirac distribution is introduced for convenience such that the obtained system matrices become positive. In 2-D the Green's function is given by (s.f. Appendix B):

$$u^*(\vec{x},\vec{\xi}) = -\frac{1}{2\pi}\ln\left|\vec{x}-\vec{\xi}\right| = -\frac{1}{2\pi}\ln r \tag{3.20}$$

$$\frac{\partial u^*}{\partial \vec{n}} = q^*(\vec{x},\vec{\xi}) = -\frac{1}{2\pi r}\frac{\partial r}{\partial \vec{n}} = -\frac{1}{2\pi\left|\vec{x}-\vec{\xi}\right|^2}(\vec{x}-\vec{\xi})\cdot\vec{n} \tag{3.21}$$

with the common abbreviation r of the Euclidean distance $\left|\vec{x}-\vec{\xi}\right| = \sqrt{(x_i-\xi_i)^2}$. The 3-D case leads to (s.f. Appendix C):

$$u^*(\vec{x},\vec{\xi}) = \frac{1}{4\pi\left|\vec{x}-\vec{\xi}\right|} = \frac{1}{4\pi r} \tag{3.22}$$

$$\frac{\partial u^*}{\partial \vec{n}} = q^*(\vec{x},\vec{\xi}) = -\frac{1}{4\pi r^2}\frac{\partial r}{\partial \vec{n}} = -\frac{1}{4\pi\left|\vec{x}-\vec{\xi}\right|^3}(\vec{x}-\vec{\xi})\cdot\vec{n}\,. \tag{3.23}$$

The functions u^* and q^* are denoted as single layer and double layer potentials, respectively. After selecting $w = u^*$, Equation (3.18) and $\nabla^2 u = 0$ associated with the sifting property of the Dirac distribution lead to

$$u(\xi) = \int_\Gamma (u^*(x,\xi)q(x) - q^*(x,\xi)u(x))d\Gamma\,,\ \xi\in\Omega \tag{3.24}$$

where

$$q(x) = \frac{\partial u(x)}{\partial \vec{n}} \tag{3.25}$$

The common notations x for the field point or receiver point (marked by the vector $\vec{x}$) and ξ for the load point or source point (marked by the vector $\vec{\xi}$) have been used.

Other than in the 1-D case, higher dimensional problems lead to integrals over the boundary Γ of the domain Ω, or to be more precise, over the boundary Γ_x consisting of all field points x on Γ.

By recalling all steps necessary to derive Equation (3.24), one recognizes, that the weighted residual statement Equation (3.17) does not lead to an approximation. The question arises, whether an exact solution of Equation (3.24) is an exact solution of Laplace's equation as well. This seems not to be the case, since the weighted residual statement allows for local errors in the domain but averages them to zero by domain integration. An exact solution of Equation (3.24) which fulfils the integral pointwise represents a weighting with infinitely many linearly independent test functions in the residual statement (3.17). It follows that statement (3.17) is only fulfilled if the differential equation is satisfied identically. Thus, the exact solution of (3.24) is an exact solution of the corresponding differential equation as well.

3.4. Comparison between discretization techniques

Depending on the purpose of the study, different numerical methods could be applied for solving scientific and engineering problems.

Generally computational fluid dynamics tends to use the Finite Volume scheme. Computational fluid dynamics problems usually require discretization of the problem into a large number of cells/gridpoints (millions and more), therefore cost of the solution favors simpler, lower order approximation within each cell. This is especially true for 'external flow' problems, like air flow around the car or airplane, or weather simulation in a large area. With the FVM, discontinuities of the coefficients will not be any problem if the mesh is chosen such that the discontinuities of the coefficients occur on the boundaries of the control volumes. From the industrial point of view, the FVM is known as a robust and cheap method for the discretization of conservation laws (by robust, we mean a scheme which behaves well even for particularly difficult equations, such as nonlinear systems of hyperbolic equations and which can easily be extended to more realistic and physical contexts than the classical academic problems). The FVM is cheap thanks to short and reliable computational coding for complex problems. However, in some cases, it is difficult to design schemes which give enough precision. Indeed, the FEM can be much more precise than the FVM when using higher

order polynomials, but it requires an adequate functional framework which is not always available in industrial problems.

In several classes of problems like infinite-domain problems such us those in acoustics, electrostatics, and electromagnetics BEM is a very efficient option. The BEM solution of a problem is found by superposing singular solutions distributed over the entire boundary of the problem. The advantages in the boundary element method arises from the fact that only the boundary (or boundaries) of the domain of the PDE requires sub-division. Thus the dimension of the problem is effectively reduced by one. In cases where the domain is exterior to the boundary, as it is in potential flow past an obstacle, the extent of the domain is infinite and hence the advantages of the BEM are even more striking; the equation governing the infinite domain is reduced to an equation over the (finite) boundary. Despite the big advantage to reduce the dimension of the problem by one, BEM is not successfully applied to non linear problems and matrices resulted in BEM are not easy to solve because are unsymmetric and fully populated.

The FEM is the method of choice in all types of analysis in structural mechanics, i.e. solving for deformation and stresses in solid bodies or dynamics of structures. The FEM is based on a variational formulation, which is written for both the continuous and the discrete problems. The nature of the solution and the degree of approximation depend only on the size and number of the elements used but also on the interpolation functions selected.

An important feature of FEM that sets it apart from other numerical methods is the ability to formulate solutions for individual elements before putting them together to represent the entire problem.

This means, for example, that if we are treating a problem in stress analysis, we find the force-displacement or stiffness characteristics of each individual element and then assemble to find the stiffness of the whole structure. A complex problem reduces to considering a series of greatly simplified problems. The most attractive feature of the FEM is its ability to handle complicated geometries and boundaries, and to include inhomogeneities and non linearity in the domain with relative ease.

Motivated by the previous considerations, we can state that the most adequate method to calculate stress and strain and hence deriving associated geophysical signals changes in a given material is the finite element method. Hence, we use FEM for modeling heterogeneous medium, topography irregularity, complex loading and different rheologies in the description of ground deformation in volcanic and sismogenetic areas. Appendix D, E and F show the FEM formulation for elastic, viscoelastic and plastic problems.

Chapter 4

Forward FE modeling

In the design of natural structures, numerical simulations play an increasingly important role. This can be attributed to the high costs or practical difficulties related to experiments, which have to confront rapid advances in the computational power and the resulting decrease in the costs for computer simulations. However, in order to supplement or even replace experiments, simulation approaches have to fulfill strong requirements. An essential demand is that the simulations are efficient and lead to accurate and reliable results. This in turn will depend upon the mathematical model of the physical world which the has to be chosen, and which specific simulation tool by applying assumptions about the loading situation, initial and boundary conditions.

The most comprehensive understanding of volcanic processes necessarily calls for a multi-disciplinary, integrated approach of data acquisition for monitoring, analysis, identification and modeling.

Geodetic observations play an important role for the monitoring of the volcanic activity and for the quantitative evaluation of the geophysical processes preceding and accompanying volcanic unrest (Bonaccorso and Davis, 2004). Fundamental insight about volume changes in the magma reservoir and the dynamics of dike intrusion processes is generally obtained using ground deformation (Voight et al., 1998; Battaglia et al., 2003; Murase et al., 2006). However, an accurate interpretation of deformation signals is necessary for improving the monitoring of active volcanoes as well as developing a better understanding of the pre-eruptive mechanisms that produce them. Volcanic processes are complex geophysical systems and it is difficult to derive analytical deformation models, unless important simplifications and approximations are taken into account (McTigue, 1986; Carbone et al., 2007). The drawbacks of the analytical formulations for modeling volcanic activities are the assumption of simple geometries for the sources embedded in homogeneous elastic half-space. Surface displacements in a homogeneous elastic half-space have been described by Mogi (1958) for a spherical source to explain the inflation/deflation of the magma reservoir and by Okada (1985; 1992) for a rectangular fault to model the opening of eruptive fractures.

Nevertheless natural characteristics of volcanic areas such as topography or lateral variations of rheological properties may have great influence on the observed signals: such complexities can be

treated using numerical methods, therefore the homogeneous and elastic half-space may be unsuitable to model them.

In this section we validated the numerical method in a homogeneous elastic half-space and compared the results with those obtained from analytical models. Particularly, here we reported results obtained comparing the Okada analytical model with a numerical dislocation source. In geology, a dislocation source, or fault, is a planar rock fracture which shows evidence of relative movement. It can be characterized by three sense of movement (slip): dip slip, strike slip and (iii) tensile slip. The dip slip component occurs when the crust is extended, the strike-slip component when the main sense of slip is horizontal and the tensile slip when the main sense of slip is normal to the fault.

We performed a convergence analysis to quantify the discretization errors, which are sensitive to the size and quality of the mesh elements and can cause inaccurate numerical solutions. Secondly, several numerical models were conducted to appreciate how the complex distribution of elastic medium parameters, the topography relief and rheological properties make the numerical results differ from the simple analytical solutions. Benchmarks tests are conducted. Computations are carried out with two software packages: the FE software COMSOL and PyLith open source code. Comparison between the two packages is shown.

4.1 Comparison between COMSOL and PyLith packages

All the computations performed in this thesis are made using one (or both) of these two finite element software packages: COMSOL Multiphysics, a commercial product, and PyLith, an open source program.

COMSOL Multiphysics is a powerful interactive environment for modeling and solving all kinds of scientific and engineering problems based on partial differential equations (PDEs). With this product is possible to easily extend conventional models for one type of physics into multiphysics models that solve coupled physics phenomena and do so simultaneously. Thanks to the built-in physics modes it is possible to build models by defining the relevant physical quantities, such as material properties, loads, constraints, sources, and fluxes, rather than by defining the underlying equations. COMSOL Multiphysics then internally compiles a set of PDEs representing the entire model. It is feasible to access the power of COMSOL Multiphysics as a standalone product through a flexible graphical user interface, or by script programming in the COMSOL Script language or in the MATLAB language (Comsol, 2008).

PyLith is a multi-scale simulation software package for earthquake physics. It is a scalable software for simulation of crustal deformation across spatial scales ranging from meters to hundreds of

kilometres and temporal scales ranging from milliseconds to thousands of years. It allows the solution of both implicit (quasi-static) and explicit (dynamic) problems using a finite-element scheme. The code runs in either serial or parallel mode, and the design allows for relatively easy scripting using the Python programming language. Material properties and values for boundary and fault conditions are specified using spatial databases, which permit easy prescription of complex spatial variations of properties and parameters. Simulation parameters are generally specified through the use of simple ASCII files or the command line. At present, mesh information may be provided using a simple ASCII file (PyLith mesh ASCII format) or imported from CUBIT or LaGriT, two widely used meshing packages. The elements available include a linear bar in 1D, linear triangles and quadrilaterals in 2D, and linear tetrahedral and hexahedra in 3D. Higher-order (quadratic) elements are also supported. Materials presently available include isotropic elastic, linear Maxwell viscoelastic (3D only), and generalized Maxwell viscoelastic (3D only). Boundary conditions include Dirichlet (prescribed displacements and velocities), Neumann (traction), and absorbing boundaries. Cohesive elements are used to implement slip across interior surfaces (faults) (Aagaard et al., 2008).

We made a comparison between the two software packages considering a simple 3D elastic problem. Meshes, properties of the medium, boundary conditions and numerical solvers are the same in both problems. We compare vertical displacements obtained from COMSOL and PyLith in 20 different stations (Figure 4.15). We found a general agreement between the two solutions. This allow us for

using COMSOL or PyLith concerning only about the advantages that one software provide respect the other in a specific case study.

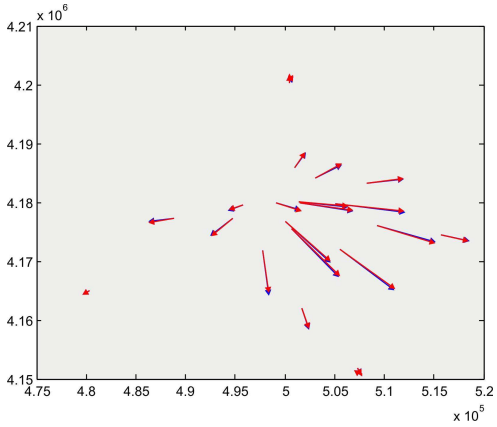

Figure 4.1. Comparison between vertical displacement obtained using COMSOL (blue line) and PyLith (red line) packages.

4.2 Analytical and numerical model: error estimates

The definition of a FEM problem requires to set up boundary conditions, optimal size of domain, meshing, and the type of the elements that are not known a priori. Therefore, a robust preliminary set-up is needed to obtain realistic results.

We considered a 3D FEM model reproducing a rectangular dislocation source in a homogeneous and isotropic half-space. The geometry of the intrusion source is reported in Table 4.1.

Table 4.1. Geometrical parameters of the dislocation source.

Length L [m]	1000
Width [m]	1000
Inclination angle δ [°]	90
Strike angle θ [°]	0
Depth of the top d [m]	1000
Dislocation **B** [m]	1

We assumed stress-free boundary condition at the upper surface, and zero displacement values at bottom and lateral boundaries. The dislocation source is modelled as a rectangular discontinuity surface by means of pair elements. The elements are added in pairs along the surface rupture, where in one element the dislocation $+U$ and in the other $-U$ is assigned. A non-null homogeneous dislocation over the rupture area is imposed and an identity pair condition along the remaining surface is enforced to assure the continuity of deformation fields on the volume surrounding the dislocation source. The medium is assumed to be elastic with Lames coefficients $\lambda=\mu$, namely Poisson ratio $\upsilon=0.25$, and Young modulus of 30 GPa. A computational domain of 50 km × 50 km × 50 km is meshed with tetrahedral elements (Figure 4.2).

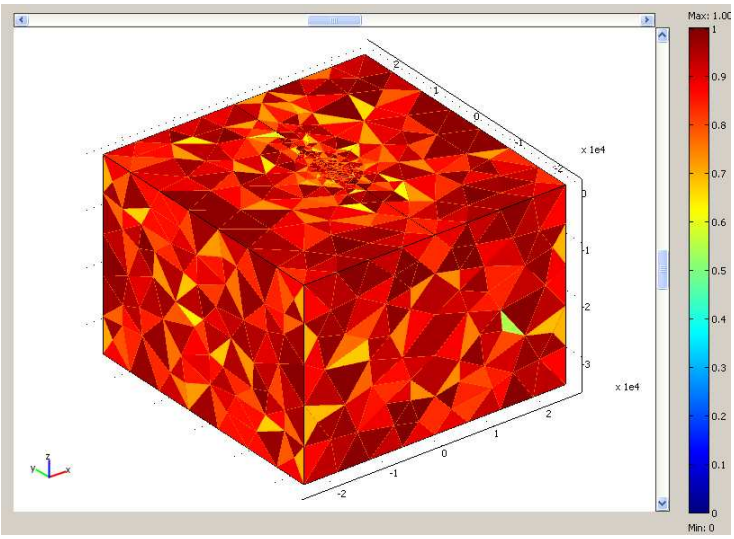

Figure 4.2. Computational domain. Colors show element mesh quality.

In the finite element analysis a critical step is the meshing of the computational domain. The number of elements of the mesh largely influences the accuracy of the solution. Starting from a coarse mesh, we incrementally refined the meshed domain increasing the number of nodes. We examined the accuracy of the solution in terms of discretization error due to the meshing procedure to test how the mesh resolution can affect the numerical solution. A convergence analysis was performed to quantify the discretization errors caused by the mesh resolution. Eight different meshes were constructed by refining the domain. The number of nodes was increased to improve the mesh resolution and the solution accuracy (Table 4.2).

Table 4.2. Statistics for the eight simulations in which the mesh parameters are changed.

	Simulation							
	#1	#2	#3	#4	#5	#6	#7	#8
Mesh vertices	2228	2513	2570	3195	3977	5101	8591	36196
Vertex elements	32	32	32	32	32	32	32	32
Edge elements	206	229	230	280	307	350	408	612
Boundary elements	2166	2434	2482	3004	3586	4226	6160	15620
Elements (thedraedral)	9858	11236	11505	14663	18888	25141	45021	205700
Minimum element quality	0.3544	0.3083	0.3441	0.3109	0.3417	0.2960	0.3050	0.2454

Besides the number of nodes, also the mesh quality should be taken into account to assure an accurate solution. The mesh not only must properly describe the geometrical boundaries, but it must not have degenerated elements that make the numerical solution instable. Therefore, we defined a factor to track the mesh quality among the several meshes. For tetrahedral elements, more the element approaches an equilateral tetrahedron, more the numerical solution is stable and accurate (Field, 2000; Edelsbrunner, 2001). For each element in the mesh we evaluated its quality with respect to the equilateral tetrahedron as:

$$q = f \frac{V^2}{(A+B+C+D)^3} \tag{4.1}$$

where $\boldsymbol{V}$ denotes the volume of the tetrahedron, $\boldsymbol{A}$, $\boldsymbol{B}$, $\boldsymbol{C}$ and $\boldsymbol{D}$ are the areas of its faces and $f = 216\sqrt{3}$ is a normalizing coefficient ensuring that the quality of an equilateral tetrahedron is equal to 1. The quality

of the worst elements for each mesh is reported in Table 4.2. In all the computations the minimum mesh quality was higher than 0.2.
To quantify the accuracy of the numerical solutions, a mean misfit function with respect the analytical solution is defined as:

$$\Delta(U) = \sum_{i=1}^{N} \frac{\left| U_i^{FE} - U_i^{AN} \right|}{N} \tag{4.2}$$

where U_i^{FE} is the computed deformation at the *i*-th node for the numerical model, U_i^{AN} the corresponding result for the analytical model, and N is the total number of nodes in the meshed domain. To provide a reference for the quality of the fit, we have normalized each mean misfit value by the average magnitude of the deformation field:

$$M(U) = \sum_{i=1}^{N} \frac{\left| U_i^{AN} \right|}{N} . \tag{4.3}$$

The misfit function $\delta_m = \Delta(U)/M(U)$, $m=x,y,z$, computed for each deformation component decreases quickly as the mesh quality is improved (Figure 4.3).

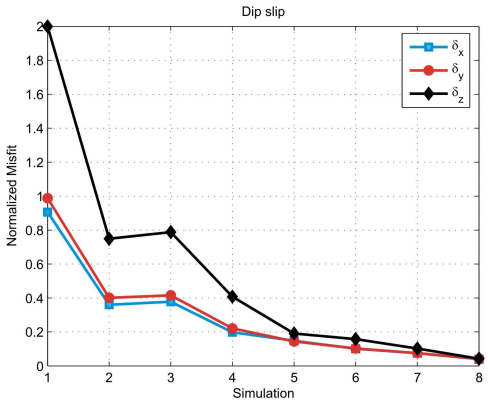
Dip slip
Normalized Misfit
Simulation
δx
δy
δz

(a)

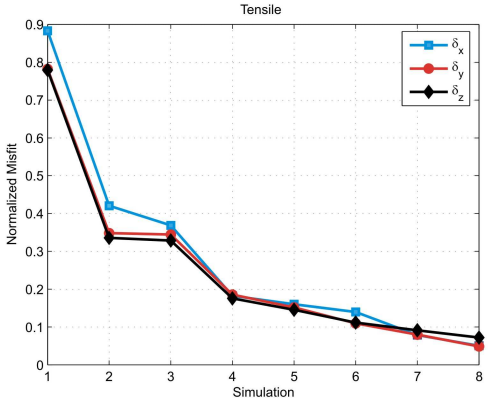
Tensile
Normalized Misfit
Simulation
δx
δy
δz

(b)

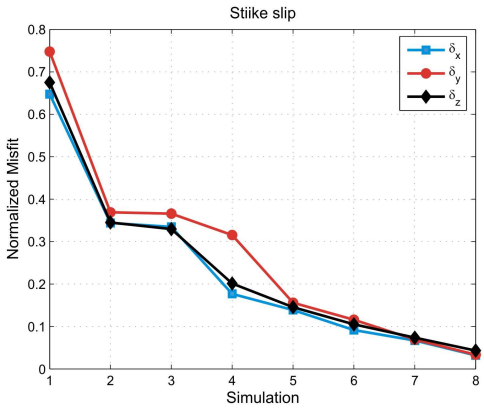

(c)

Figure 4.3: Misfit values between numerical and analytical solutions for all the displacement components. Dip-slip (a), tensile (b) and strike- slip (c) dislocation sources are considered.

The displacements due to the different component slip in a homogeneous medium are compared to Okada's dislocation models (Okada, 1992). The results from the FEM models are generally consistent with those from the dislocation model in a homogeneous half-space as the mesh reaches a number of about 15,000 elements. The ratio $\Delta(U)/M(U)$ is less than 0.1 for all the displacement components and no significant improvements are obtained when using finer meshes. Therefore, the numerical results are found to be in nearly perfect agreement with the analytical solutions.

The domain was proved to be big enough to avoid numerical artefacts in the solution due to the finite boundary condition. The external boundaries of the domain depend on the extent of the displacement components, which is especially related to the depth of the source. We performed several tests for a opening source, whose geometric

parameters as the same as before (Table 4.1), and the depth is varied from 1 to 4 km. We consider also two different domains which extend 50 km × 50 km × 35 km (Figure 4.4) and 100 km × 100 km × 75 km (Figure 4.5). As the depth of the source increases the deformation components show a greater spatial extent. The deformation field decays to 10% of the maximum value within 10 km from the source when the source is at 1 km depth, within 33 km when the source is at 4 km. The source depth controls the shape and the extent of the deformation field, and so regulates also the computational domain size. As a rule of thumb, the domain size must be at least twice the deformation field extent, or in other words about 40 times the depth of the source to obtain an accurate numerical solution.

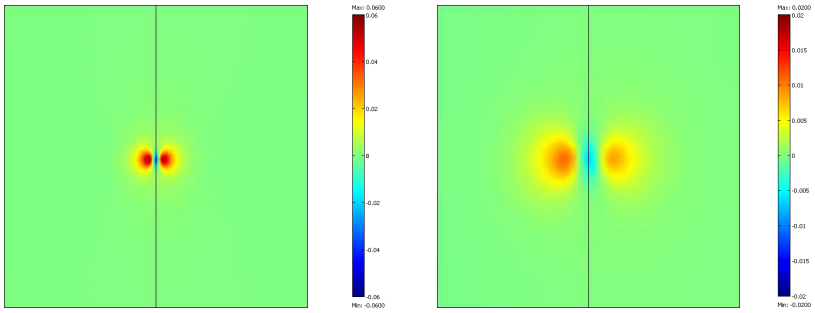

Figure 4.4. Ground uplift due to a source placed at (a) 1 km depth and (b) 4 km depth. The computational domain extends 50 km × 50 km × 35 km.

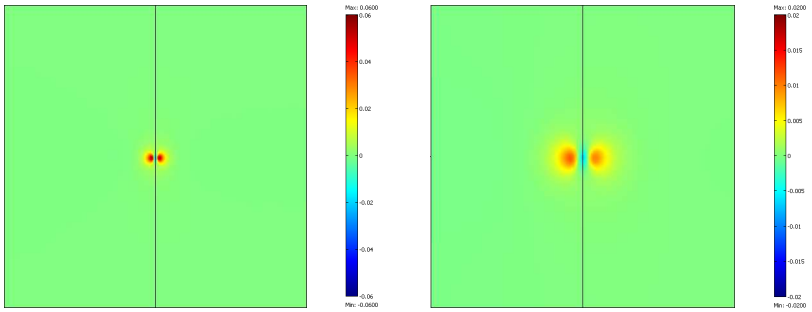

Figure 4.5. Ground uplift due to a source placed at (a) 1 km depth and (b) 4 km depth. The computational domain extends 100 km × 100 km × 75 km.

4.3 Topography and medium heterogeneity

Although the analytical model provided an acceptable representation of the dike intrusion, it is not able to justify all the details. The simplified assumption of elastic half-space medium disregards effects caused by the topographic relief and the presence of medium heterogeneity, while they could play a role in the modeling procedure. To evaluate how the topography and medium heterogeneity could affect the computed ground deformation, we carried out numerical models including the real topography of the Etna volcano and the medium heterogeneity inferred from seismic tomography study. In the numerical computations we used an opening source geometry from Table 4.3. We evaluate three numerical models in which we considered: (i) a homogeneous elastic medium with a flat surface, (ii) a homogeneous elastic medium with the real topography

of Mt Etna, and (iii) an elastic heterogeneous medium with the real topography relief.

Table 4.3. Geometrical parameters of the dislocation source.

Dislocation **B** [m]	3.5
Length L [m]	2200
Width [m]	2300
Depth of top d [m]	1400 a.s.l.
Inclination angle δ [°]	90
Strike angle θ [°]	7

4.3.1 Flat topography and homogeneous medium.

We performed a 3D FEM model considering a rectangular dislocation embedded in a homogeneous, isotropic and elastic half-space. The medium is assumed to be elastic and Poissonian ($\lambda = \mu$) with a Young modulus of 30 GPa. This numerical models equivalent to the Okada's analytical model. Indeed, all the deformation components well match the analytical ones within the computational error, assuring the validity of the domain size, mesh resolution and boundary conditions used in the numerical computations (Figure 4.6).

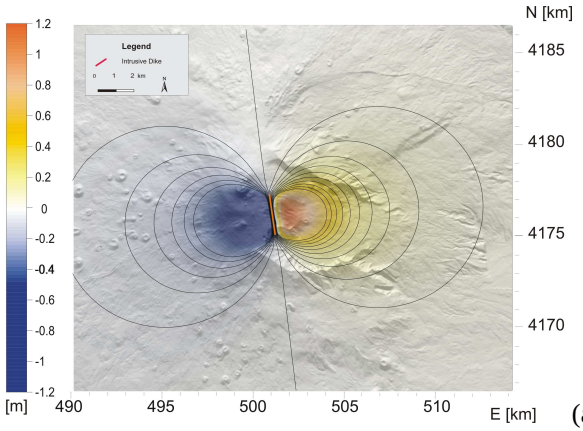
Legend
Intrusive Dike
0 1 2 km
N
1.2
1
0.8
0.6
0.4
0.2
0
-0.2
-0.4
-0.6
-0.8
-1
-1.2
[m]
490
495
500
505
510
E [km]
N [km]
4185
4180
4175
4170

(a)

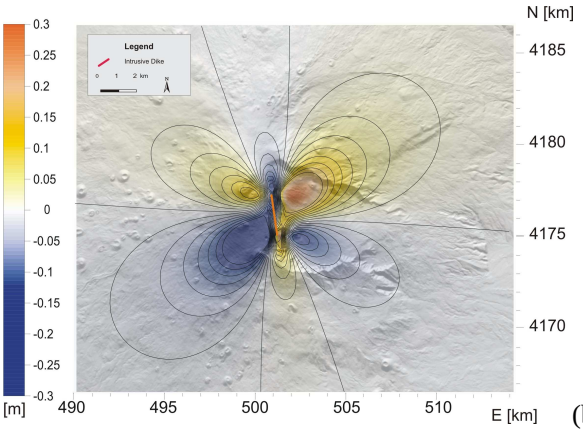
Legend
Intrusive Dike
0 1 2 km
N
0.3
0.25
0.2
0.15
0.1
0.05
0
-0.05
-0.1
-0.15
-0.2
-0.25
-0.3
[m]
490
495
500
505
510
E [km]
N [km]
4185
4180
4175
4170

(b)

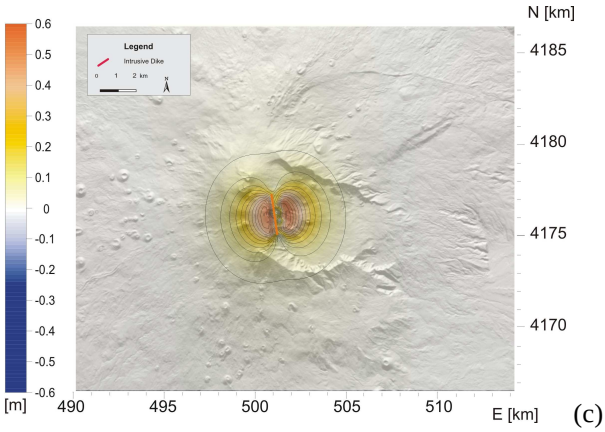

Figure 4.6. Deformation field due to a source in a homogeneous, isotropic and elastic half-space: (a) eastern component, (b) northern component, (c) vertical uplift. Contour lines are at 0.05 m.

4.3.2 Real topography and homogeneous medium.

To examine the effects of topography on the deformation at Mt Etna, we included in the numerical model the real 3D topography of the volcano using a digital elevation model from the 90m Shuttle Radar Topography Mission (SRTM) data. The domain was modelled using a total of 15585 elements and 3288 nodes. Numerical results highlighted the influence of topography on the deformation field. Ground deformation components differ significantly in shape and amplitude from those of the simple model based on the assumption of a homogeneous half-space medium (Figure 4.7). The discrepancies between the numerical and analytical models are mainly restricted to the volcano summit area where the topography of Mt Etna is most irregular. The symmetry of the solution observed in the analytical solution is lost in the numerical results since the volcano edifice is

rather asymmetric having a strong mass deficit in the eastern sector with respect to the western sector in correspondence of Valle del Bove. The amplitudes of the deformation components are a little smaller because the effective distance between the source and the ground surface is increased. To evaluate the effect of topography, we compare numerical and analytical solutions for source at different depths. We find out that the topography strongly influences the ground deformation especially when the source is quite shallow. The residuals, the difference between the analytical and the numerical models, gradually increase as the source became shallower (Figure 4.8). This discrepancy depends also on the horizontal distance between the observation points and the position of the source. We compute the residuals on different grid sizes centred on the tensile dike extending: (i) 5 km × 5 km, (ii) 10 km × 10 km, (iii) 20 km × 20 km and (iv) 30 km × 30 km. As the grid extends farther from the dike the numerical solution converges to the analytical one.

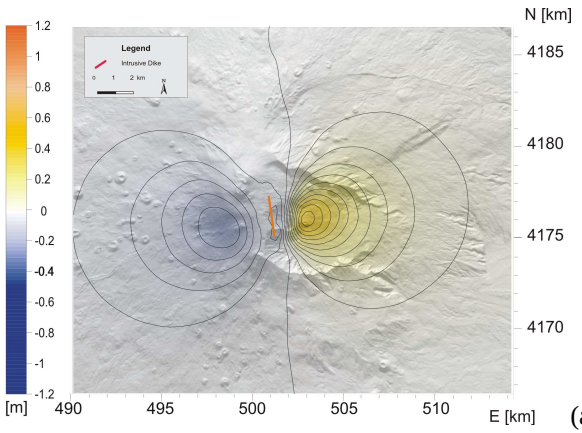

(a)

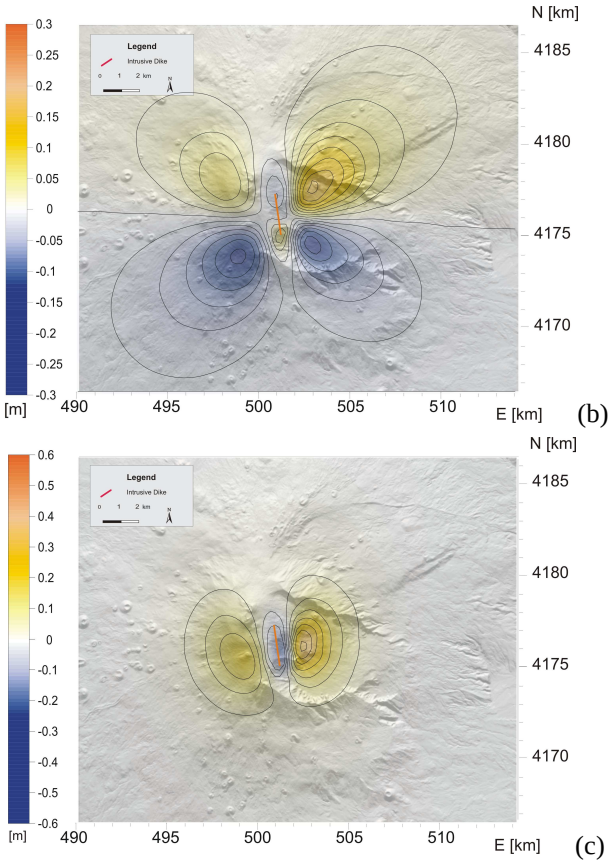

Figure 4.7. Deformation components caused by the 2001 intrusive dike in a homogeneous, isotropic and elastic medium with the real topography of Mt Etna: (a) eastern component, (b) northern component, (c) vertical uplift. Contour lines are at 0.05 m.

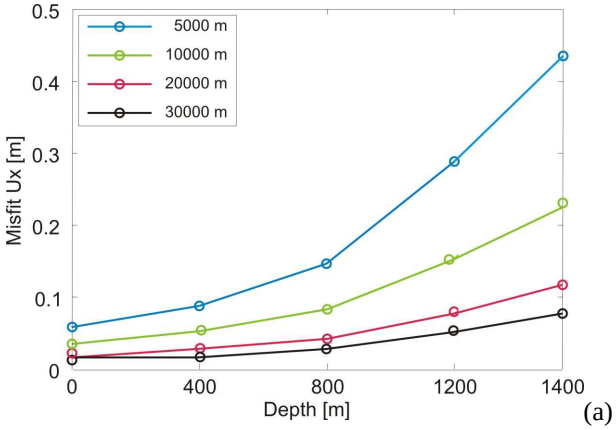
5000 m
10000 m
20000 m
30000 m
Misfit Ux [m]
Depth [m]
0
0.1
0.2
0.3
0.4
0.5
0
400
800
1200
1400

(a)

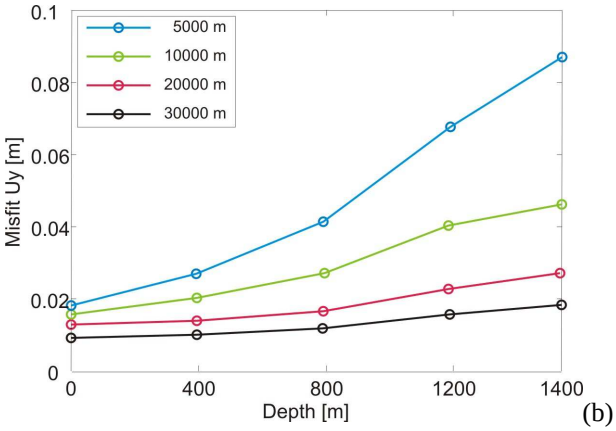
5000 m
10000 m
20000 m
30000 m
Misfit Uy [m]
Depth [m]
0
0.02
0.04
0.06
0.08
0.1
0
400
800
1200
1400

(b)

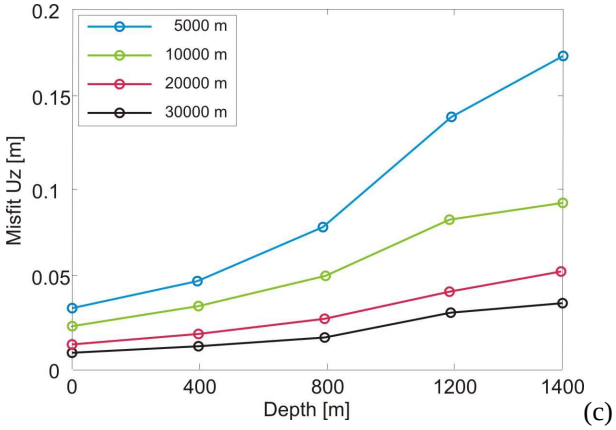

Figure 4.8. Comparisons between the analytical and numerical solutions including the Mt Etna topography. The computations were performed for different depths of the source and varying the extent of the grid point on which the misfit is evaluated.

4.3.3 Real topography and heterogeneous medium.

We evaluated the deformation pattern caused by a tensile dislocation embedded in a heterogeneous medium. Instead of using a simple multi-layered crustal rigidity model (Currenti et al., 2008a), a complex distribution of elastic medium properties was considered. At each node of the mesh different values of Young modulus and Poisson ratio are assigned on the basis of seismic tomography investigations. In this way, smooth elastic medium heterogeneities, instead of sharp boundary layers, may be included that are effectively most likely for many geological settings. Moreover, this procedure allow to better represent the presence of a high rigidity body centred below the SE sector, inferred from recent seismic tomography studies (Chiarabba et al., 2000; Patanè et al., 2002). We used P-wave and S-wave seismic velocities to derive the elastic medium parameters. Particularly, the

Young modulus was estimated by using the following equation (Kearey and Brooks, 1991):

$$E = 2V_s^2 \rho(1+\upsilon) \tag{4.4}$$

where V_s is the seismic shear wave propagation velocity, and ρ the density of the medium which was fixed to 2500 kg/m^3. Instead, the values of Poisson ratio were obtained using the equation (Kearey and Brooks, 1991)

$$\upsilon = \frac{(V_p/V_s)^2 - 2}{2(V_p/V_s)^2 - 2} \tag{4.5}$$

where V_p is the seismic P-wave propagation velocity. On the basis of Equations (4.4) and (4.5), the Young modulus varies from 12.9 GPa to 141 GPa (Figure 4.9), while the Poisson ratio is in the 0.12–0.32 range (Figure 4.10).

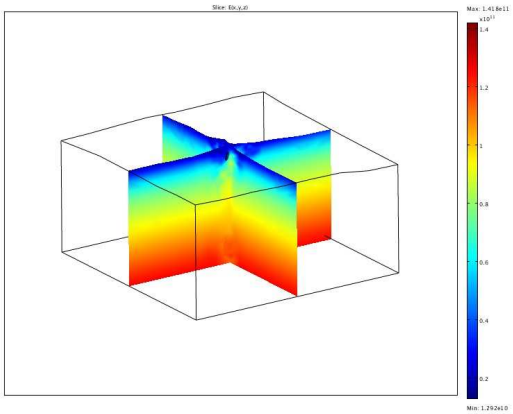

Figure 4.9. Young modulus distribution.

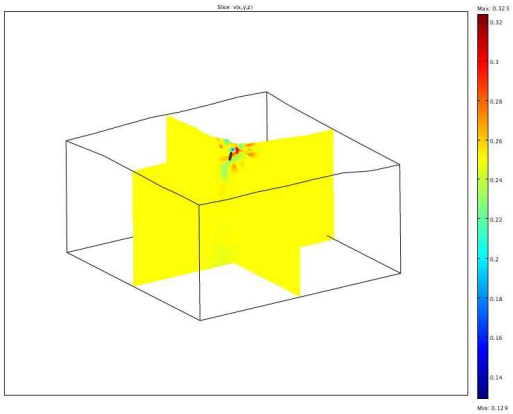

Figure 4.10. Poisson ratio distribution.

We considered three different media with: (a) homogeneous Young modulus and heterogeneous Poisson ratio, (b) heterogeneous Young modulus and homogeneous Poisson ratio, and (c) heterogeneous Young modulus and heterogeneous Poisson ratio. In

the (a) case where only the Poisson ratio is heterogeneous, the discrepancy with respect to the homogeneous model is negligible. The models with heterogeneous Young modulus are those that engender higher perturbations in the numerical models considering the inhomogeneity of medium properties. Nevertheless, results compared to homogeneous medium model do not reveal significant differences in pattern and intensity of the deformation field (Figure 4.11). The influences of the medium heterogeneity seem to affect mainly the horizontal components (Figure 4.11 a–b) with respect to the vertical uplift (Figure 4.11 c).

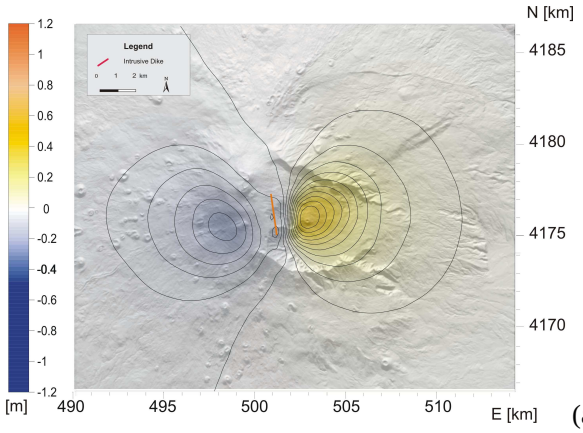

(a)

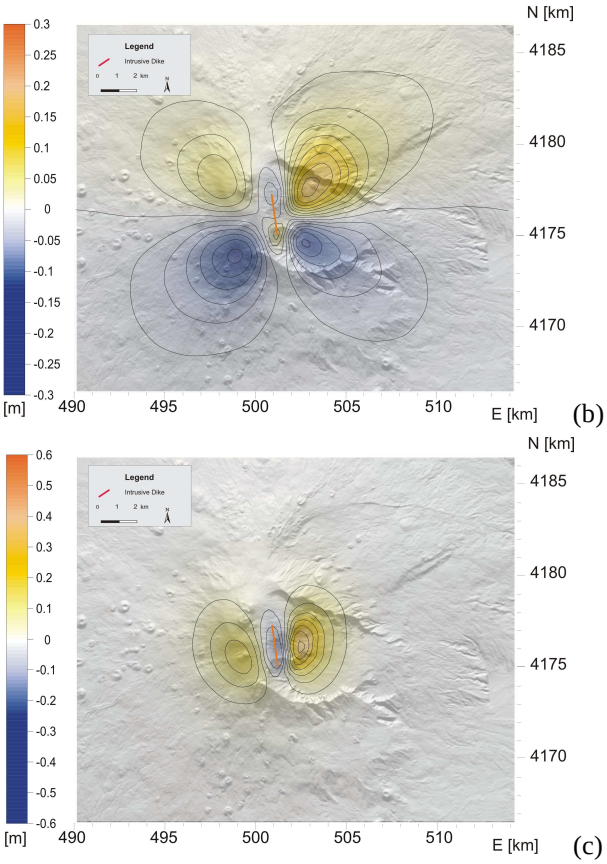

Figure 4.11. Deformation fields of the tensile crack in a heterogeneous medium with the real topography of Mt Etna: (a) eastern component, (b) northern component, (c) vertical uplift. Contour lines are at 0.05 m.

4.4 Rheological modeling

Most volcano deformation models developed to date assume that the Earth's crust behaves as a perfectly elastic solid and allow us to obtain a simple image of volcanic deformation sources. Over the last decades, elastic numerical models have con contributed to asses how medium heterogeneity and topography can influence ground deformation especially near the volcano summit (Cayol and Cornet, 1998; Williams and Wadge, 2000; Currenti et al., 2008a). All these mechanical deformation models based on an elastic rheology assumption have been successfully and widely applied to interpret geodetic data acquired on several volcanoes (e.g. Walsh and Decker, 1971; Yang et al., 1992; Okada and Yamamoto, 1991; Bonaccorso and Davis, 1999; Currenti et al., 2008a).

However, in volcanic regions, elastic rheology assumption is oftentimes an over simplification: in many cases elastic models seem to be unable to reproduce the observed uplifts unless unrealistic over-pressures are considered (e.g. Berrino et al., 1984). The elastic approximation is generally appropriate for small deformations of crustal materials with temperatures cooler than the brittle-ductile transition, between 300 °C and 500 °C depending mainly on composition and strain rate. Although elastic behaviour well describes the upper 10–15 km of the Earth's crust, in active volcanic zones anelastic behaviour is more appropriate to characterize the medium

around the magmatic sources, which at relatively shallow crustal levels can extensively perturb the geothermal gradient. In this section we describe some common approaches to model the elastic and anelastic behaviour. Our purpose is to outline the development of rheological models, going deeply in the rheological models adopted in the present work: spherical pressure source embedded in elastic and viscoelastic medium.

4.4.1 Elastic model

The elastic analytical solution of a point dilatation source embedded in an elastic and homogeneous half-space was proposed by Mogi (1958). The model well reproduces a finite spherical source if the source depth d is twice compared to the radius a (McTigue, 1987). The elastic displacements are described by the spherical source position, its radius a, and the pressure change ΔP :

$$U_i = \frac{3K + 4\mu}{2\mu(3K + \mu)} \frac{\Delta P a^3 x_i}{R^3} \quad with \quad i = 1,2. \tag{4.6}$$

$$U_z = \frac{3K + 4\mu}{2\mu(3K + \mu)} \frac{\Delta P a^3 d}{R^3} \tag{4.7}$$

where R is the radial distance from the source centre to the observation point.

The analytical solutions of displacement field in a elastic half-space were used to assess the accuracy of the numerical solutions

obtained by Finite Element Method. We assumed a pressurized spherical source located at 4 km depth with a radius a of 0.7 km and a step-like temporal increase in pressure of $\Delta P = 100MPa$ at $t = 0$. The source is embedded in a homogeneous half-space having Poisson ratio υ=0.25, total shear modulus G=30 GPa, fractional shear moduli μ_0=μ_1=0.5.

The numerical analysis needs to set some parameters that could affect the accuracy of the solution. In particular, the size of the computational domain and the size of the finite elements are to be accurately chosen. The domain was proved to be big enough to avoid numerical artefacts in the solution due to the finite boundary condition. We assumed free displacement values at the upper surface and zero displacement values at bottom and lateral boundaries. Since in numerical methods the size domain is finite, these boundary conditions are implemented by considering a domain big enough that the assumption of zero potential at the boundary does not affect the solution in the interested area.

We considered a 3D axi-symmetric model. In such a case a simpler two-dimensional domain can be considered by exploiting the symmetries. Hence, the number of nodes, in which the solution is computed, decreases significantly. This model was chosen to perform a coarser analysis and carry out several tests to assess the goodness of numerical solutions. The FEM model is made up of ~16,000 triangular elements of variable size, in axi-symmetric configuration. The domain extends 25 km horizontally from the source centre and 35 km below the surface, and well reproduces the conditions generally imposed to half-space models (vanishing stresses at infinity). We report the

horizontal and vertical displacement of the analytical and numerical model. The numerical deformation solution practically coincides with the analytical ones (Figure 4.12).

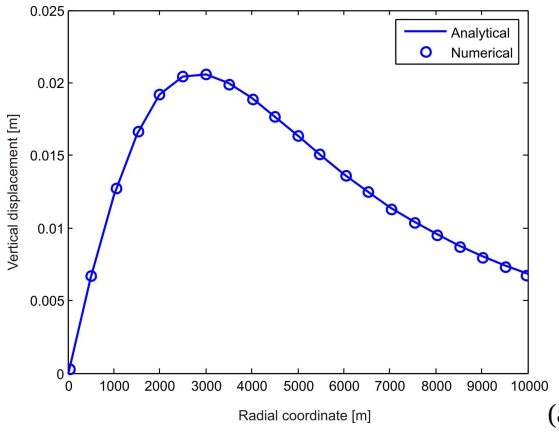

(a)

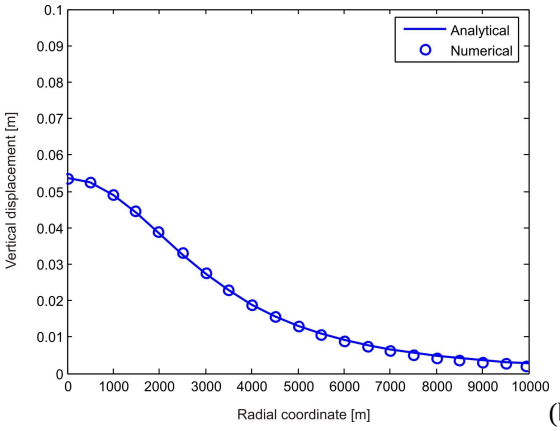

(b)

Figure 4.12. Comparison between analytical solutions (solid line) and numerical results (circles) for (a) horizontal and (b) vertical displacement due to a spherical pressure source in a homogenous elastic half-space.

4.4.2 Viscoelastic model

For a linear viscoelastic material, the analytical solution of the governing equations can be obtained employing the Correspondence Principle (Fung, 1965; Christensen, 1971), which allows to solve a linear viscoelastic problem using the associated elastic solutions, in which the elastic moduli are replaced by the Laplace transform complex moduli. The Correspondence Principle cannot be applied to a general thermo-viscoelastic problem, but it can be applied to thermo-rheologically simple materials, i.e. when the temperature dependence of mechanical properties is amenable to analytical description, and one of following conditions is satisfied: (i) the temperature field is spatially uniform but time-dependent; (ii) the temperature field has a spatial dependence but is independent of time (Christensen, 1982). If the analytic solution for the deformation field of any linear elastic model is given, we can apply the Correspondence Principle to the elastic solution to obtain the viscoelastic behaviour of deformation field. The Laplace transform of the viscoelastic solution $\tilde{W}_i(s)$ is given by

$$\tilde{W}_i(s) = \tilde{g}(s)\tilde{U}_i(s) \tag{4.8}$$

where $\tilde{g}(s)$ is the Laplace transform of the source time function *g(s)* giving the temporal evolution of the pressure amplitude, and $\tilde{U}_i(s)$ indicates the displacement function U_i in which the constant moduli are replaced with their Laplace transform moduli. The Laplace

transform of the shear modulus, which depends on the particular rheology considered, can be easily obtained using Equation (4.8) as

$$\tilde{\mu}(s) = \frac{G\tilde{Q}(s)}{2\tilde{P}(s)} \tag{4.9}$$

where $\tilde{Q}_i(s)$ and $\tilde{P}_i(s)$ are the Laplace transforms of Equations (2.6) and (2.7).

For a generalized Maxwell model with M Maxwell linear viscoelastic models in parallel, the Laplace transform of the shear modulus is:

$$\tilde{\mu}(s) = G\mu_0 + \sum_{i=1}^{M} \frac{s}{\frac{s}{G\mu_i} + \frac{1}{\eta_i}} \tag{4.10}$$

When the shear modulus has been defined and the elastic analytical solution is available, the resulting expression in Equation (4.10) must be inverted in order to obtain the viscoelastic solution for the displacement field in the time domain.

We derive the viscoelastic solution applying the Correspondence Principle to the elastic displacement equation (Equations (4.6) and (4.7)). Only the first term in Equations (4.6) and (4.7) $(3K + 4\mu)/2\mu(3K + \mu)$ depends on the rheology assumption. Adopting a generalized Maxwell rheology with one Maxwell model in

parallel and using Equation (4.10), the Laplace transform of the shear modulus is given by

$$\tilde{\mu}(s) = \frac{s(\mu_0 + \mu_1)G + \mu_0\mu_1 G^2/\eta}{s + \mu_1 G/\eta} \tag{4.11}$$

Since we assume that the viscous part of the deformation is incompressible, the bulk modulus $K = E/3(1-2\upsilon)$ is constant. As source time history, we consider a step-like increase in pressure amplitude at $t = 0$ on the source wall:

$$g(t) = \Delta P\, H(t) = \begin{cases} 0 & t < 0 \\ \Delta P & t \geq 0 \end{cases} \tag{4.12}$$

where $H(t)$ is the Heaviside function whose Laplace transform is $\Delta P / s$.

To derive the analytical viscoelastic solution we have to multiply the second term of Equations (4.6)-(4.7) with the inverse Laplace transform of the following equation:

$$\tilde{A}(s) = \frac{3K + 4\tilde{\mu}(s)}{2s\tilde{\mu}(s)(3K + 4\tilde{\mu}(s))}, \tag{4.13}$$

which is given by

$$A(t) = \frac{1}{2G_0}\left[\frac{3K + 4G_0\mu_0}{3K + G_0\mu_0} + \right.$$
$$\left. -3\frac{\eta G_0^2 e^{-\frac{G_0\mu_1(3K+G_0\mu_0)}{\eta(3K+G_0)}t}}{\eta(3K + G_0\mu_0)(3K + G_0)}(1-\mu_0) - \left(\frac{1}{\mu_0} - 1\right)e^{-\frac{G_0\mu_0\mu_1}{\eta}t}\right] \quad (4.14)$$

For the generalized Maxwell rheology, the viscoelastic response depends on time through two characteristic times:

$$\tau_1 = \frac{3K + G_0}{3K + G_0\mu_0}\tau_0 \quad (4.15)$$

$$\tau_2 = \frac{\tau_0}{\mu_0} \quad (4.16)$$

with $\tau_0 = \frac{\eta}{G_0\mu_1}$ the Maxwell time.

To assess the accuracy of the numerical solutions obtained by Finite Element Method we compare the analytical solutions of displacement field in a viscoelastic half-space with the numerical ones. We consider a 3D axi-symmetric model which geometrical and elastic parameters and boundary conditions are the same of those used in the elastic model (see previous section). We choose a fractional shear moduli of $\mu_0=\mu_1=0.5$ and a viscosity of $\eta = 2\times10^{16}\,Pas$ giving

characteristic times $\tau_0 = 1.33\times10^6 s$, $\tau_1 = 1.45\times10^6 s$ and $\tau_2 = 2.66\times10^6 s$.

Benchmark tests were carried out on the axi-symmetric models in order to verify the accuracy of the numerical solution. For the sake of simplicity, we report only the vertical displacements but similar results are achieved for horizontal displacements. The viscoelastic solution at *t=0* coincides with the elastic solution. Subsequently, the deformation grows exponentially approaching a finite value. The numerical deformation solution practically coincides with the analytical ones (Figure 4.13). This result allowed to validate the numerical technique used in these computations. The ground deformation of the viscoelastic model is enhanced with respect the elastic solution.

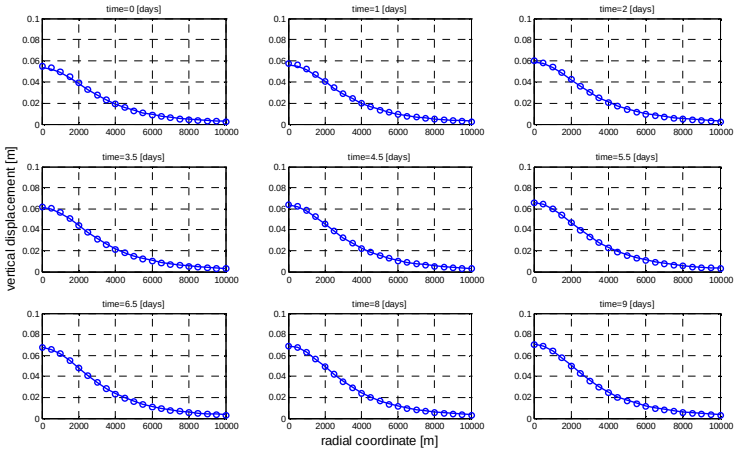

Figure 4.13. Comparison between analytical solutions (solid line) and numerical results (circles) for the vertical uplift due to a spherical pressure source in a homogenous and viscoelastic half-space.

We also simulated a pressure source that evolves following a trapezoidal source history instead of a step-like source function. Trapezoidal shape function describes the pressurization followed by depressurization of the magmatic source, usually observed in volcanic areas. The source history increases linearly in time from 0 to ΔP for t ranging between 0 and t1, remains constant to ΔP for $t_1 \le t \le t_2$, and finally decreases from ΔP to 0 for $t_2 \le t \le t_3$:

$$g(t) = \Delta P\left\{\frac{t}{t_t}\left[1 - H(t-t_1)\right] + H(t-t_1) - H(t-t_2) + \right.$$
$$\left. + \frac{t_3 - t}{t_3 - t_2}\left[H(t-t_2) - H(t-t_3)\right]\right\} \qquad (5.2)$$

whose Laplace transform is

$$\tilde{g}(s) = \frac{\Delta P}{s^2}\left(\frac{1 - e^{-st_1}}{t_1} + \frac{e^{-st_3} - e^{-st_2}}{t_3 - t_2}\right) \qquad (5.3)$$

We further derived the analytical solution and compared it with the numerical one. As shown in Figure 4.14, the numerical solution is nearly identical to the analytical one.

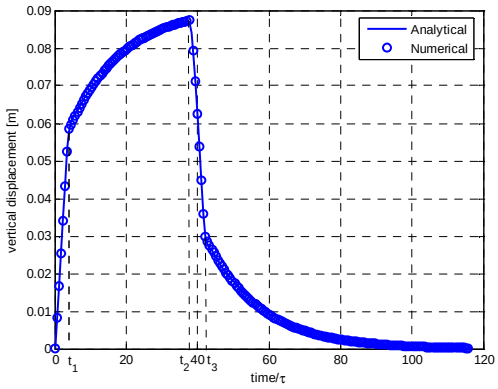

Figure 4.14. Comparison between analytical solution (solid line) and numerical result (circles) for the ground uplift as a function of time. A trapezoidal source history is assumed with $t_1=\tau_0/2$, $t_2=5\tau_0$, and $t_3=5.5\tau_0$. The pressure reaches 100MPa.

Chapter 5

Modeling of ground deformation

The correct identification and interpretation of the sources of a wide spectrum of geophysical signals associated with eruptive and seismic activity is the principal goal of modeling in geophysics.
The main task of geophysics is to reveal quantitatively the structure and dynamics of the volcanoes and seismogenetic areas. Over the last decades, geophysical studies have been evolving from an empirical to a more quantitative approach in the study of processes. Within this framework, new modern techniques of monitoring have been implemented in order to mitigate the volcanic and seismic hazard and to improve the knowledge of eruptive processes and earthquakes.

Field measurements are the starting point for the geophysics process understanding. A popular instrument that has long been used to detect changes in the slopes of volcanoes is called a tiltmeter. A tiltmeter is placed on the slope and a small container filled with fluid measures how much the tilt of the slope changes. More recently,

satellites have been used to monitor changes in slope. For example, Global Positioning System (GPS) instruments have been installed on volcanoes and linked to satellites orbiting our planet. When a surface deforms, the changes in position of these GPS instruments is detected by the satellites and the exact amount and direction of movement can be calculated.

However, field data alone are not enough for making any quantitative interpretation, but in addition theoretical responses (model responses) are needed and for realistic models. This makes modeling so important and basic area in geophysical research. In this thesis several case study were presented. They both investigated post-seismic and pre-eruptive processes using a FE models.

Earthquakes are caused mostly by rupture of geological faults, but also by volcanic activity, landslides, mine blasts, and nuclear experiments. In this thesis were analyzed tectonic earthquakes, which occur anywhere within the earth where there is sufficient stored elastic strain energy to drive fracture propagation along a fault plane. In the case of transform or convergent type plate boundaries, which form the largest fault surfaces on earth, they will move past each other smoothly and aseismically only if there are no irregularities or asperities along the boundary that increase the frictional resistance. A real Case study on the Landers and Hector Mine Californian earthquakes was presented.

Volcanic activity is caused by the ascent of magma to the Earth's surface and its eruption. Active magmatic systems interact strongly with their surroundings, causing ground deformation, material failure and other effects such as disturbed groundwater

systems and degassing. These processes and interactions lead to geophysical and phenomenological effects, which precede and accompany eruptions. The term volcanic source is a simplification here referred to the cause responsible for the variations in the geophysical observations. There are a lot of mechanisms connected with magma rise and accumulation, in this thesis two principal kinds of volcanic sources were treated: the dislocation sources and the pressure sources. Several applications on Etna volcano were presented.

5.1 Dislocation sources: faults

In geology a fault, or fault line, is a planar rock fracture which shows evidence of relative movement. Large faults within the Earth's crust are the result of differential or shear motion and active fault zones are the causal locations of most earthquakes or they could lead to geophysical effects, which precede and accompany eruptions.

The two sides of a non-vertical fault are called the hanging wall and footwall. By definition, the hanging wall occurs above the fault and the footwall occurs below the fault. Faults can be categorized into three groups based on the sense of movement (slip) : (i) Dip-Slip, (ii) Strike Slip and (iii) Tensile Slip Faults.

(i) Dip-slip faults can be again classified into the types "reverse" and "normal". A normal fault occurs when the crust is extended. Alternatively such a fault can be called an extensional fault.

The hanging wall moves downward, relative to the footwall. A downthrown block between two normal faults dipping towards each other is called a graben (Figure 5.1). An upthrown block between two normal faults dipping away from each other is called a horst. Low-angle normal faults with regional tectonic significance may be designated detachment faults. A reverse fault is the opposite of a normal fault i.e. the hanging wall moves up relative to the footwall. Reverse faults are indicative of shortening of the crust. The dip of a reverse fault is relatively steep, greater than 45°.

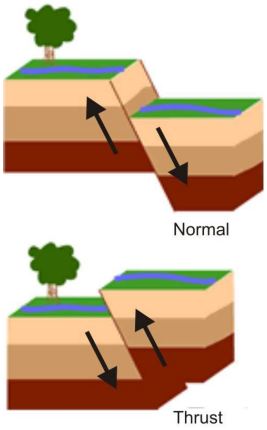

Figure 5.1. Dip-slip faults.

(ii) A fault is known as a transcurrent or strike-slip fault when the main sense of slip is horizontal (Figure 5.2). Strike-slip faults with left-lateral motion are also known as sinistral faults. Those with right-lateral motion are also known as dextral faults. A special class of strike-slip faults is the transform faults which are a plate tectonics feature related to spreading centres such as mid-ocean ridges.

Oblique-slip faults have significant components of both strike and dip slip.

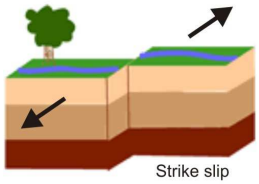

Figure 5.2. Strike-slip faults.

(iii) A classic mechanism of magma uprising is related to intrusive processes characterizing the emplacement of dikes. A dike can be represented by an opening fault (tensile slip) (Figure 5.3). Tensile dislocation theory has been applied with success to the case of a rectangular shaped source with tensile opening in an elastic homogeneous half-space (Okada, 1985; Yang and Davis, 1986). The application of dislocation theory to the case of tensile mechanisms has often been used in the last ten years and applied successfully to the study of ground deformations (e.g., Yang et al., 1992).

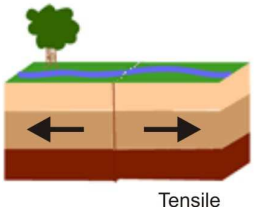

Figure 5.3. Tensile faults.

5.1.1 Case study: intrusive event forerunning the 2001 Etna eruption

The numerical modeling procedure is applied to study the ground deformation observed during the Etna 2001 eruption. Late night on 12 July 2001 an intense seismic swarm preceded and accompanied the opening of a system of fractures at the base of the South–East (SE) crater and continued without any fall in energy release till the late night of July 16. Some 800 earthquakes were recorded by the early morning of July 13, from a total of 2645 occurring between 12 and 18 July (Patanè et al., 2002). In concomitance with the seismic crisis, marked ground deformation (50–120mm) was recorded at the GPS permanent stations. Tilt variations were very small in the northern flank, of few μ-rad in the 177 western flank, and much more marked at stations close to the fracture field (Bonaccorso et al., 2002). The deformation was mainly cumulated during the late night of July 12 and the following two days. Bonaccorso et al. (2002) modelled the ground deformation changes recorded in the days before the eruption onset (between July 11 and 16) by means of analytical solutions. The tilt and GPS data inversion indicated the response to a tensile mechanism with an opening dislocation of ca. 3.5 m that evidenced an intrusion in the volcano edifice along a ca. N–S direction (Bonaccorso et al., 2002). The location of the tensile source lies within the zone of the seismic swarm that occurred during the magma ascent. Although the analytical model provided an acceptable representation of the dyke intrusion occurred on the south flank, it is not able to justify all the details. The simplified assumption of elastic half-space medium disregards effects

caused by the topographic relief and the presence of medium heterogeneity, while they could play a role in the modeling procedure. To evaluate how the topography and medium heterogeneity could affect the computed ground deformation, we carried out numerical models including the real topography of the volcano edifice and the medium heterogeneity inferred from seismic tomography study.

5.1.1.1 Numerical computations

In the numerical computations we used the source geometry (Table 5.1) obtained by the analytical inversion model from Bonaccorso et al. (2002) and we evaluated the deformation pattern caused by a tensile dislocation embedded in a heterogeneous medium applying at each node of the mesh different values of Young modulus and Poisson ratio assigned on the basis of seismic tomography investigations and including real topography of the volcano edifice. A computational domain of 50 km × 50 km × 35 km is meshed with ~35000 tetrahedral elements.

Table 5.1. Geometrical parameters of the dislocation source.

Dislocation **B** [m]	3.5
Length L [m]	2200
Width [m]	2300
Depth of top d [m]	1400 a.s.l.
Inclination angle δ [°]	90
Strike angle θ [°]	7

We considered three different media with: (a) homogeneous Young modulus and heterogeneous Poisson ratio, (b) heterogeneous Young modulus and homogeneous Poisson ratio, and (c) heterogeneous Young modulus and heterogeneous Poisson ratio.
To better appreciate the discrepancies of the numerical models with respect to the analytical ones, we compared the displacement field at the locations of GPS continuously running stations.

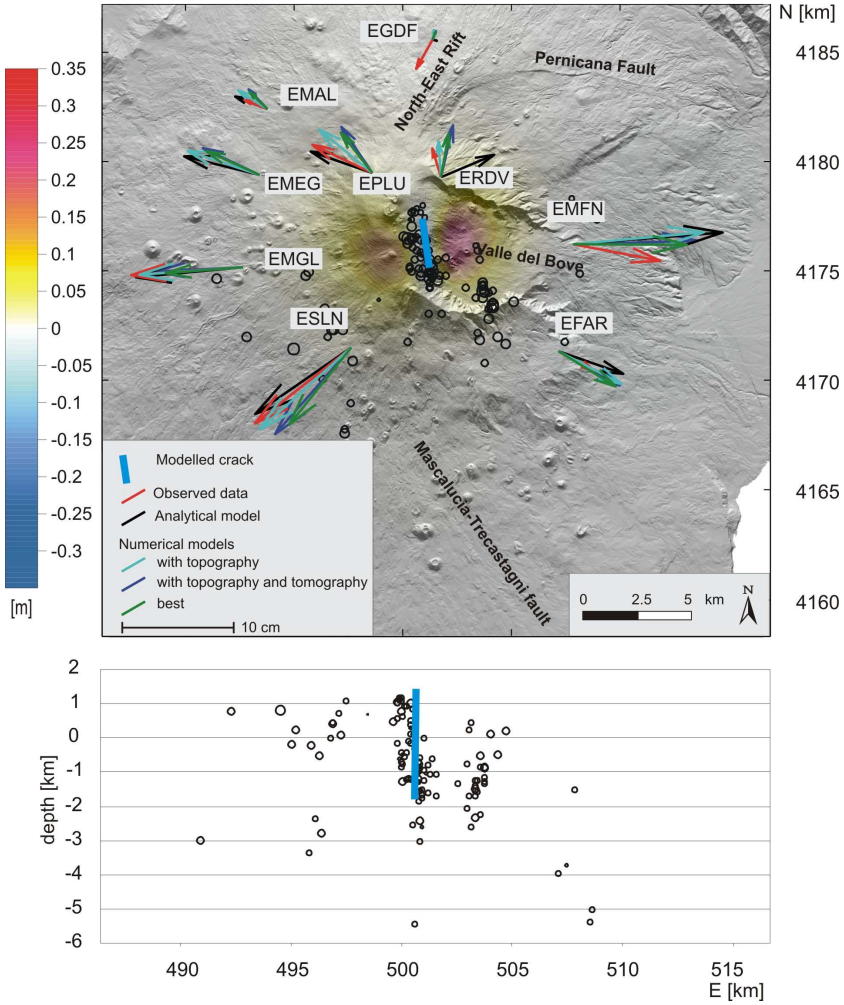

Figure 5.4. Observed and expected horizontal displacements at the GPS stations between 11 and 16 July 2001. The vertical uplift, computed by the "best" numerical model using real topography and medium heterogeneity, is shown. The black circles represent the epicenters of the seismic event accompanying the dyke intrusion (after Musumeci et al., 2004).

Figure 5.4 shows the horizontal component of GPS data together with results achieved by the numerical models. The observed vectors are obtained from the interval comparisons 11–16 July before the eruption onset. Discrepancies of at most a few cm between the numerical and analytical models are observed at the GPS stations (Figure 5.4). In fact, almost all the GPS stations are located far enough from the summit area and are not significantly affected by the topography. A more general agreement is achieved with respect to the deformation computed from the analytical model at ERDV station. Nevertheless, a higher discrepancy with respect to the observed deformation still remains at the EMFN station on the eastern flank of the volcano and at EGDF on the northern flank. Both the topography and medium heterogeneity included in the numerical model cannot account for the displacements observed by the EMFN and EGDF geodetic stations.

Among the considered models, a good match is achieved by the model including only the topography (cyan arrows in Figure 5.4). The residuals, the difference between observed field and numerical solutions, show a standard deviation: of 2.3 cm for the analytical model, of 1.7 cm for the numerical model with topography, and of 2.0 cm for the numerical model including the topography and the medium heterogeneity. When the tomography is included in the numerical model the residual increases. The topography is known with higher resolution and accuracy, whereas the medium heterogeneity is estimated from the 3D velocity model. Three factors can alter this estimate: (i) the low spatial resolution of 3 km in the tomography model by Chiarabba et al. (2000), (ii) the variation of 3D velocity

model in the analyzed period, (iii) the difference between the static elastic modulus and the dynamic elastic modulus deduced from the P-wave velocity. Recently, Patanè et al. (2006) obtained new 3D velocity models at higher resolution on Mt Etna, detecting significant variations in the elastic parameters during different volcanic cycles. Further comparisons of different 3D velocity models could showup how the accuracy on medium heterogeneity can affect the numerical solutions.

5.1.1.2 Parameters space investigation

It is worth to note that we adopted source parameters from analytical inversion of GPS data by Bonaccorso et al. (2002). To enhance the match between the data and the numerical solution including topography and medium heterogeneity, we performed an exploration through the parameter space varying the width, the depth and the opening of the dyke. The range of variability of these parameters was also chosen on the basis of the location of the seismic swarm accompanying the dyke intrusion (Figure 5.4, Musumeci et al., 2004). The earthquakes were quite shallow from 1000 m a.s.l. to 2000 m b.s.l.. Starting from the parameter suggested by the analytical inversion (Bonaccorso et al., 2004), we performed a grid search on the numerical model, which includes both the topography and the medium heterogeneity, varying the width within 2000–3000 m, the opening within 2–4 m and the depth within 0–1400 m a.s.l.. The residuals show a variation range of 2.5 cm with a minimum of 1.9 (Figure 5.5).

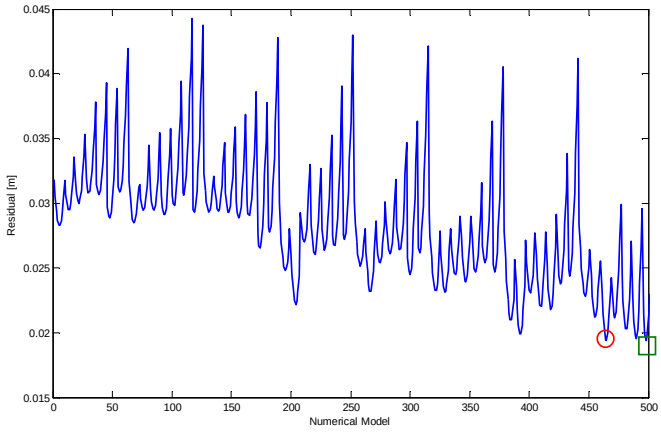

Figure 5.5. Residuals between the observed ground deformation and numerical solutions. The circle represents the numerical model with source parameters coming from the analytical inversion, while the square is the "best" numerical model (with minimum residual).

The "best" model, associated with the minimum residual, has an opening of the dyke of 2.5 m, a width of 3000 m, and a depth of 1400 m, that well matches the hypocenters of the seismic events occurred during its intrusion (Figure 5.4). However, the best solution does not differ too much with respect to the numerical solution obtained using the dyke parameters inferred from the analytical inversion. Even if the parameters vary in a wide range, the solutions for all the considered models computed at the GPS stations are quite similar. The standard deviation affecting measurements in the horizontal components ranges between 0.2 and 0.5 cm while, over measurements in the vertical component, between 1 and 2 cm (Bonaccorso et al., 2003). Thus, a maximum uncertainty of ±1 and ±4 cm at the 95% confidence interval

can be assumed over the horizontal and vertical component, respectively. Therefore, considering the measurement errors and the computed misfit values, all the numerical models can be assumed as valuable solutions.

We also computed the sensitivity of fit to the "best" numerical model for the depth and width parameters (Figure 5.6). The sensitivities with respect to these parameters evaluated at the GPS stations are continuous decreasing functions with residuals from 0.2 to 1.6 cm.

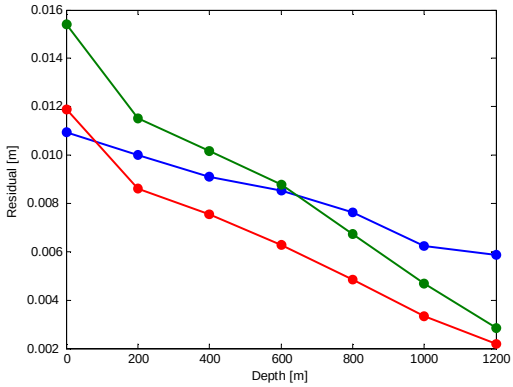

(a)

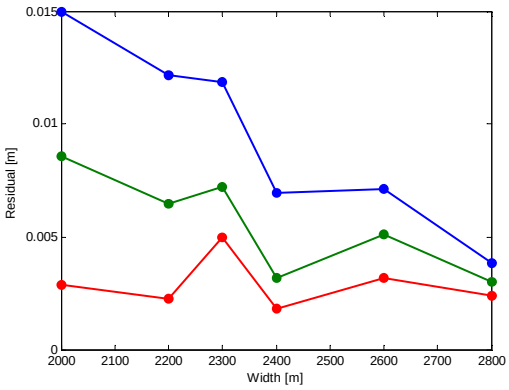

(b)

Figure 5.6. Sensitivity of fit to (a) depth and (b) width parameters of the intrusive dyke. The residuals on the *x*-component (blue line), the *y*-component (green line), and vertical uplift (red line) are computed at the locations of GPS stations.

The low residuals and the sensitivity values point out that it is not possible to better constrain the depth and width parameters of the dyke only on the basis of ground deformation at the available GPS stations. To understand whether this uncertainty is due to the far location of the GPS stations or to the inherent ambiguity of the used model, we recomputed the sensitivities functions over a grid of points extending 10 km × 10 km around the source (Figure 5.7). In this case, the depth sensitivity increases, while the width sensitivity is almost unchanged. Therefore, a better coverage of the summit area could enhance the capability to constrain the source depth.

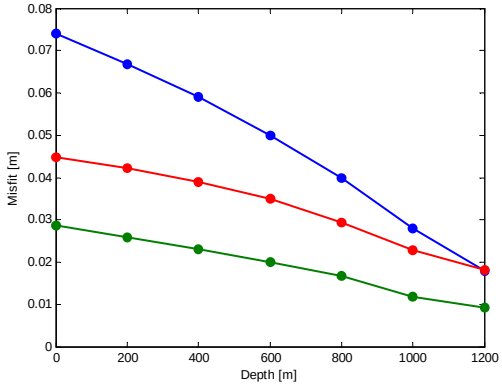

(a)

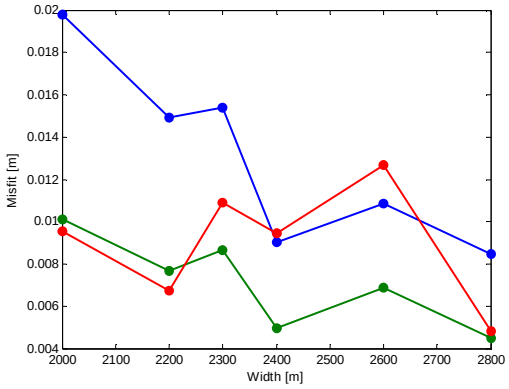

(b)

Figure 5.7. Sensitivity of fit to depth and width parameters of the intrusive dyke. The residuals on the *x*-component (blue line), the *y*-component (green line), and vertical uplift (red line) are computed over a grid extending 10 km × 10 km at the ground surface around the source.

5.1.1.3 Conclusions

3D finite elements models were carried out in order to evaluate the ground deformation produced by dip-slip, strike-slip and tensile dislocation sources. The numerical results were compared to

analytical solutions from Okada's dislocation theory for validating their accuracy. The FEM technique enabled to consider both the topography and the medium heterogeneity in modeling the intrusive event occurred at Mt Etna in July 2001. The topography significantly alters the general pattern of the ground deformation especially near the volcano summit. On the contrary, the medium heterogeneity does not strongly affect the expected deformation. Several computations were performed to better understand the effects induced by the numerical model. We explored the source parameter space with a grid search. In comparison to the analytical solution, the numerical model associated with the minimum residual provides tensile source with a reduced opening and a wider extension which well matches the hypocenters of the seismic swarm occurred during the dyke intrusion. However, this numerical model does not differ too much from the analytical one. The numerical and the analytical solutions are both valuable solutions given the measurement errors and the location of GPS stations. A good match between the observed and the computed deformation was achieved at most stations. An exception is represented by the EMFN station located within the Valle del Bove in the eastern flank, and EGDF station located near the North East Rift. The numerical model is not able to account for the higher discrepancies at the EMFN station. Therefore, the heterogeneity and the topography cannot give an explanation for the displacement observed on the eastern flank. Indeed, the response of the eastern flank of the volcano to the intrusive event is more composite because of the presence of intricate geological structures. The eastern sector is confined in the northern flank by the North-East Rift zone and by the East-West trending left

lateral-transtensive Pernicana fault (Figure 5.4), while the southern sector is delimited by the Mascalucia-Trecastagni fault system (Rasà et al., 1996). The EGDF and EMFN stations are closer to these geological structures that are not taken into account into the numerical model. A new model should be set up including these discontinuity surfaces to better draw the complex interaction between the magmatic intrusions and the tectonic processes responsible for the kinematics of the eastern flank.

5.1.2 Case study: Post-seismic deformation following the 1992 M 7.3 Landers and 1999 M 7.1 Hector Mine, California earthquakes

We propose a fully 3D viscoelastic model for describing the postseismic relaxation following both the M. 7.3 1992 Landers and M. 7.1 1999 Hector Mine earthquakes. Landers earthquake occurred in the Mojave Desert, rupturing the northwest-trending Bullion and Lavic Lake faults, which are part of the eastern California shear zone (ECSZ) (Scientists of the USGS et al., 2000; Treiman et al., 2002, Simons et al., 2002, Sieh et al., 1993). The tectonically active ECSZ is believed to accommodate about 15% of the relative motion between the North American and Pacific plates, with an estimated strain accumulation rate of the order of 1 cm/yr across the 80-km-wide shear zone (e.g., Sauber et al., 1986; Dokka and Travis, 1990). The Landers earthquake was followed soon after by the nearby (about 20 km to the est) 1999 M7.1 Hector Mine quake (Figure 5.8). Such a close temporal and spatial proximity has raised the question of a possible causal relationship between these earthquakes (Parsons and Dreger,

2000; Scientists of the USGS et al., 2000; Freed and Lin, 2001). Both the Landers and Hector Mine earthquakes initiated robust aftershock sequences, as well as triggering seismicity as far as several hundred kilometres from the rupture plane (Hauksson et al., 2002). Before addressing the relationship between these two earthquakes we must first construct the most reliable postseismic slip model.

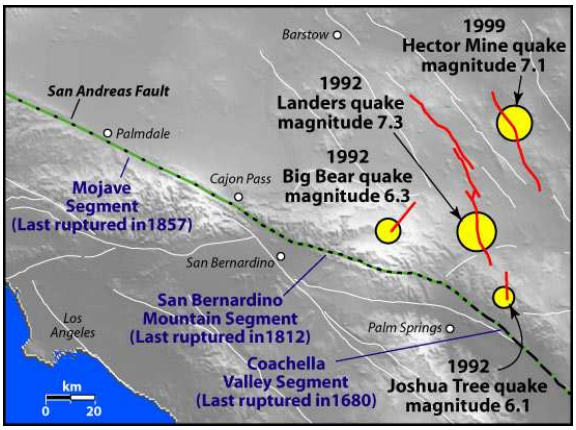

Figure 5.8. Tectonically active eastern California shear zone (ECSZ).

Recent advances in remote sensing, in particular of dense Global Positioning System (GPS) networks permit us to form high-resolution maps of earthquake-induced surface deformation at a centimetre-scale accuracy. Postseismic deformation was recorded at an extensive array of continuous GPS stations that span a very broad region of southern California and into Nevada (more than 200 km from the epicentre) (Figure 5.9).

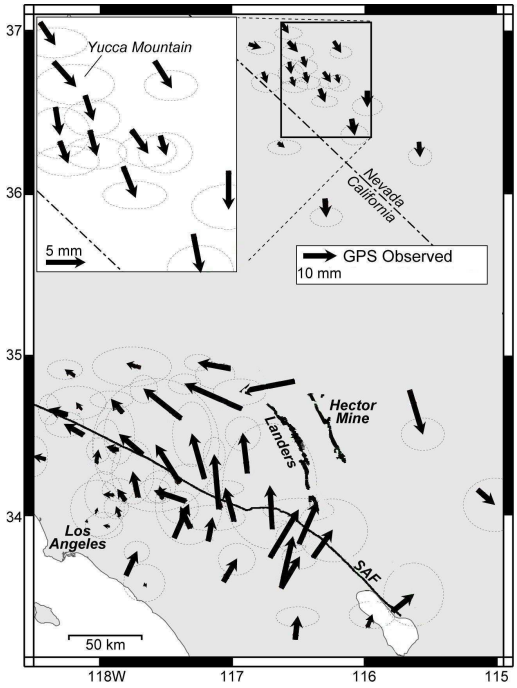

Figure 5.9. Cumulative GPS observed postseismic horizontal surface displacements (transient component) for the 7 year period following the 1999 Hector Mine earthquake (after Freed et al., 2007).

5.1.2.1 Observational Constraints and modeling approach

Seven years of cumulative transient deformation resolves a broad postseismic response (Figure 5.9) to the 1999 M7.1 Hector Mine earthquake, as well as continued deformation from the nearby 1992 M7.3 Landers earthquake. The postseismic response reaches the vicinity of Yucca Mountain, Nevada, more than 200 km from the Hector Mine epicentre (Figure 5.9, inset). To describe the mechanism

responsible for this deformation pattern we use a 3-D viscoelastic finite element model of the Mojave region that incorporates both rupture surfaces (Figure 5.10, inset). The computational domain was set up to a large volume extending 600 km × 600 km ×120 km including the areas of Yucca Mountain. It was represented by number of 1629800 arbitrarily distorted tetrahedral elements connected by 283761 nodes. The mesh resolution is about 500 m around the Landers and Hector Mine faults and decreases to 50 km in the far field (Figure 5.10). We use the inferred coseismic slip distribution of Fialko (2004b) for the Landers earthquake, and that of Simons et al. (2002) for the Hector Mine earthquake (Figure 5.11), as well as the same layered elastic structure (Figure 5.12).

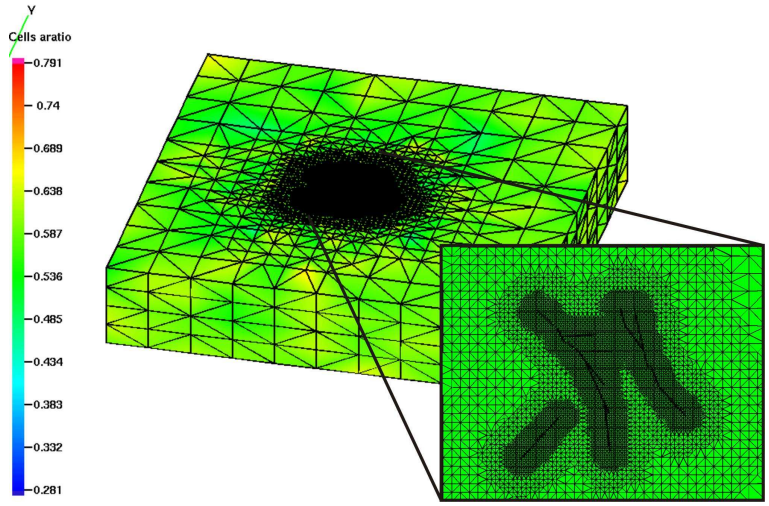

Figure 5.10. Computational domain which incorporates Landers and Hector Mine rupture surface. Colors refer to the quality of the mesh.

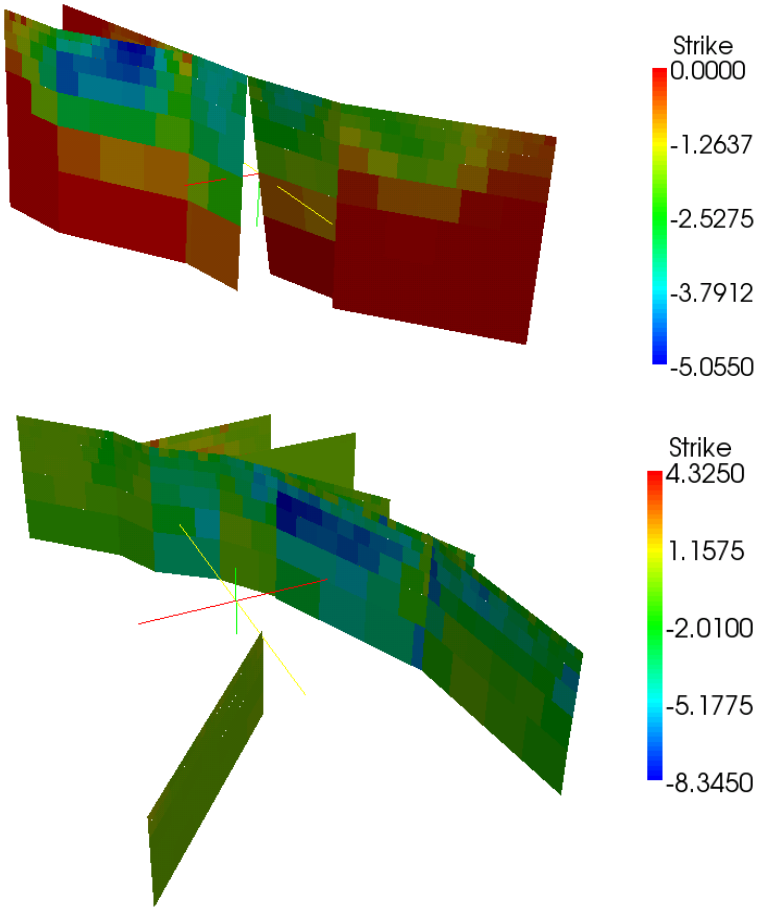

Figure 5.11. Strike-slip distribution for (a) Hector Mine and (b) Landers faults from Fialko (2004b) and Simons et al. (2002).

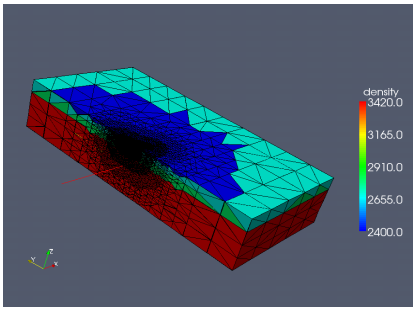

(a)

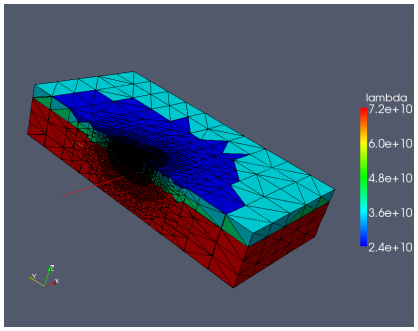

(b)

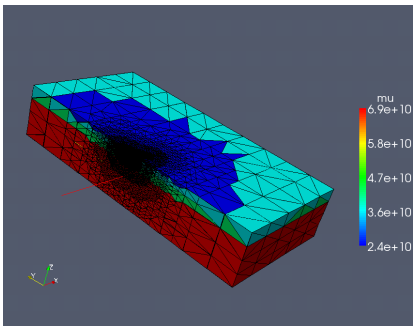

(c)

Figure 5.12. The layered elastic structures: (a) Density, (b) Lambda, (c) μ.

Considering a layered viscoelastic rheology (Figure 5.13), we first

simulate the Landers rupture, allow the rheology to respond to these stress changes for 7 years, then simulate the Hector Mine rupture and allow the rheology to respond for another 7 years (Figure 5.14).

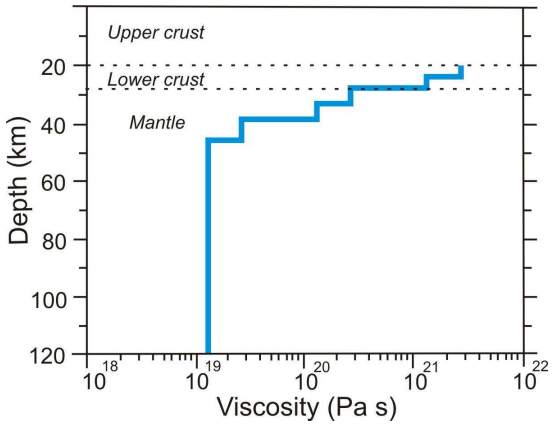

Figure 5.13. The layered viscoelastic rheologhy (after Freed et al. 2007).

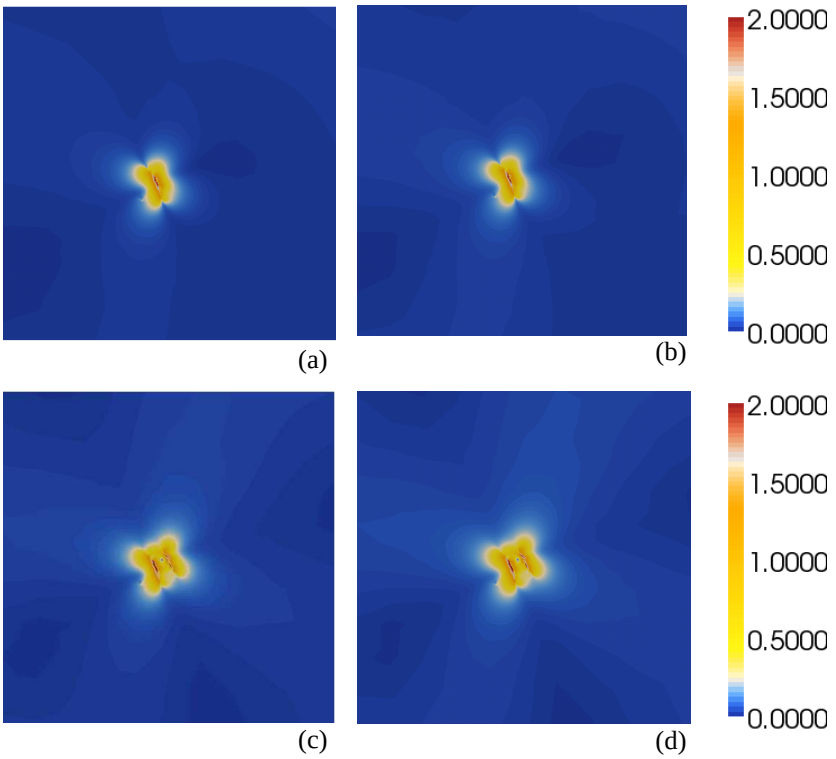

Figure 5.14. Ground response after (a) 0 year, (b) 6 years, (c) 7 years, and (d) 14 years.

Figure 5.14a shows the elastic response of the medium after Landers earthquake. After 6 years the effects of viscoelastic rheology modifies the deformation pattern (Figure 5.14b). The Hector Mine earthquake was simulated in the seventh year, Figure 5.14b shows the combined effects of deformation due to the viscoelastic response of the medium to the Landers earthquake and due to the elastic response after Hector Mine shock. Figure 5.14d shows the effects of

viscoelastic relaxation after 14 years. The time-dependent ground deformation caused by seismic faulting in a benchmark station is shown in Figure 5.15. The effect of the Hector Mine rupture faulting at time t=7 years is clear in the discontinuity of the horizontal and vertical displacements.

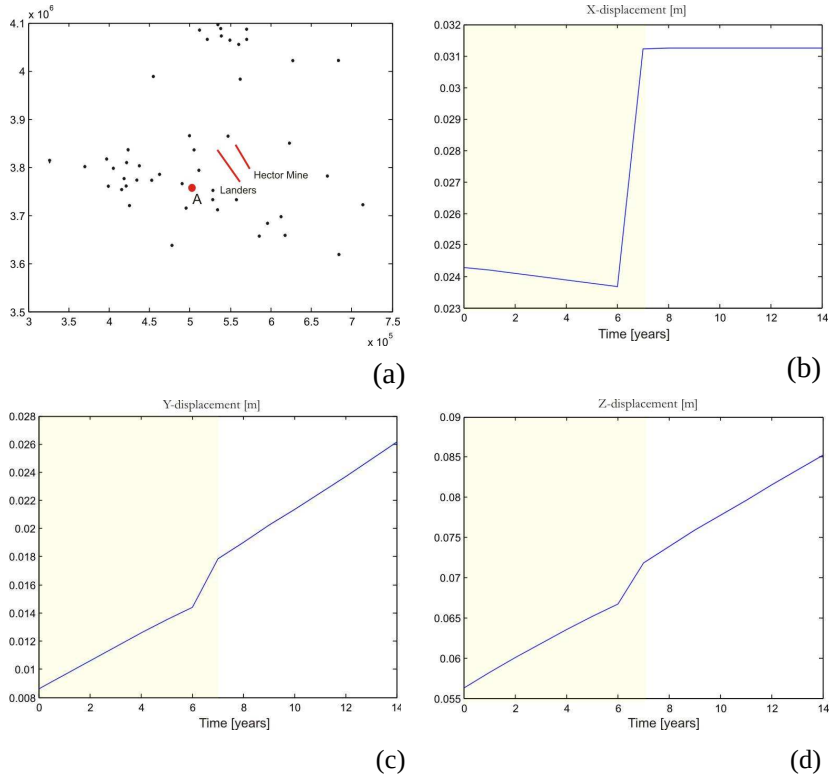

Figure 5.15. (a) GPS station location map. Time dependent vertical (b)-(c) and horizontal (d) displacement at station A.

Calculated cumulative postseismic model displacements over this latter 14-year period are compared to those observed to test the

hypothesis of viscoelastic rheology. Figure 5.16 shows the horizontal component of GPS data together with results achieved by the elastic and viscoelastic numerical models. The observed vectors are obtained from cumulative GPS observed postseismic horizontal surface displacements (transient component) for the 7 year period following the 1999 Hector Mine earthquake. Discrepancies of at most a few cm between the GPS observed and viscoelastic numerical model are observed in areas of Yucca Mountain. A more general agreement is achieved with respect to the deformation observed from GPS stations at near and middle field areas.

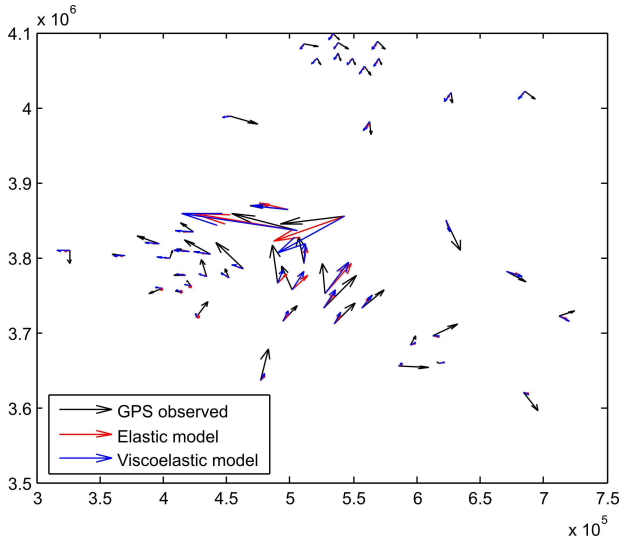

Figure 5.16. Comparison between GPS observed (black), elastic (red) and viscoelastic (blue) deformation.

5.1.2.2 Conclusions

3D finite elements models were carried out in order to evaluate postseismic relaxation of ground deformation following both the Landers and Hector Mine earthquakes.

The numerical results were compared to those observed from GPS stations, a good match between the observed and the computed deformation was achieved at most stations in the near and middle field areas but a disregard still appear in the far field area.

New models should be set up including different rheologies like power–law rheology and different mechanisms like the after-slip model in order find a better match with the observed GPS stations. These models could help us to discover the dominant mechanism that best explains the post-seismic deformation and to provide a better understanding of the rheological properties of the lithosphere.

5.2 Pressure sources

Magma rises through fractures from beneath the crust because it is less dense than the surrounding rock. When the magma cannot find a path upwards it pools into a magma chamber. As more magma rises up below it, the pressure in the chamber grows. This phenomenon is commonly ascribed to a pressure source that describes the effect of dilatation caused by accumulation of magma or gas in a reservoir. Since these areas where magma accumulates before eruption are

probably much more complex than anything having the simple shape of a "chamber", it is more appropriate to talk of "magma storage areas" or "magma reservoirs". Variation of the geometrical and physical characteristics of pressure sources determines the distribution and intensity of the stress and displacement field in the volcanic edifice (Figure 5.17).

A variety of mechanisms have been proposed in the past: one of the first and probably the most employed was proposed by Mogi (1958), who studied the response of a homogeneous, isotropic and elastic half-space to a isotropic dilatation point in axi-symmetric geometry. A more general reservoir description is the 3-D point-source ellipsoidal cavity studied by Davis (1986). The pressure sources was analyzed as a system of double forces of unequal magnitude, located at the ellipsoid centre, such that the resulting normal pressure on the inner side of the cavity is uniform.

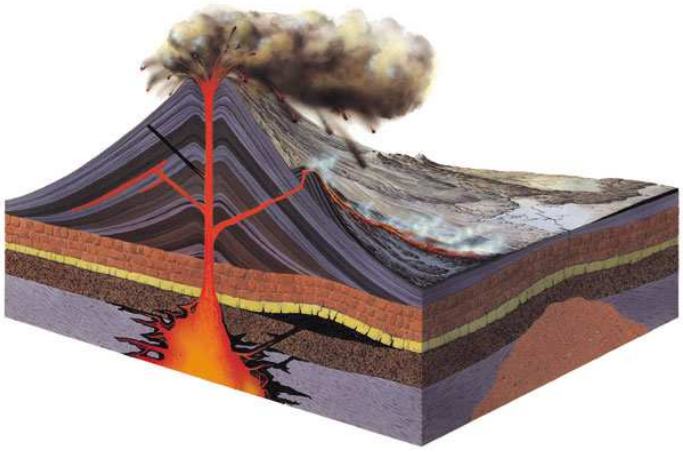

Figure 5.17. Illustration of a volcano plumbing system.

5.2.1 The 1993–1997 inflation period on Etna volcano

We use the Finite Element Method performing a fully 3D formulation to study the long-term deformation observed at Mt Etna in 1993–1997 period. Etna is one of the better monitored and successfully studied volcanoes in the world, where continuously running geodetic networks are operating (Bonaccorso and Davis, 2004). Since 1993, different geodetic techniques (EDM, GPS, SAR and leveling data) identified an inflation phase characterized by a uniform expansion of the overall volcano edifice. The beginning of the inflation phase was detected from the comparison of SAR images covering the 1993–1995 time interval (Figure 5.18). The inversion of interferograms required the inflation from a spheroidal magmatic source located at about 5 km b.s.l. (Lundgren et al., 2003). Also levelling data (Figure 5.19) supported the presence of a pressurized spherical source beneath the summit craters at 4.5 km b.s.l. (Obrizzo et al., 2004). Recently, Bonaccorso et al. (2005) interpreted the 1993–1997 GPS and EDM (Figure 5.20) data by a pressurized ellipsoidal source using a numerical elastic model. In order to reproduce the observed displacements, an effective overpressure of about 320 MPa was needed, which is exceedingly high. The inclusion of a realistic anelastic component could significantly lower the inferred pressure necessary to explain the observed surface deformation (Newman et al., 2006).

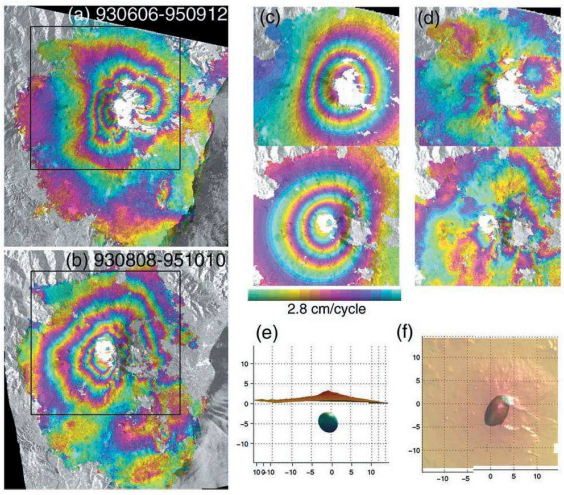

Figure 5.18. SAR images covering the 1993–1995 time interval on Mt. Etna, from Lundgren et al., 2003.

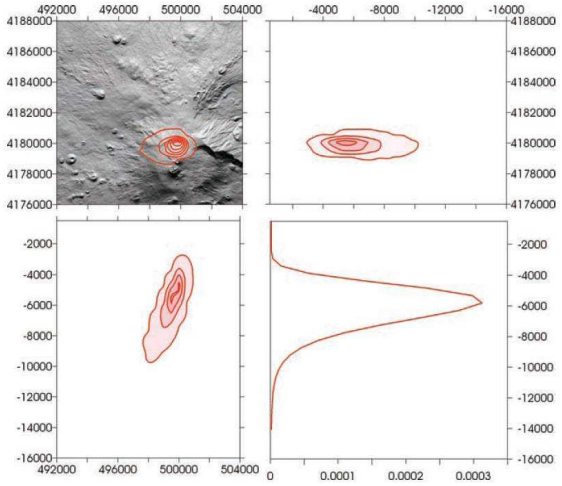

Figure 5.19. Levelling data recorded at Mt. Etna during the 1993–1995 time interval, from Obrizzo et al. 2004.

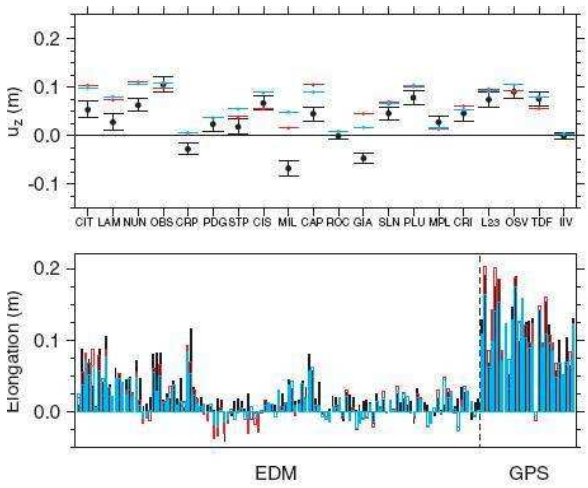

Figure 5.20. GPS and EDM recorded at Mt. Etna during the 1993–1995 time interval, from Bonaccorso et al. (2005).

We propose a thermo-mechanical numerical model for evaluating the temperature dependency of the anelastic solution. We considered two different behaviours: (i) viscoelastic and (ii) elastoplastic rheology. Both temperature distributions and ground deformation are firstly evaluated by solving an axi-symmetric problem to estimate the effects of thermo-mechanical response of the medium. The thermo-mechanical model permits to evidence that anelastic relaxation is responsible for significant time-dependent variations in long-term deformation. These effects may be relevant for the interpretation and quantitative assessments of the pressure changes within magmatic sources.

With this in mind, we reviewed the ground deformation observed on Etna volcano during the 1993–1997 inflation period by

setting up fully 3D temperature-dependent anelastic models. The real topography of volcanic edifice and the crustal heterogeneities inferred from the seismic tomography data were included in the 3D model. We evaluated the effects of conductive thermal propagation on long-term deformation in terms of viscoelastic response of the medium.

5.2.1.1 Viscoelastic versus elastic rheology: the enhancement in ground deformation.

Some studies on the deformation of a viscoelastic Earth were developed since 1970's, and very slow crustal deformations with the duration time of several days to a few years were investigated (Peltier, 1974). The multi-layer Earth model was rather difficult to deal with analytically, however a simpler case study was anticipated in order to describe the behavior of a viscoelastic half-space. Bonafede et al. (1986) presented the crustal deformation due to the Mogi model in a viscoelastic half-space and worked out analytical solutions for the displacements and associated stress fields induced by a pressure point source. Dragoni and Magnanensi (1989) computed an analytical model considering a spherical magma chamber in an infinite space and surrounded by a homogeneous shell of thermal metamorphic rocks, which is elastic dilatational and Maxwell deviatoric. Recently, Piombo et al. (2007) computed the viscoelastic effect on displacement, displacement gradient and stress fields due to shear and tensile dislocations. Investigations were also conducted using numerical methods, highlighting that rheological heterogeneities may be much more important than elastic heterogeneities in the

interpretation of long-term deformation (Folch et al., 2000; Trasatti et al., 2003; Fernández et al., 1996b, 2001).

In the present study, we starting considering an axi-symmetric model. In such a case a simpler two-dimensional domain can be considered by exploiting the symmetries. Hence, the number of nodes, in which the solution is computed, decreases significantly. The FEM model is made up of ~16,000 triangular elements of variable size, in axi-symmetric configuration. The domain extends 25 km horizontally from the source centre and 75 km below the surface (Figure 5.21), and well reproduces the conditions generally imposed to half-space models (vanishing stresses at infinity). We choose a fractional shear moduli of $\mu_0 = \mu_1 = 0.5$ and a viscosity of $\eta = 2 \times 10^{16} Pas$. An overpressure of 100 MPa was applied on the source wall.

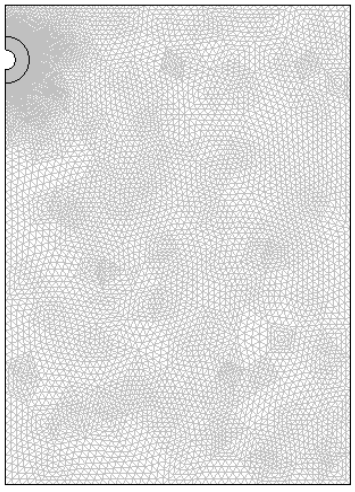

Figure 5.21. The FEM mesh for the axi-symmetric model incorporating the spherical magma chamber.

Simulations last for about 9 days: we report the vertical displacements but similar results are achieved for horizontal displacements. The viscoelastic solution at t = 0 coincides with the elastic solution. Subsequently, the deformation grows exponentially approaching a finite value (Figure 5.22).

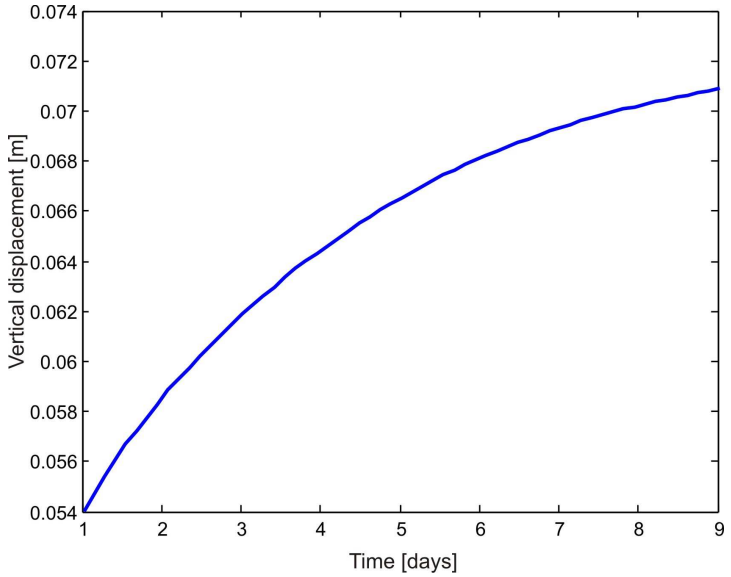

Figure 5.22. Temporal evolution of the vertical uplift due to a spherical pressure source in a homogenous and viscoelastic half-space.

The ground deformation of the viscoelastic model is enhanced with respect the elastic solution. Particularly, the ratio between the steady-state viscoelastic solution and the elastic one is about 1.7. Therefore, the inclusion of a viscoelastic rheology significantly lowers the pressure changes, necessary to obtain the same amount of ground deformation, from 100 MPa to 58.9 MPa. To estimate the increase in

ground deformation with respect to the elastic solution, we computed the relative misfit for the vertical displacement as

$$E_{\%} = \frac{\sum \left| U_{viscoelastic} - U_{elastic} \right|}{\sum \left| U_{elastic} \right|} \times 100 \qquad (5.1)$$

The steady-state viscoelastic solution yields a misfit E% of 71%.

The assumption of a homogeneous viscoelastic half-space is too restrictive and limits the application of the model to more realistic case study. In fact, the upper lithosphere does not participate in viscoelastic flow due to its lower temperature. To overcome this limitation, we explore a viscoelastic shell model in which the spherical source is embedded in an elastic half-space and surrounded by a concentric shell of viscoelastic material. It is reasonable to assume that rocks near the inflation source are considerably heated and weakened beyond the brittle-ductile transition temperature, where viscoelastic rheology is more appropriate to describe the mechanical behaviour of the surrounding rocks. We supposed a viscoelastic behaviour inside the shell, while an elastic behaviour outside it. We firstly choose a homogeneous viscoelastic shell with radius 1.7 km. The viscoelastic medium parameters within the shell are the same as in the homogeneous half-space model. As we can notice from Figure 5.23, after the introduction of the viscoelastic shell the surface uplift is less enhanced with respect to the previous model when the entire half-space medium is assumed viscoelastic. The relative misfit E% is decreased to 54%. The amplitude of the viscoelastic response is dependent on the size of the shell (Dragoni and Magnanensi, 1989):

wider the shell, higher the deformation observed at the ground surface. Both the thickness and the viscosity of the shell are strongly influenced by the temperature state of the volcanic source.

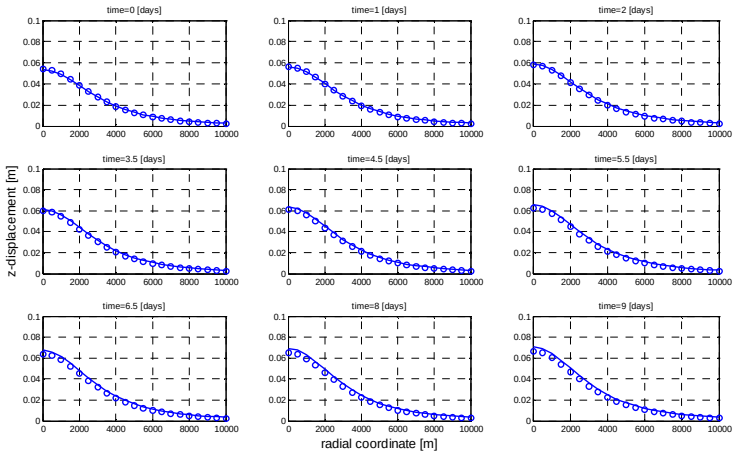

Figure 5.23. Ground uplift due to a spherical pressure source embedded in a viscoelastic half-space (solid line) and in an elastic half-space and surrounded by a viscoelastic shell (circles).

5.2.1.2 Effects of thermo-viscoelastic response

The spatial dependence of viscosity on temperature can be included in the model solving a thermal model to compute the temperature field distribution. Therefore, we conducted a thermo-mechanical model in which the viscoleastic properties of the medium are derived from the computed temperature distribution. We simulated the model in two steps solving separately: (i) the heat conduction

equation to compute the temperature profile, and (ii) the viscoelastic problem to obtain the numerical solution of the deformation field.
To derive the temperature profile, we numerically solved the heat conduction equations in an axial-symmetric formulation, given by

$$\nabla(k\nabla T) = q \tag{5.2}$$

where $T = T(r, z)$ is the temperature field, r is the radial coordinate, z is the vertical coordinate, k is thermal conductivity, and $A(z) = A_s \exp(-z/b)$ is the crustal volumetric heat production, where A_s is the volumetric rate of heat production, and b is a characteristic depth of the order of 105 km. Since the deformation timescales are much shorter than those over which the magma chamber evolution takes place, the temperature distribution, and therefore the viscosity profile inside the shell, can be considered as steady. As boundary condition at the ground surface, we assumed that the surface is kept constant at atmospheric temperature, since the thermal conductivity of the air is much smaller than that of the ground. At bottom and lateral boundaries we assigned the geothermal temperature values, because they are far enough to not be affected by the magmatic source. We used the steady-state geothermal profile given by (Ranalli, 1995; Turcotte and Schubert, 1982):

$$T(z) = T_s + \left(\frac{q_m z}{k}\right) + \left(\frac{A_s b^2}{k}\right)\left(1 - e^{-z/b}\right) \tag{5.3}$$

where T_s is the surface temperature, q_m is the heat flow coming from the mantle. The temperature on the magma wall was set to T_0=1000 K. Physically, this boundary condition is equivalent to stating that the magma walls act as heat sources, simulating a continuous refilling of the magma chamber (Dragoni et al., 1997; Civetta et al., 2004).
Starting from the temperature distribution, a variety of empirical relationships can be used to infer the temperature-viscosity dependence. We estimated the medium viscosity surrounding the source region using the Arrhenius formula:

$$\eta = A_D exp\left(\frac{E}{RT}\right) \tag{5.4}$$

where A_D is the Dorn parameter, E is the activation energy, R is the Boltzmann constant, and T the absolute temperature. Additional work is needed to define plausible values for the rheological parameters, and determine the extent to which these parameters vary in the region of high thermal gradients near the magma chamber. The values of the parameters used in the computations are summarized in Table 5.2. The viscosity inside the shell depends on the temperature distribution. However, the thickness of the shell was kept constant at 1.7 km.

Table 5.2. Thermal and mechanical parameters.

	Thermal parameters	
Ts	Surface temperature	273 K
qm	Heat flow	0.03 mWm-2
k	Thermal conductivity	4 Wm-1K-1
As	Volumetric rate of heat production	2.47 10-6 Wm-3
b	Length scale for crustal radioactive decay	14.170 km
	Mechanical parameters	
AD	Dorn parameter	109 Pas
E	Activation energy	120 kJ/(mol)
R	Boltzmann constant	8.314 J/(mol K)

Several simulations were also conducted to investigate how the temperature of the magmatic source affects the ground uplift. Different values of temperature in the range 1000-1500 K were used. The steady-state temperature profiles using T=1000 K and T=1500 K at the source wall are shown in Figure 5.24 together with the estimated medium viscosity from Equation (5.4). The viscosity within the viscoelastic shell is ranging from 10^{15} Pas to 10^{20} Pa s for T = 1000 K, and from 10^{13} Pa s to 10^{17} Pa s for T=1500 K.

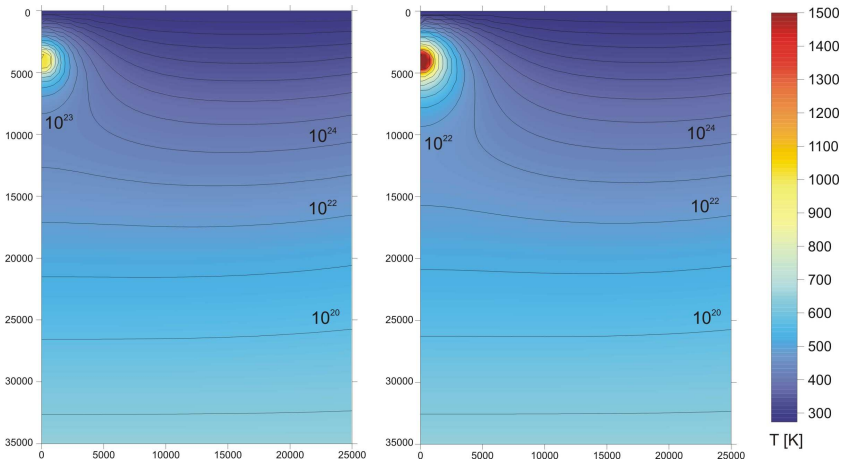

Figure 5.24. Temperature (colour scale) and viscosity (contour lines in Pa s) profiles for source wall temperature at T = 1000K (on the left) and T = 1500K (on the right).

The amplitude of the deformation after 120 days is dependent on the temperature profile (Figure 5.25). The vertical uplift at the ground surface above the source centre varies from 6.9 cm at 1000 K to 7.9 cm at 1500 K with a relative misfit E% of 29% and 47%, respectively (Figure 5.26). However, the increase is not linearly proportional, but a saturation effect is observed for higher temperatures. This could be ascribed to the fixed dimension of the shell and to the exponential dependency of the viscosity on the temperature. It is reasonable to assume that the thickness of the viscoelastic shell increases with the temperature.

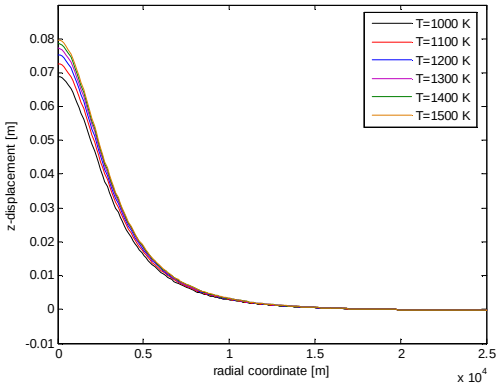

Figure 5.25. Vertical uplift at 120 days after the pressure increase within a magma source embedded in an elastic medium and surrounded by a viscoelastic spherical shell. Different thermal regimes are considered.

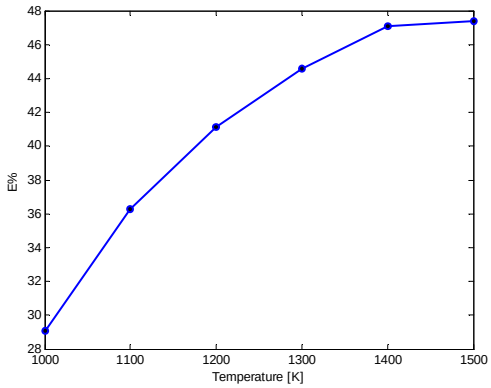

Figure 5.26. Misfit on the vertical uplift between the elastic solution and the viscoelastic response at 120 days after the pressure step-like increase. The uplift increases with the temperature on the source wall.

The viscoelastic behaviour is appropriate around the magmatic source where the temperature is higher. Instead of using a constant thickness for the viscoelastic spherical shell, we modified the properties of the medium through the constitutive equations, allowing the element of the domain to behave elastically or viscoelastically in function of the temperature distribution. We associated to the medium elastic proprieties where the temperature values are below a fixed threshold and viscoelastic proprieties above this threshold. The solutions vary as a function of the threshold. We made a comparison between this model in which the thickness of the shell is temperature-dependent and the model in which all the medium is fully viscoelastic. We observed that these results does not differ too much using temperature threshold lower than 700 K (Figure 5.27). Far away from the source, the temperature decays, yielding a higher value of viscosity which makes the medium to behave as elastically (Williams and Richardson, 1991). As before, the deformation raises with temperature (Figure 5.28), but no saturation phenomena are observed (Figure 5.29). The vertical uplift at the ground surface above the source centre reaches, after 120 days, a deformation of 7.4 cm at 1000 K (E% = 38%) and 8.8 cm at 1500 K (E% = 59%). It is worth to note that in this case the deformation is enhanced with respect to the case in which the viscoelastic behaviour is restricted to a fixed shell around the source.

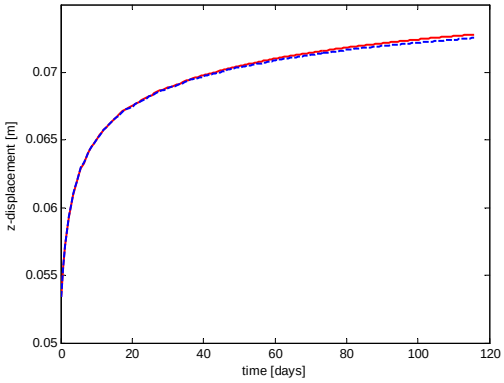

Figure 5.27. Comparison between the model in which the thickness of the shell is temperature-dependent (blue dashed line) and the model in which all the medium is fully viscoelastic (red solid line).

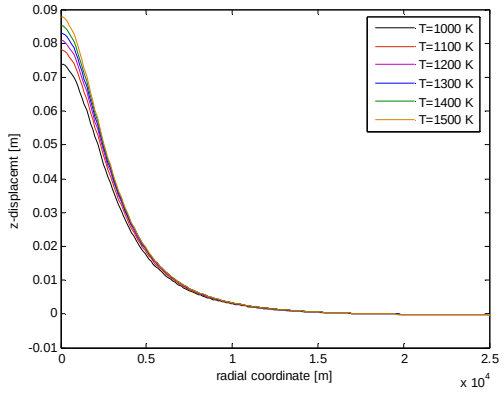

Figure 5.28. Vertical uplift at 120 days after the pressure increase within a magma source embedded in a temperature-dependent. viscoelastic half-space. The temperature on the source wall is varied from 1000K to 1500K.

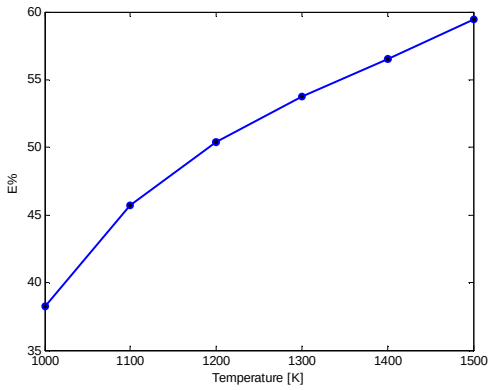

Figure 5.29. Misfit on the vertical uplift between the elastic solution and the viscoelastic solution at 120 days after the pressure increases. The viscoelastic response is strongly dependent on the temperature along the source wall.

The temporal evolutions of the vertical uplift with source wall temperature at T = 1000K and T = 1500 K are shown in Figure 5.30. As the temperature increases, the viscoelasticity decreases yielding lower relaxation times and the ground deformation raises faster. Even when the viscoelastic shell thickness is fixed (Figure 5.30a), the temperature profile affects the amount of deformation reached after the exponential increase. When the rheological behaviour of the whole surrounding medium is temperature-dependent (Figure 5.30b), the region, which behaves viscoelastically, becomes wider as the temperature increases and gives more contribution to the viscoelastic part of the deformation field.

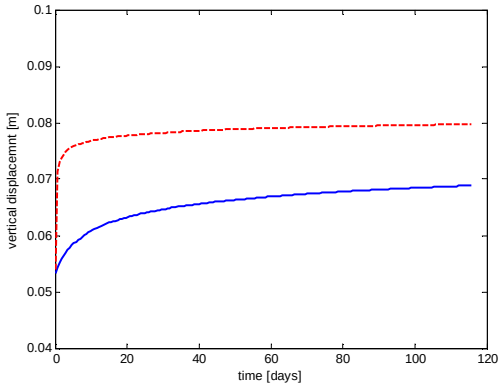

(a)

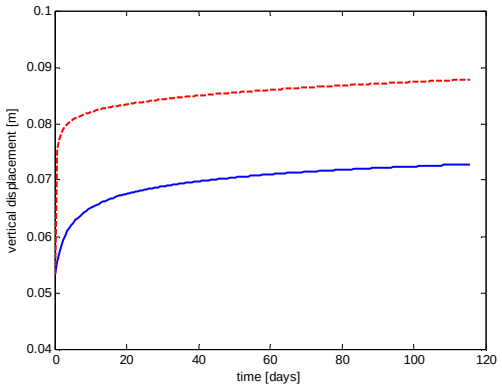

(b)

Figure 5.30. Ground uplift at $r = 0$ as function of time. (a) The pressure source is surrounded by a viscoelastic spherical shell and the wall temperature is $T = 1000$ K (blue solid line) and $T = 1500$ K (red dashed line). (b) The pressure source is embedded in a temperature-dependent viscoelastic half-space and the wall temperature is $T = 1000$ K (blue solid line) and to $T = 1500$ K (red dashed line).

5.2.1.3 Temperature-dependent elastoplastic numerical model

We explored an elastoplastic model in which the magmatic source is embedded in an elastic medium and surrounded by a shell of elastoplastic material. It is reasonable to assume that rocks near the magma source are considerably heated and weakened beyond the brittle-ductile transition temperature, where elastoplastic rheology is more appropriate to describe the mechanical behavior of the surrounding rocks. We supposed an elastic behavior inside the shell, while an elastoplastic behavior outside it. The elastic medium parameters were inferred from seismic tomography studies (Chiarabba et al., 2000; Patanè et al., 2006). The Young modulus varies from 11.5 GPa to 133 GPa, while the Poisson ratio is in the range 0.12-0.32 (Currenti et al., 2007; 2008; Del Negro et al., 2009). Among the several rheological laws that can be used to model plastic effects, the ideal plasticity obeying von Mises' criterion is adopted for the elastoplastic shell. This criterion assumes that isotropic deformation is always related elastically to the mean pressure, while the deviatoric strain is elastically related to deviatoric stress up to a threshold condition, above which plastic strain takes place at constant deviatoric stress.

We assume that the thickness of the elastoplastic shell is dependent on the temperature state of the magmatic source. This dependency is included in the model solving a thermal model to compute the temperature field distribution. Starting from the temperature distribution, we modified the properties of the medium through the constitutive equations, allowing the element of the domain to behave elastically or plastically in function of the temperature

distribution. We associated to the medium elastic proprieties where the temperature values are below a fixed threshold and elastoplastic proprieties above this threshold. To derive the temperature profile, we numerically solved the heat conduction equations (Equation 5.2). Since the deformation timescales are much shorter than those over which the magma chamber evolution takes place, the temperature distribution, and hence the elastoplastic volume, can be considered as steady. As boundary condition at the ground surface, we assumed that the surface is kept constant at atmospheric temperature, since the thermal conductivity of the air is much smaller than that of the ground. At bottom and lateral boundaries we assigned the geothermal temperature values, because they are far enough to not be affected by the magmatic source. We used the steady-state geothermal profile given by Equation (5.3).

Figure 5.31 shows the ground uplift setting the threshold from 600 K to 1000 K. In the elastoplastic model the transition temperature is found to be a very sensitive parameter. Indeed, as the threshold temperature decreases, the volume participating to the elastoplastic flow increases and gives more contribution to the plastic deformation. A 100 K of variation in the transition temperature is sufficient to enhance the ground uplift from 0.18 m to 0.25 m.

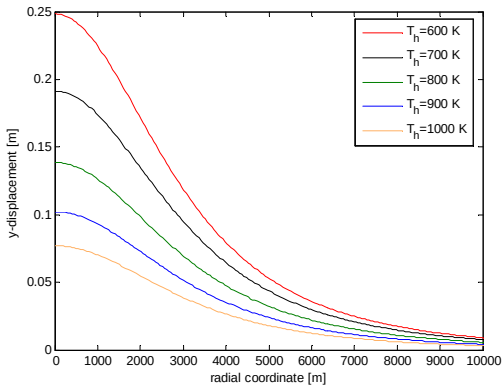

Figure 5.31: Ground uplift for the elastoplastic model as the threshold temperature increases from 600 K to 1000 K.

5.2.1.4 Comparison between elastic and anelastic strain.

We developed a 3D axi-symmetric model using FEM in order to assess the effect of rheology on the surface deformation field. In such a case a simpler two-dimensional domain can be considered by exploiting the symmetries. The source has a spherical geometry with a radius of 0.5 km and is centered at 4 km depth. The axi-symmetric model is composed of ~200,000 triangular elements, covering a rectangular half-space that extends 50 km horizontally from the source centre and 50 km below the ground surface (Figure 5.32).

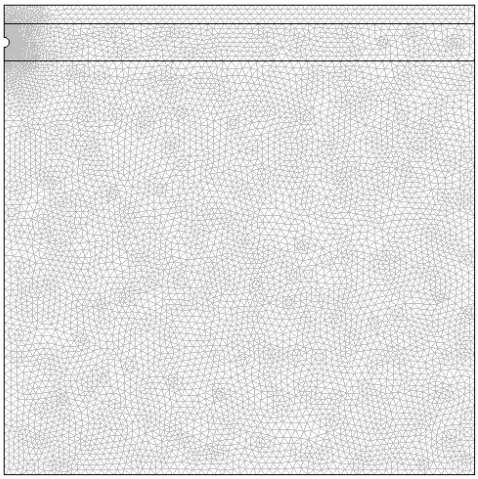

Figure 5.32. The FEM mesh for the layered axi-symmetric model.

For boundary conditions, the displacements on the outermost lateral boundaries and on the bottom are fixed to zero, while the boundary at the ground surface is stress-free. We compared the deformation field considering four different cases: (i) elastic, (ii) temperature-dependent elastic (iii) viscoelastic and (iv) elastoplastic rheology.

The first model is a three-layered elastic half-space with Poisson ratio $\upsilon = 0.25$. A very soft layer with a Young's modulus of 2 GPa is assumed for the upper part extending from the ground surface to 2 km. A Young's modulus of 40 GPa is assumed for the second layer from 2 km to 6 km b.s.l., whereas a Young's modulus of 80 GPa is used for the third layer from 6 km to 50 km b.s.l.. The other models were constructed introducing in the layered half-space a shell surrounding the magmatic source. The thickness of the shell is dependent on the temperature state of the magmatic source. The

temperature field distribution is computed solving the thermal model with values of the model parameters reported in Table 5.2. The temperature on the magma chamber wall is set to T_w=1200 K. Laboratory experiments of mechanical strength on basaltic rocks have shown that the elastic modulus decreases steadily with temperature and ductility is expected above 900 K at a differential stress of about 10-15 MPa (Rocchi et al., 2004; Dingwell, 1998). Etnean rocks remain fully brittle up 900 K, and above this temperature the elastic modulus decreases reaching 10% of the original value (Rocchi et al., 2004). Therefore, in the second model the rigidity modulus varies linearly with the temperature (18 MPa/K) besides 900 K, and is kept at 10% of the initial values above 1100 K. In the third and fourth model an anelastic behavior was supposed in the shell surrounding the source, while the remaining domain was set as elastic. Particularly, in the third model the anelastic behaviour was supposed as viscoelastic, in the fourth model was supposed elastoplastic. For these models, starting from the temperature distribution, we modified the properties of the medium through the constitutive equations, allowing the element of the computational domain to behave elastically or anelastically in function of the temperature distribution. We associated different rheologies to the medium: (i) elastic behavior where the temperature values are below 900 K, and (ii) anelastic behavior above this threshold.

The third model implement a linear viscoelastic material, where stress linearly depends on the strain and its time derivatives. We choose a fractional shear moduli of $\mu_0 = \mu_1 = 0.5$ and a viscosity of $\eta = 2 \times 10^{16} Pas$. In the fourth model we implemented the yield

stress/strain laws considering an ideal plastic behavior obeying to von Mises criterion; the yield strength of surrounding rocks is assumed as $\sigma_y = 15MPa$. In both models the elastic parameters of the medium are those of first model previously described.

An overpressure of 100 MPa was applied on the source wall. Model results are shown in Figure 5.33. The layered elastic model gives a vertical uplift above the source center of about 7.5 cm. When the elastic modulus is decreased with temperature, an enhancement to 9.0 cm is obtained. In the viscoelastic solution the deformation are greater of about 1.3 in comparison with the elastic solution while, the elastoplastic model considerably enhances the ground uplift up to a 14.5 cm, which is about double than that obtained for the heterogeneous elastic model. These results show that the presence of a plastic region can greatly amplify the strain response.

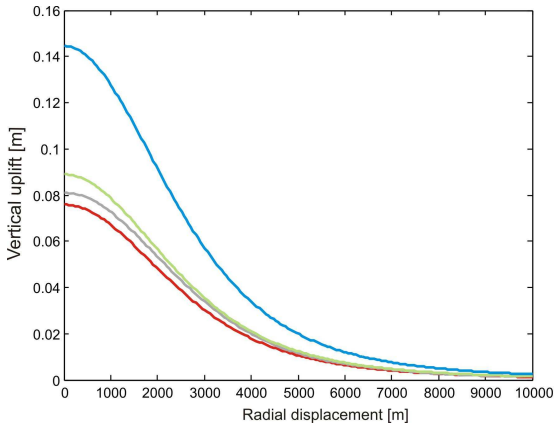

Figure 5.33. Comparison of the deformation expected from a same pressurizing (100 MPa) chamber centered at a 4 km depth in a layered medium considering elastic (red line), elastic with varying temperature (gray line), viscoelstic (green line) and elastoplastic (blue line) rheologies.

5.2.1.5 The application on Mt. Etna

Most interpretations of the deformation on Mt Etna from 1994 to 2004 (Table 5.3) were based on a homogeneous elastic half-space model. Under the assumption of elastic rheology, the amplitude of the deformation field for a spheroidal pressure source is linearly related to the intensity factor $V\Delta P / \mu$ (V =volume, ΔP =pressure change, μ =rigidity modulus). Hence, the effect of changes in pressure and in volume of a spheroidal source on the ground deformation cannot be separated from the estimate of rheology parameters. Because of the strict link between crustal rigidity, source pressure and deformation, a lack of insight into the rheology contributes to increase the uncertainty on source volumes and associated pressures (Newman et al., 2001; Bonaccorso et al., 2005). Differences between the static elastic modulus and the dynamic elastic modulus deduced from seismic velocities can furthermore alter these estimates (Ciccotti and Mulargia, 2004; Cheng and Johnston, 1981). Therefore, the correct estimate of the magmatic source pressure from the ground deformation is still an open issue.

Table 5.3. Pressure sources from geodetic data inversion at Mt Etna (after Bonforte et al., 2008). All models are based on analytical solutions except Bonaccorso et al. (2005), who used also a numerical solution.

Period	Source	Lat [UTM km]	Long[UTM km]	Depth [km]	ΔP*V [N*m]	Rigidity [GPa]	Reference	Data
Sept 1993 – Jul 1994	Mogi	4179	500	3.8	2.19×10^{17}	not reported	Puglisi et al. (2001)	GPS
Jun 1993 – Oct 1995	Yang	4177.67	499.89	4.8	2.74×10^{17}	30	Lundgren et al. (2003)	InSAR
Jul 1996 – Jul 1997	Mogi	4180.9	497.61	9.3	13.69×10^{17}	not reported	Puglisi and Bonforte (2004)	GPS
Sept 1993 – Jul 1997	Mogi	4179.45	496.96	6.8	17.24×10^{17}	30	Palano et al. (2007)	GPS
Sept 1993 – Jul 1997	Davis	4177.96	500.7	4	9.6×10^{17}	heterogeneous	Bonaccorso et al. (2005)	EDM,GPS
Sept 1994 – Sept 1998	Mogi	4181	500	5	2.32×10^{17}	10	Obrizzo et al. (2004)	levelling
Sept 1993 – Jul 2000	Mogi	4181.37	496.93	8.1	28.84×10^{17}	30	Palano et al. (2007)	GPS
Jul 1994 – Jul 2001	Mogi	4180.5	499	6.2	33.4×10^{17}	not reported	Houlie´ et al. (2006)	GPS

Despite the different geodetic data, the methodologies used and the results achieved, the intensity factors $V\Delta P / \mu$ are similar for most of the models (Table 5.3), but it is not possible to determine them unambiguously because of the trade-off between the volume and overpressure of the source. Assuming a homogeneous half-space with an elastic shear modulus of 30 GPa, Lundgren et al. (2003) used SAR images for estimating a pressure of about 5 MPa for a spheroidal source with a volume of $68.69 \cdot 10^9$ m^3, which is definitely too high as it has never been revealed by the seismic investigations. Bonaccorso et al. (2005) interpreted the 1993-1997 GPS and EDM data using an analytical model of a ellipsoidal source with a volume of $3 \cdot 10^9$ m^3, an overpressure of 20 MPa and a low homogeneous shear modulus of 1 GPa. They also evaluated the effects of topography and medium heterogeneity on the deformation field using a numerical simulation employing an elastic model. Since the average values of the dynamic shear modulus used in the simulation, which had been estimated from seismic velocity measurements, were larger than those used in the homogeneous analytical model, the observed displacements in the

heterogeneous models were reproduced by increasing the overpressure up to about 320 MPa. The source inferred by the simpler analytical model is equivalent to a lower pressurized magma chamber surrounded by a lower rigidity, which can be considered as a sort of "effective" rigidity calling for the needs of using an anelastic rheology (Bonaccorso et al., 2005).

In the previous sections, we observed how the inclusion of a realistic anelastic component could significantly lower the inferred pressure necessary to explain the observed surface deformation (Newman et al., 2006). With this in mind, we developed a fully 3D model analyzing the ground deformation accompanying the 1993-1997 inflation period on Mt Etna assuming a heating pressurized magma chamber embedded in an anelastic heterogeneous medium.

We adopt the same ellipsoidal source determined by Bonaccorso et al. (2005),which is located 4.2 km b.s.l. beneath the central craters (latitude 4177.9 UTM km and longitude 500.7 UTM km). The ellipsoid has a semi-major axis of 1854 m and the other two semi-axes of 725 m and 544 m, respectively with an orientation angle of 124◦ and a dip angle of 77◦ (Figure 5.34).

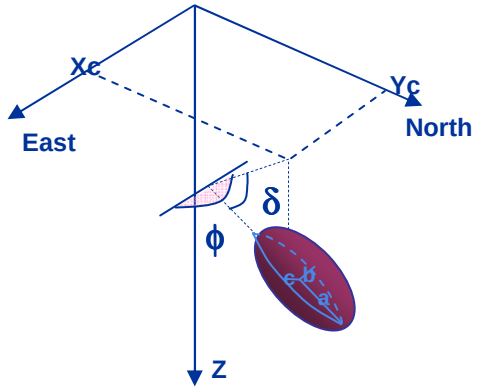

Figure 5.34. Ellipsoidal source (from Bonaccorso et al., 2005).

In the numerical model we also included the rheological heterogeneities of the medium. We used P-wave and S-wave seismic velocities, inferred from recent seismic tomography studies (Chiarabba et al., 2000; Patanè et al., 2006), to derive the elastic medium parameters. The computational domain was set up to a large volume extending 100 km × 100 km × 100 km in order to avoid artifacts in the numerical solution because of the proximity of the boundary. The mesh of the ground surface was generated using a digital elevation model of Etna volcano from the 90m Shuttle Radar Topography Mission (SRTM) data. The computational domain was represented by number of 20,000 arbitrarily distorted tetrahedral elements connected by 4000 nodes. The mesh resolution is about 100 m around the ellipsoidal source, about 300 m in the area surrounding the volcano edifice, and decreases to 2 km in the far field (Figure 5.35).

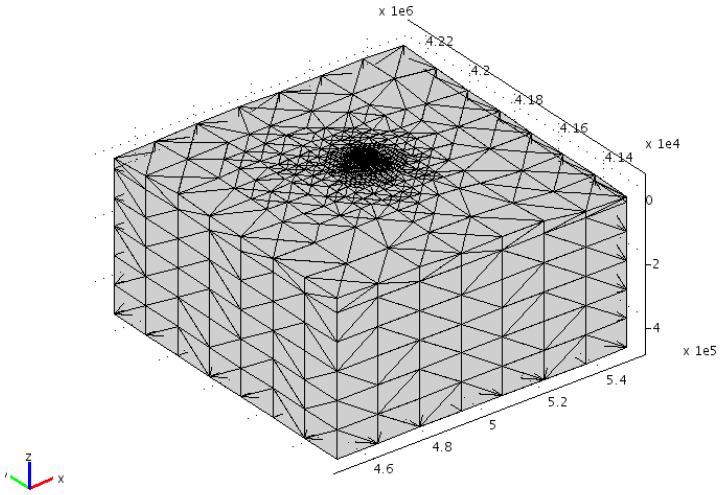

Figure 5.35. The FEM mesh for the fully 3D model.

Firstly, we solved the conductive heat transfer equation. The temperature field distribution (Figure 5.36) is computed solving the thermal model with values of the model parameters reported in Table 5.2. The temperature on the magma chamber wall is set to T_w=1200 K.

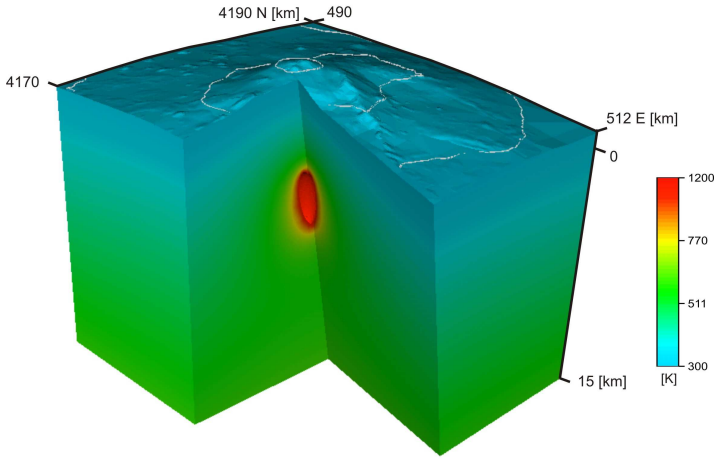

Figure 5.36. Temperature field distribution assuming a source wall temperature of T_w=1200 K.

Two simulations were carried out. In the first one we assumed a thermo-viscoelastic rheology, in the second one we assumed a temperature-dependent elastoplastic medium.

Regarding the viscoelastic model (see table 5.2 for parameters), two different simulations were carried out. In the first one we assumed a step-like pressure change of 320 MPa, in the second one we assumed a linear pressure increase in order to simulate the continuous inflation phase of the pressurized magmatic source. The pressure source evolves like a ramp function from 0 MPa to 320 MPa during 1993–1997 with a increment of 90 MPa/year. Even if the temporal evolution is very different, the final uplift is quite similar. Figure 5.37 shown the viscoelastic response after 3 years and half applying a step-like pressure change.

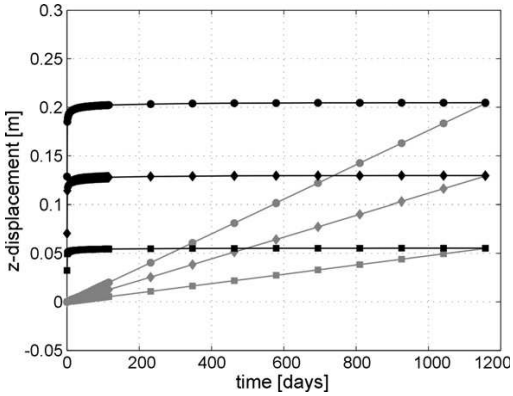

Figure 5.37. Vertical uplift at OBS (circle), ESLN (square) and TDF (diamond) computed for a step-like pressure increase (black lines) and linear pressure change (grey lines).

Therefore, a comparison with the temporal evolution of real data could allow for distinguishing between them. In Bonaccorso et al. (2005), no temporal evolution of ground deformation data was shown. However, a cumulative planar areal dilatation was computed for the Etna networks. Since a fairly continuous expansion seems to affect the volcanic edifice starting from 1993 to 1997, we can better consider a continuous linear feeding rate of the pressure source. The relative misfit with respect to the elastic solution at the ground surface is 55% for a wall temperature of T = 1000K and 66% for T = 1500K. Both the horizontal and vertical deformation in the viscoelastic solution are enhanced of about 1.6 in comparison with the elastic solution (Figure 5.38). Therefore, the temperature-dependent viscoelastic model requires a lower pressure changes (~200MPa) that is nearer to the lithostatic load (~170MPa), but still higher than 500 the crustal strength (~45MPa).

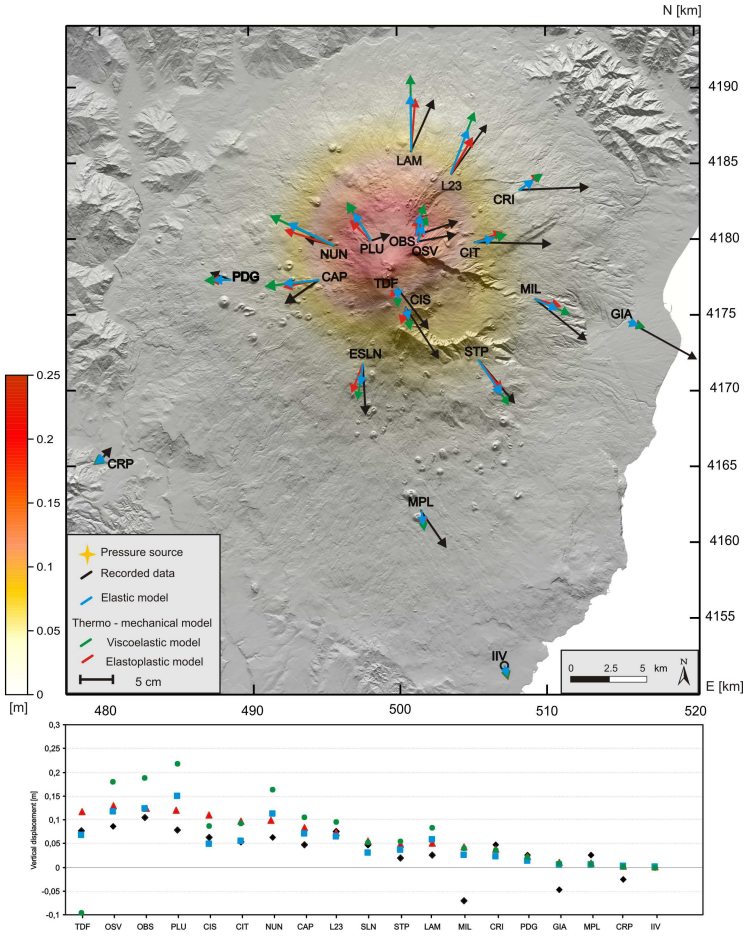

Figure 5.38. Comparison between GPS observed (black) and computed deformation during the 1993–1997 period. The numerical computations are performed assuming a heterogeneous elastic medium (blue, after Bonaccorso et al., 2005) and a temperature-dependent viscoelastic medium with pressure source of 320MP and the elastoplastic model D (blue). Horizontal displacements (top) and vertical displacements (bottom) are calculated at GPS stations. The overall pattern of the vertical uplift for the elastic model is also reported (color scale).

In the case of elastoplastic rheology, we performed eight models to investigate how the ground deformation is affected by the rheology parameters (elastic moduli, yield strength, and temperature threshold) and thermal state (source wall temperature). The elastic moduli were fixed to those inferred from seismic tomography, whereas different yield strength values were used in according to laboratory measurements on basalts from Etna (Rocchi et al., 2004; Balme et al., 2004). A vertical geothermal gradient of 22 K/km was assumed for the areas surrounding the volcano edifice in agreement with the temperature measurements carried out in deep boreholes (AGIP, 1977). The source wall temperature T_w was chosen to range between 1100-1200 K (Corsaro and Pompilio, 2004). The effect of the transition temperature T_t, which controls if the behavior of the medium is elastic or elastoplastic, was investigated in a range from 800 to 900 K where laboratory experiments showed ductile deformation failure (Rocchi et al., 2004). The parameters used in the all models are reported in Table 5.4.

Table 5.4. Elastoplastic model parameters. The misfit function are shown in Figure 5.39.

Model	σ_y [MPa]	T_w [K]	T_t [K]	χ^2	ΔP [MPa]
A	10	1100	900	1.19×10^4	95
B	15	1100	900	1.19×10^4	98
C	20	1100	900	1.19×10^4	102
D	10	1200	800	1.15×10^4	46
E	10	1200	900	1.17×10^4	69
F	10	1100	800	1.16×10^4	59
G	15	1200	800	1.16×10^4	53
H	15	1200	900	1.18×10^4	75

For each model, we performed different simulations varying the magma overpressure from 1 MPa to 120 MPa (with a step of 1 MPa) and computed the chi-square value χ^2 as:

$$\chi^2 = \frac{\sum (U_x^{obs} - U_x^{calc}) + \sum (U_y^{obs} - U_y^{calc})}{\sigma_H^2} + \frac{\sum (U_z^{obs} - U_z^{calc})}{\sigma_V^2} \qquad (5.7)$$

where U_{obs} and U_{calc} are the observed and computed displacements respectively, and σ is the standard deviation of the measurements (Bonaccorso et al., 2005). The standard deviation affecting measurements ranges between 2 and 3 mm in the horizontal components and between 5 and 6 mm in the vertical component. The χ^2 values are shown in Figure 5.39 for all the models and the pressure changes corresponding to the minimum χ^2 that best fits the geodetic data are reported in Table 5.4.

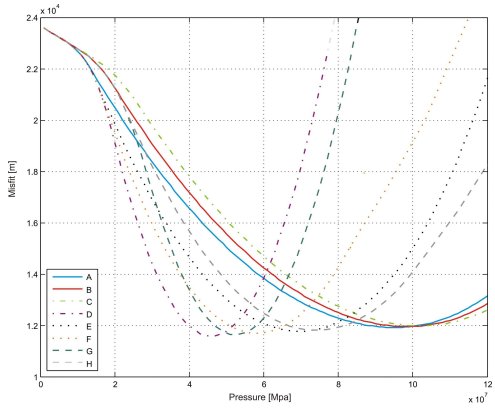

Figure 5.39. Chi-square values obtained varying the overpressure from 0 to 120 MPa for different model parameters of elastoplastic models (Table 5.3).

The pressure change estimates range between 46 MPa (model D) and 102 MPa (model C). In all the models, as the pressure increases, the deformation starts to grow linearly as far as the yield condition is not satisfied. When the elastic limit is reached, the ground deformation increases more rapidly since plastic deformation prevails. In the models with lower values of the yield strength (A, D, E, F), the medium fails plastically at lower values of the pressure change and the ground deformation is enhanced with respect to the other models (Figure 5.40).

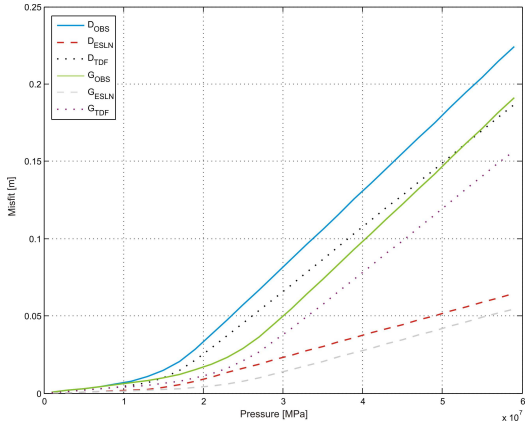

Figure 5.40. Vertical uplifts for the elastoplastic models D (gray lines) and G (black lines) at OBS (solid lines), TDF (dotted lines), ESLN (dashed lines) stations (see Figure 5.28 for the positions) for increasing source pressure.

Therefore, the pressure estimates are strongly dependent on the model parameters. The value of pressure, which gives the minimum χ^2 value, is tuned by the yield strength. The higher the yield strength, the higher the pressure required to obtain the same amount of deformation.

Besides the yield strength, another sensitive parameter is the transition temperature. As the threshold temperature decreases, the volume participating to the elastoplastic flow increases and gives more contribution to the plastic deformation. A 100 K of variation in this parameter is sufficient to vary the estimated pressure from 46 MPa (model D) to 69 MPa (model E) when the other parameters are kept constant.

Further simulations were performed assuming a decrease in rigidity modulus with increasing temperature for the models A, B, and C. Following laboratory tests on basalt rock samples from Etna (Rocchi et al., 2004), we assumed that the elastic modulus decreases steadily at 900 K reaching 10% of the original values at 1100 K. The comparison among the different models shows that the dependence of the elastic modulus on temperature does not affect too much the simulation results (Figure 5.41). A slight difference is obtained at lower overpressure since the deformation is almost elastic. When the plastic deformation prevails on the elastic deformation, it becomes the dominant effect and the effect of variations in the elastic modulus due to temperature is negligible.

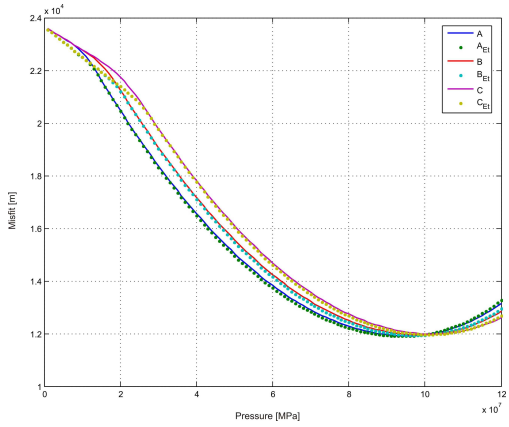

Figure 5.41. Chi-square values obtained varying the overpressure from 0 to 120 MPa for different elastoplastic models: (i) A, B, and C (continuous lines) simulations with rigidity modulus independent on temperature, (ii) A_t, B_t, C_t (dotted lines) simulations using decreasing rigidity modulus with increasing temperature.

Figure 5.38 shows deformation obtained considering Model D, with a yield strength of 15 MPa, the temperature on the source wall of T=1000 K, and the transition temperature of T=600 K. It is worth to note that this model uses a pressure change of only 46 MPa, whereas the elastic model needs an unrealistic pressure of the order of 200-300 MPa to get the same amount of deformation (Bonaccorso et al. 2009). The elastic model with a 46 MPa of pressure change would have caused ground uplifts of few centimeters, whereas the elastoplastic model reaches tens of centimeters (Figure 5.42). Interpretation of long-term deformation is complicated by the coarse spatial resolution of the available geodetic data, and the contribution of more than one mechanism to the observed ground displacements. A significant contribution to the horizontal displacements on the easternmost

stations (MIL and GIA), affected by flank instability, could be given by the effect of the sliding of the volcano eastern flank (Bonaccorso et al., 2005), which could also alter the estimate of the source parameters. It is worth to note that our numerical models disregard the stress induced by the topographic load. However, in the near-surface region, topography loading can make the stress state different from the lithostatic stress state (zero deviatoric stress), usually assumed for half-space model. Due to the topography, the medium is initially in a non-zero deviatoric stress state and the elastic limit could be even reached with a lower source overpressure.

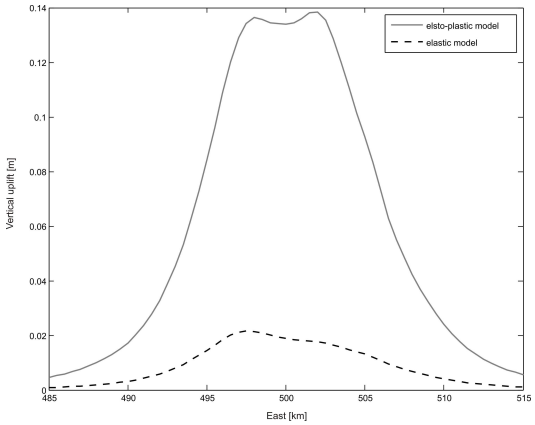

Figure 5.42. Comparison between the vertical uplift along the AB profile (Fig. 7) for the elastic (dashed line) and elastoplastic model D (solid line) using a pressure change of 46 MPa.

5.2.1.5 Discussions and conclusions

Geodetic observations are useful to discriminate among different deformation models (elastic, viscoelastic, and elastoplastic)

and may provide valuable constraints on the rheological and mechanical parameters of the medium. The elastic models usually require either overpressures of several hundreds MPa or exceedingly high source volume to justify the observed ground deformation. High overpressure values are unrealistic because the induced stresses would be such high that rocks would fracture because of the low tensile strength of common solid rocks (Balme et al, 2004; Haimson and Rummel 1982; Schultz 1995).

The viscoelastic model enables to produce deformation comparable with those obtained from elastic model, requiring a significantly lower pressure. Nevertheless, the pressure change is still high: the viscoelastic model requires a pressure increase of about 200 MPa that is near to the lithostatic load but still higher to crustal strength.

Finally, we showed that the overpressure can be lowered to geologically satisfying values if elastoplastic behavior is taken into account. The high overpressure foreseen by the elastic models is not compatible with the low levels of both volcanic activity and seismicity occurred in the analyzed period (Patanè et al. 2003). Although the summit craters were continuously degassing between March 1993 and July 1995, no fresh magma reached the surface (Allard et al., 2006). Afterwards, a series of paroxysmal eruptions occurred at the summit craters (Bocca Nuova and North-East craters), whereas South-East crater became active in the autumn of 1996 after 5 years of repose. This volcanic activity was very modest and only in the middle of 1998 significantly resumed with a series of lava fountaining from the summit craters (Allard et al., 2006) (Figure 5.43).

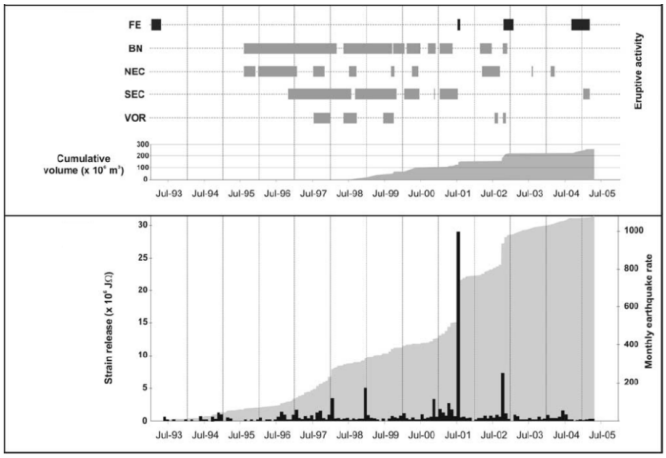

Figure 5.43. Eruptive activity and strain release during the long-lasting inflation phase from 1993 to 1997, from Bonforte et al., 2008.

A shallow broad region of low Qp hot fluids has been recognized on the west of the high rigidity body beneath the South-East flank of Etna volcano (Arevalo et al., 2005; De Gori et al., 2005; Patanè et al., 2006) (Figure 5.44), which is in agreement with the location of the estimated ellipsoidal source inferred by Bonaccorso et al. (2005), and used inside the elastoplastic rheology in this work (Figure 5.45).

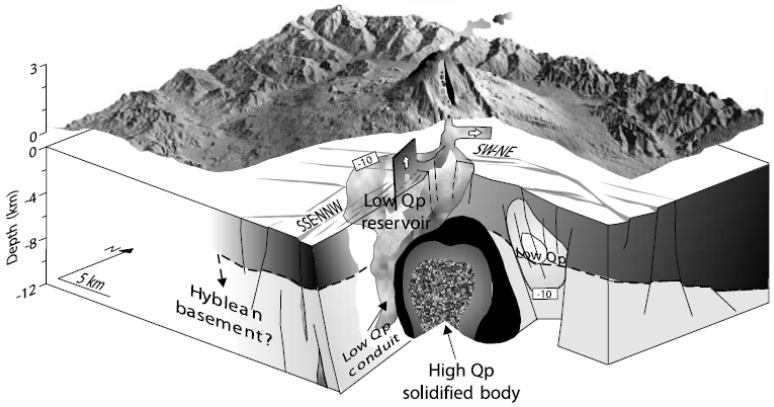

Figure 5.44. Sketch of the Mount Etna plumbing system from Q_p and V_p anomalies, from De gori et al. 2005.

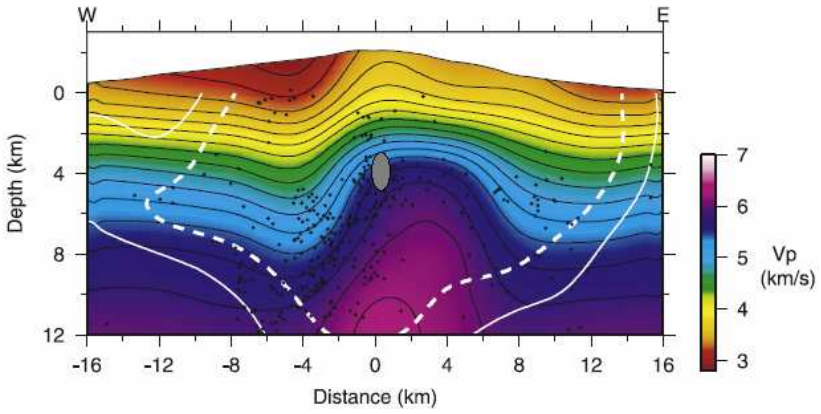

Figure 5.45. Estimated ellipsoidal source inferred by Bonaccorso et al. (2005). (After De gori et al. 2005).

During the last decades, this area has been a preferential pathway of magma rising and a region of intermediate magma storage (Bonforte et al., 2008), which could have perturbed the geothermal gradient and, hence, the mechanical behavior of the surrounding rocks. Recently, Bonforte et al. (2008) showed that the deformation observed during the long-lasting inflation phase was not recovered in the following eruptive phases, indicating a permanent deformation of the volcano. The deformation seems to be mainly accumulated following a non-elastic behavior (Figure 5.46).

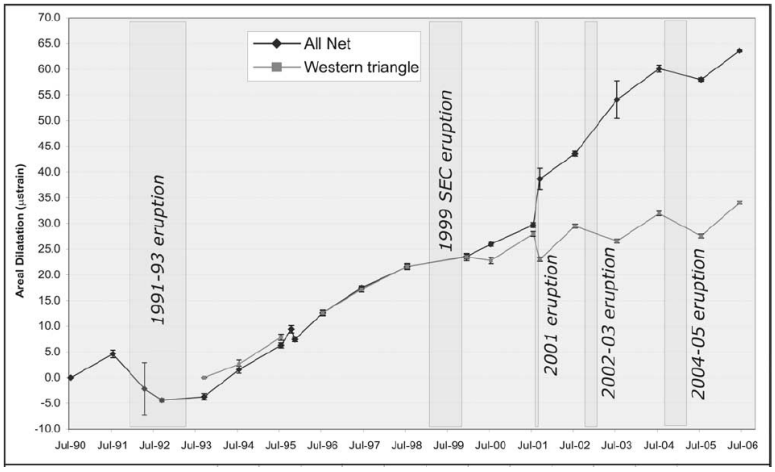

Figure 5.46. Deformation accumulated during the long-lasting inflation phase from 1992 to 2001, from Bonforte et al. 2005.

All these evidences point to the elastoplastic rheology as the more probable behavior to perform more realistic numerical simulations. Results suggest that the integration of the material rheology variations into volcano deformation modeling is a critical

and necessary advancement toward more reliable predictions and early warning systems for eruptive activity.

Chapter 6

FEM-based inversion procedure

Many analytical and numerical models have been developed to reproduce the strain-stress generated by faulting or cracking (e.g. Rybicki, 1986; Erdogan, 2000 and references therein). The elastic dislocation theory has been widely used with the simple case of a rectangular source with uniform slip in a homogeneous half-space (e.g., Okada, 1985; 1992) to model both faulting events and also intrusions in volcano areas. A main effort was also focused on calculating analytical and numerical solutions for the effects produced by dislocations embedded in a layered half-space (e.g. Sato, 1971; Sato and Matsu'ura, 1973; Sing et al., 1993; Fernandez et al., 1998; Bonafede et al., 2002, and references therein). However, different limits arise from the previous analytical and numerical models. In fact, the models in a layered medium have been mostly developed for point sources and the extended source is often modelled through a discrete distribution of point sources. Nevertheless, this procedure shows

strong singularities in the stress field of a point source and can result non-convergent and thus unsuitable in the near- field (e.g. Bonafede and Rivalta, 1999). Moreover, geometrical complexities and lateral variations of the crust layers cannot be take into account in the analytical models, and the topography, which in volcano areas can produce significant effects in the steepest surface profiles (Bonaccorso et al., 2005; Currenti et al., 2008a; Currenti et al., 2008b; Del Negro et al., 2009), is not dealt in the analytical models.

A numerical method such as the Finite Element Method can overcome these limits and help to investigate complex characteristics of the medium (e.g. Williams and Wadge, 2000; Cayol and Cornet 1998). Recently FEM has been used to examine the effect of crust layering by comparing results from different models. Irregular crust geometry, rigidity layering and lateral variations have been considered for a modeling analysis of subduction at Japan trench (Zhao et al., 2004), and heterogeneities at scale of seismic fault have been investigated (Megna et al., 2008). The results show that the effect of the crust rigidity layering and the heterogeneities' presence are significant and cannot be neglected in quantitative models of faulting or earthquakes.

The large amount of available ground deformation data recorded during the fault movements definitely highlighted that slip along a fault rupture is usually not uniform and can be better described as a distribution of different slip in the rupture source (e.g., Johnson et al., 2001; Fukahata and Wright, 2008). For considering a no-uniform fault-slip distribution the overall displacement at an observation point is given by the superposition of contributions to the displacements

(Green's Functions) from each slip on the fault. Therefore, the inverse problem yields the solution of a large-scale system of linear equations to estimate the slip distribution along the fault interfaces. The computation of the Green's functions is usually based on homogeneous or layered models, where analytical or semi-analytical solutions are available (e.g. Bürgmann et al., 1997; Wang et al., 2003). Obviously the limits in this approach are that the medium heterogeneity and topography, which are likely to affect the magnitude and pattern of the deformation field, are not considered. Nowadays denser GPS networks and above all the higher spatial resolution of DInSAR (Differential Interferometric Synthetic Aperture Radar), which provide both accurate and fine spatial characterization of ground deformation, raise the demand to use better refined models. Therefore a new binding challenge is to use numerical methods considering together a detailed medium (i.e. with local heterogeneities and real topography) and a fault/crack source with a no-uniform fault-slip distribution with the aim to invert the available deformation data.

We developed an automated procedure for high resolution geodetic data inversion to estimate not uniform slip distribution along earthquake ruptures. To account for topographic effects as well as a complicated distribution of material properties, we use the finite-element method (FEM) for computing synthetic Green's functions and estimating the static displacement. The procedure is parallelized to run on cluster for speeding up the computation time. In order to recover the slip distribution, we invert the geodetic data using a Quadratic Programming (QP) algorithm with bound constraints on slip values. A

number of tests were carried out on synthetically generated data and to assess the performance and the implication of the inversion procedure.

6.1 Application of InSAR Data for Deformation Monitoring.

InSAR data has the potential to overcome the practical limitations of poor spatial sampling by densely and accurately measuring the surface deformation field. Therefore, it is one of the preferred input to this model.

InSAR technology was originally developed for military purposes. Nowadays, it is available and widely used for a variety of civilian applications. Since the late 1980s, many applications of radar interferometry have been developed, including the observation of ground motion over agricultural areas by Gabriel et al (1989), the creation of high accuracy DEM (Zebker and Goldstein, 1986), and deformation monitoring of the Earth's crust with millimeter per year accuracy at very dense spatial sampling (Strozzi et al., 2000).

As for volcano deformation, Massonnet et al. (1995) evaluated space born radar interferometry as a highly effective method for volcano deformation detection studies. It was successfully demonstrated that radar images, acquired by ERS-1 satellite, could be applied to detect the inflation of volcanic edifices that usually precede eruptions. Further studies conducted on Mt Etna volcano also showed

the suitability of the InSAR for volcano eruption monitoring (Sansosti et al.,1998; Lanari et al, 1998).

Indeed, the researchers indicated the advantages of the InSAR over standard geodetic techniques for ground deformation monitoring either for volcanic activities or earthquake motion detection, due to the very dense spatial sampling and its high vertical accuracy.

The drawbacks instead are the horizontal resolution limited by the size of the resolution pixel (20 m in case of satellite ERS-1/2) and, while the weather conditions do not prevent a radar system from acquiring an image, the changes in weather conditions from times of image acquisition reduce the applicability of radar interferometry for deformation detection studies.

6.1.1 Differential Interferometry Method

Deformation observation using InSAR are made possible by the fact that surface motion caused by natural and human activities generates a local phase shift in the resultant interferograms.

Two SAR images are required to produce an interferogram; these may be obtained pre-processed, or produced from raw data by the user prior to InSAR processing. The two images must first be co-registered, using a correlation procedure to find the offset and difference in geometry between the two amplitude images. One SAR image is then re-sampled to match the geometry of the other, meaning each pixel represents the same ground area in both images. The interferogram is then formed by cross-multiplication of each pixel in the two images, and the interferometric phase due to the reference ellipsoid is removed, a process referred to as flattening. For

deformation applications a DEM can be used in conjunction with the baseline data to simulate the contribution of the topography to the interferometric phase, this can then be removed from the interferogram (Figure 6.1).

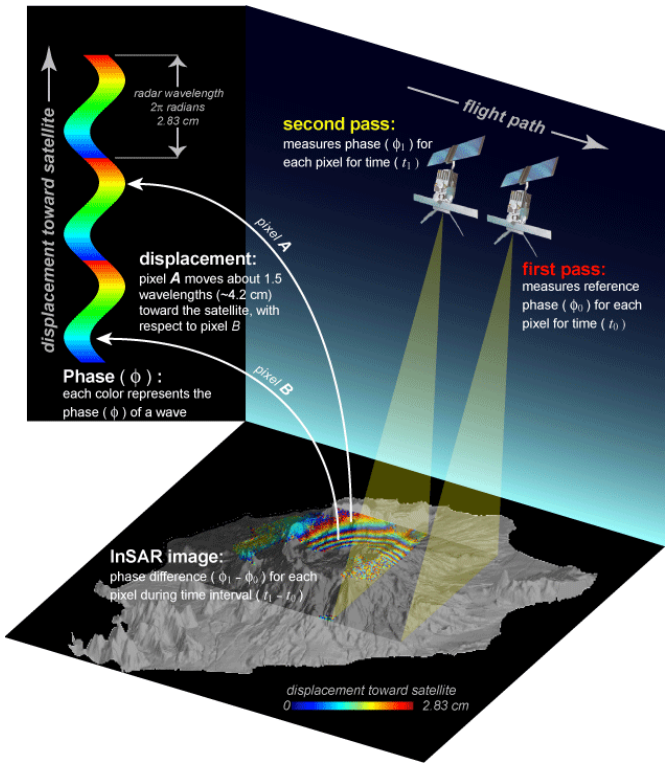

Figure 6.1. Schematic illustration of the interferometric technique.

In the interferometric mode we measure phase changes, ϕ, between radar backscatter from the Earth's surface taken at various orbits of the satellite. The phase is related to the surface displacement projected onto the line of sight to the satellite by the expression :

$$\phi = \frac{4\pi}{\lambda}(H + \Delta\rho) \tag{6.1}$$

where λ is the wavelength of the radar wave, H is the contribution from topography and $\Delta\rho$ is the change in distance to the satellite (range) that we seek. The effect of topography can be removed by using either a digital terrain model (DTM) or by using additional orbits to remove the topography term (Gabriel et al. 1989;). Removal of the topography using a DTM results in a range estimate which is accurate to 0.25–1.2 cm, for a nominal DTM error of 30 m. Using multiple satellite passes to remove topographic effects results in estimates which are accurate to a few millimeters (Zebker et al. 1995).
After the basic interferogram has been produced, it is commonly filtered using an adaptive power-spectrum filter to amplify the phase signal. For most quantitative applications the consecutive fringes present in the interferogram will then have to be unwrapped, which involves interpolating over the 0 to 2π phase jumps to produce a continuous deformation field. At some point, before or after unwrapping, incoherent areas of the image may be masked out.
Once phase unwrapping is done, the unwrapped interferogram needs to be transformed from radar coordinate system (i.e. range/azimuth) into georeferenced coordinate system (i.e. either latitude/longitude or UTM). This is the final step of InSAR processing in most case .
The deformation retrieved from the unwrapping will be referred to the satellite line of sight, according to:

$$d_{los} = [U_n \sin\phi - U_e \cos\phi]\sin\lambda + U_v \cos\lambda \tag{6.2}$$

where ϕ is the azimuth angle of the satellite heading vector (positive clockwise from the North), λ is the radar incidence angle and U_n, U_e and U_v are the displacement components respectively projected on North, East and Vertical direction.

6.2 Inversion procedure

The relationship between slip along a fault and surface displacements can generally be described by a linear relationship:

$$d_i = Gs \tag{6.3}$$

where G is the elastic response of the Earth (Green's functions), s is the fault slip and d_i are displacements observed on ground surface. Although uniform slip models can provide a fair fit to geodetic data, heterogeneous slip along the fault plane is expected. Discretizing the fault planes into M sub-faults (patches hereafter) leads to the displacement:

$$d_i = \sum_j G_{ij} s_j \tag{6.4}$$

where the G_{ij} coefficients are the contributions to the displacement at the *i*-th observation point due to a unitary dislocation of the *j*-th patch. Therefore, the inverse problem can be formulated as the solution of a system of N linear equations as:

$$\mathbf{d} = \mathbf{G}\mathbf{s} \tag{6.5}$$

where s is the M vector of unknown slip values of the patches, d is the N vector of observed ground displacements, and $\mathbf{G}$ is a matrix with elements G_{ij}. Summing up, the procedure can be subdivided into three main points (Figure 6.2):

(i) Subdividing the faults in a finite number of patches;

(ii) Computing the Green's Function for all the patches and the measurement points;

(iii) Solving a linear inversion problem to determine the slip distribution.

These points are described below in more detail.

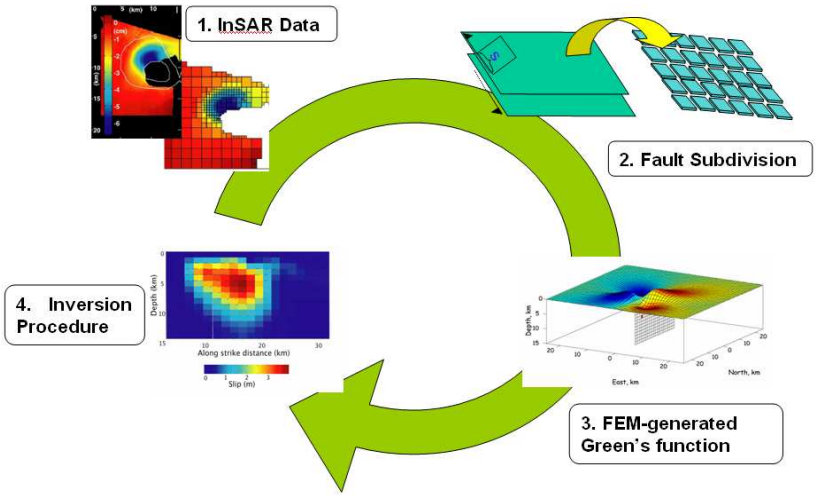

Figure 6.2. Schematic diagram of the main step in the automated procedure for InSAR data inversion.

6.2.1 Fault subdividing

The complex deformation pattern detected by geodetic measurement cannot be sufficiently explained by simple analytical models with rectangular fault geometry and constant slip along the fault. Indeed, the dislocation source parameters determined from these data suggest that slip along a fault is not uniform and is best described as a distribution of dislocation sources (Figure 6.3) (Wald and Heaton, 1994; Pritchard et al., 2002).

To deal with these issues, a discretization of the fault plane with a specified geometry and dimensions into a grid of rectangular sub-faults was implemented. The geometric parameters are fixed from the

uniform slip solutions and the goal is to solve for the optimal slip on each patch.

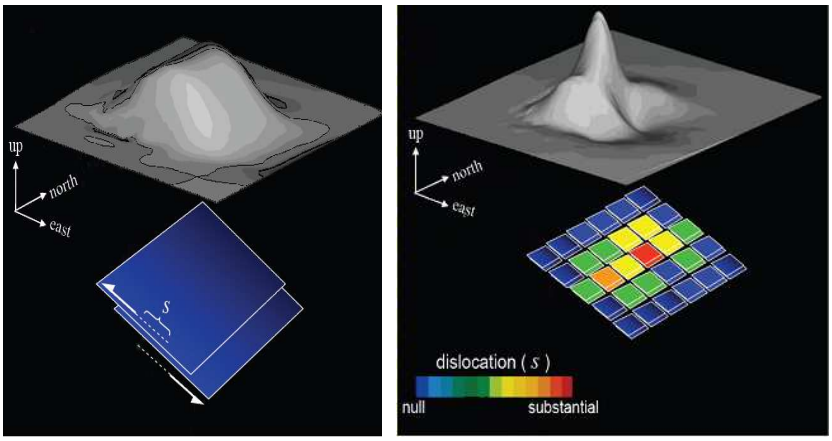

(a) (b)

Figure 6.3. (a) Constant slip on a rectangular fault and related deformation; (b) more complex deformation pattern and relative slip distribution.

6.2.2 Green's functions computing

The Green's functions are computed using the finite-element method (FEM) to account for topographic effects as well as a complicated distribution of material properties (Figure 6.4). The numerical model is conducted using PyLith, a parallel finite element code (Williams, 2006).

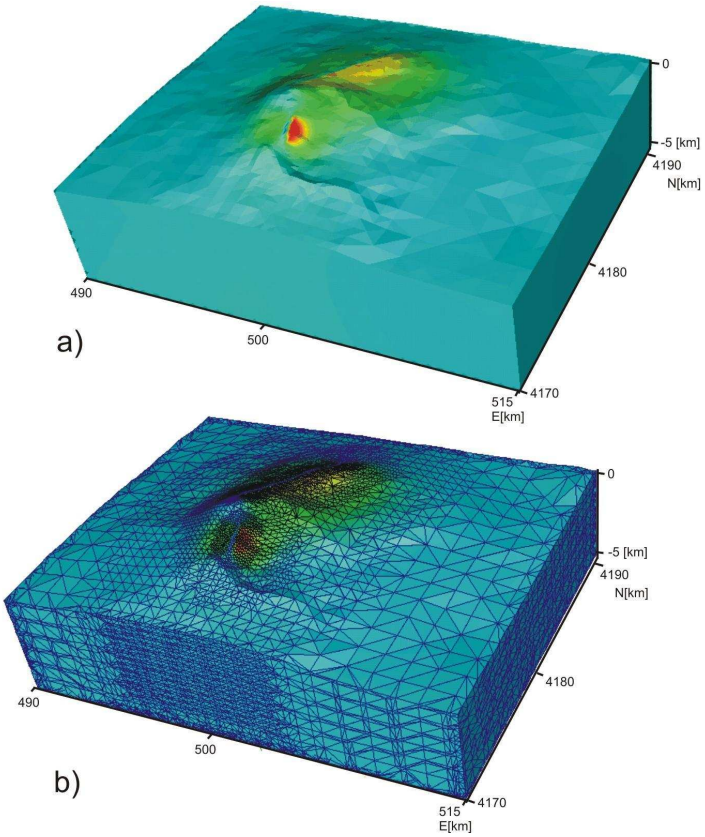

Figure 6.4. Example of computational domain (a) and FEM mesh (b) for Green's function evaluating. The mesh is refined around the dislocation sources and becomes coarser at distance.

Slip on the fault interface is represented by dislocation pairs of initially collocated nodes (Masterlark, 2003). The dislocation between a pair of nodes, initially occupying the same position, is a prescribed relative displacement between the nodes. These node-pairs deform

freely in unison in the two directions orthogonal to the dislocation vector and deform freely in tandem in the direction parallel to the dislocation vector.

Hence, each coefficient G_{ij} is a displacement component at location j due to a unit dislocation of node-pair i (Figure 6.5). The computation of the G matrix for M fault patches requires M × 3 (for strike-slip, dip-slip and tensile kinematics) model runs.

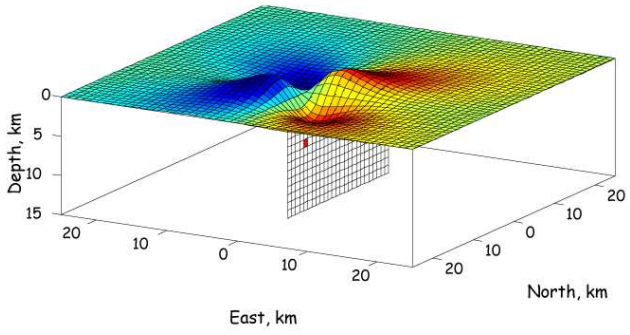

Figure 6.5. Effect of the red patch on the surface displacement for the computation of the green functions.

6.2.3 Geodetic inversion

The inverse problem consists in minimizing the difference between the observed ground deformation and that calculated with the forward modeling. Assuming that the forward problem is exactly solved by the linear Equation (6.5), the slip on each sub-fault can be found using a linear least squares inversion scheme:

$$\hat{\mathbf{s}} = [\mathbf{G}^T\mathbf{G}]^{-1}\mathbf{G}^T\mathbf{d} \tag{6.6}$$

Linear least-squares methods require to incorporate regularization techniques in order to stabilize the problem and to reduce the set of likely solution. Several studies showed that the inverse solution can yield irregular slip values on adjacent patches. This arbitrary slip model may well fit the data, but it is unrealistic: inversion of real data often result in models with alternating patches of positive and negative slip that nearly cancel out at the surface, an effect known as "checkerboarding". The checkerboarding effect stems from the magnification of noise, i.e., from the inability of the inversion to distinguish between slip on two adjacent patches to within the level of noise, or to within the available numerical precision. The idea of reducing the class of possible solutions to some set on which the solution is stable lies in the fundamental concept of introducing a regularizing operator. The inverse problem can be re-formulated as an optimization problem aimed at finding the unknown slip values s that minimize a data misfit and a smoothing functional Φ_r, defined as:

$$\phi = \phi_d + \lambda\phi_r = \frac{1}{2}\left[(\mathbf{d}-\mathbf{d}_{obs})^T(\mathbf{d}-\mathbf{d}_{obs})\right] + \lambda\phi_r \tag{6.7}$$

where λ is a regularization parameter, namely a trade-off between minimizing a measure of the data misfit Φ_d and the smoothing functional Φ_r. To avoid large variations between adjacent patches, a

smoothing functional is used in a way to minimize the second-order spatial derivative (Laplacian) of the slip distribution:

$$\phi = \frac{1}{2}\left[(\mathbf{Gs} - \mathbf{d}_{obs})^T (\mathbf{Gs} - \mathbf{d}_{obs})\right] + \lambda \mathbf{s}^T \mathbf{L}^T \mathbf{L}\mathbf{s} \tag{6.8}$$

A W_d covariance matrix could also introduced to weight different geodetic data depending on measurements uncertainties.

$$\phi = \frac{1}{2}\left[(\mathbf{Gs} - \mathbf{d}_{obs})^T W_d^T W_d (\mathbf{Gs} - \mathbf{d}_{obs})\right] + \lambda \mathbf{s}^T \mathbf{L}^T \mathbf{L}\mathbf{s} \tag{6.9}$$

The Laplacian Operator $\mathbf{L}$ is computed using a finite-difference method (Masterlark, 2003). The Laplacian Operator is introduced to avoid large variations between neighbouring dislocations and it can be solved using a finite-difference method (Equation (6.10)). The finite difference approximation (Wang and Anderson, 1982) requires a two-dimensional array, s, having column and row indices i and j, implements Laplace's equation:

$$\nabla^2 s \equiv 0 \cong \frac{s_{i-1,j} - 2s_{i,j} + s_{i+1,j}}{(\Delta x)^2} + \frac{s_{i-1,j} - 2s_{i,j} + s_{i+1,j}}{(\Delta y)^2} \tag{6.10}$$

where Δx and Δy are the respective along-strike and surface projection of the downdip fault patch dimensions (Figure 6.6).

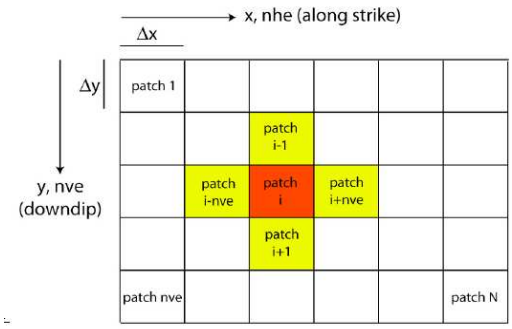

Figure 6.6. Schematic figure of *i*-th fault patch smoothed to patches at all sides.

We write the Laplacian operator in matrix form and include it in the weightening matrix W_L.

The matrix W_L is constructed so that the *n*-th row in W_L contains source component coefficients in the equation above for columns corresponding to the appropriate source (Equation 6.10).

$$W_L{}^n = \begin{vmatrix} W_{L\,(j-1)nc+i}{}^n = 2\left[(\Delta x)^{-2} + (\Delta y)^{-2}\right] \\ W_{L\,(j-1)nc+(i-1)}{}^n = (\Delta x)^{-2} \\ W_{L\,(j-1)nc+(i+1)}{}^n = (\Delta x)^{-2} \\ W_{L\,(j-2)nc+i}{}^n = (\Delta y)^{-2} \\ W_{L\,jnc+i}{}^n = (\Delta y)^{-2} \end{vmatrix} \qquad (6.11)$$

Since λ controls the sensitivity of the regularized solution, it should be chosen so that a good balance is assigned to the smoothing functional,

thereby warranting that the observations are well reproduced by the model. Among the several techniques that have been developed to properly estimate λ in inverse problem we used the L-curve criterion (Figure 6.7).

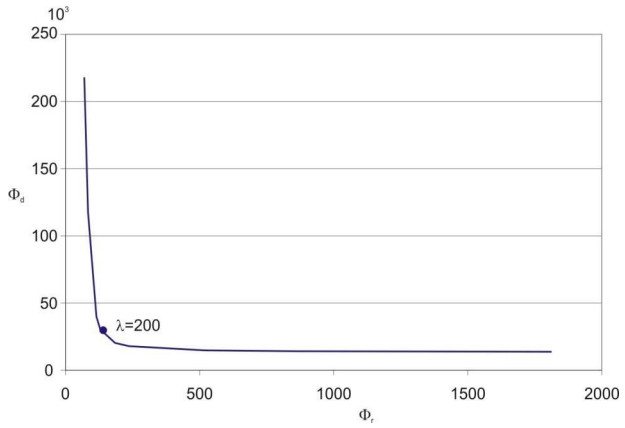

Figure 6.7 The L-curves of the data misfit versus the model norm as a function of the regularization parameter. The best value of regularization parameter lies on the corner of the L-curve.

Following this method, a family of solutions is achieved by varying lambda from 0 to ∞ and the data misfit Φ_d of the regularized solutions is plotted versus the corresponding smoothing functional Φ_r. Considering the input slip distribution of Figure 6.8a, we evaluated the possible solutions for different values of lambda. In the horizontal part of the L-curve (data misfit constant), the smoothing functional Φ_r increases rapidly without much of a decrease in the data misfit Φ_d. For higher value of lambda, the overall functional Φ is more influenced by Φ_r. Since the

smoothing functional Φ_r balances the variations between adjacent patches, the models obtained in correspondence of the horizontal part of the L-curve tend to avoid large variations between neighbouring dislocations (Figure 6.8b). In the vertical part of the L-curve (smoothing functional constant), the data misfit Φ_d increases without reducing the smoothing functional Φ_r. For lower values of lambda, the overall functional Φ is more influenced by Φ_d. Therefore, the models obtained in correspondence of the vertical part of the L-curve tend to strongly minimize the measure of the data misfit (Figure 6.8c). The value of lambda in correspondence of the point of maximum curvature represents a compromise between minimizing the data misfit Φ_d and the smoothing functional Φ_r (Figure 6.8d).

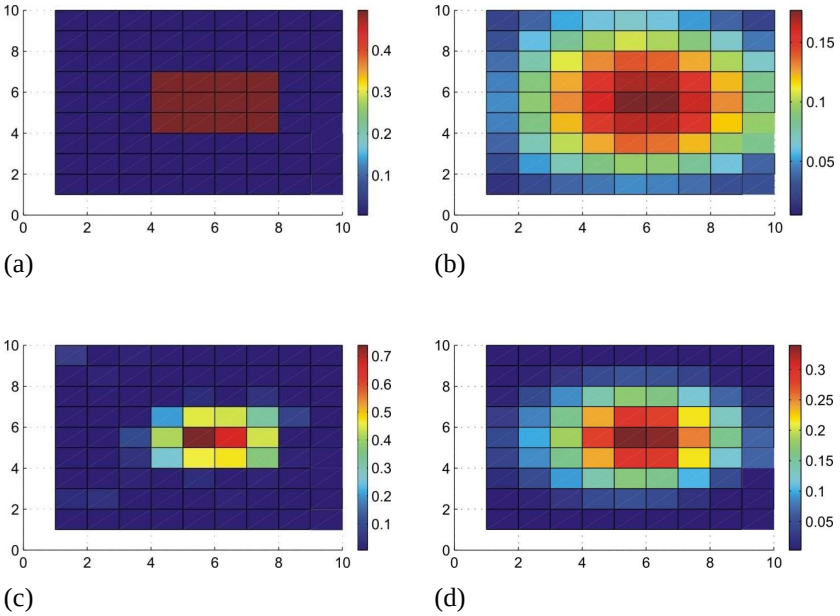

Figure 6.8. Infault slip distribution (a). Calculated slip distribution for different values of λ: (b) 1000, (c) 0 and (d) 200.

The minimization of the functional in Equation (6.8) could provide unfeasible solutions if no constraints are imposed. To ensure that the solution is reasonable, it is advisable to prescribe realistic bounds on slip values. The minimization of the quadratic functional subjected to bound constraints can be solved by using a Quadratic Programming (QP) algorithm based on an active set strategy (Gill et al., 1981):

$$\min\phi = \min\left[\frac{1}{2}\mathbf{s}^{\mathrm{T}}\mathbf{Q}\mathbf{s} - \mathbf{f}^{\mathrm{T}}\mathbf{s}\right], \quad \mathbf{L} \le \mathbf{s} \le \mathbf{U} \tag{6.12}$$

where $\mathbf{Q} = \mathbf{G}^T\mathbf{G} + \mathbf{L}^T\mathbf{L}$ and $\mathbf{f} = \mathbf{G}^T\mathbf{d}$, and $\mathbf{L}$ and $\mathbf{U}$ are the vectors of lower and upper bounds of slip values. The quadratic formulation of the problem is solved iteratively by generating a sequence of feasible solutions that converge toward the optimal solution. The iteration is stopped when no relative improvements in the functional are achieved.

6.3 Benchmark tests

The implemented procedure was validated performing several check-tests on synthetic data. Firstly, we checked whether the subdivision of the fault in patches introduces artificial error. The sum of the contribution of each patch should give the same results, within the computational error, as when the overall fault is considered. We compare the ground deformation achieved as the sum of the displacements generated by each patch and those obtained by the overall fault. In these computations a uniform slip distribution on the patch is assumed. The misfit between the two computations is shown in Figure 6.10. The error has a RMSE (root mean square error) of the order of 10-7 m, which is well below the measurement error.

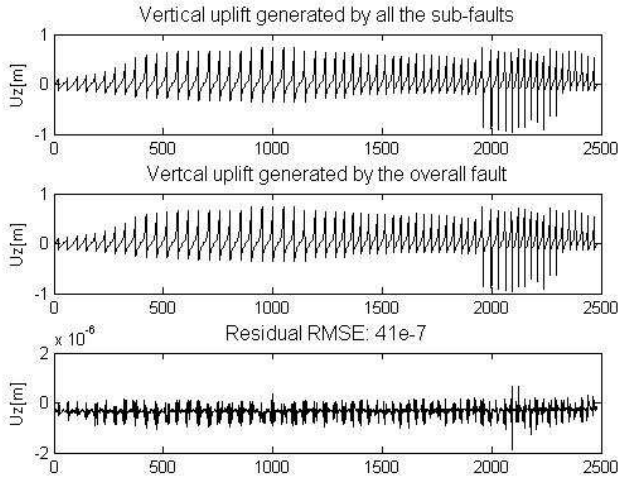

Figure 6.9. Comparison between the numerical results obtained using the overall faults and the set of patches.

Finally, synthetic tests were performed to evaluate the goodness of the inversion procedure. Indeed, the accuracy of the solution is also dependent on the number of the available observation points and their distribution with respect to the geophysical source position. For this test the data set was supposed noisy free. The experimental framework was formulated as follows. As a general case study, we assumed a uniform distribution of observation points within a regular grid of 10 × 10 km, centered on the ground projection of the dislocation sources. The RMSE between the assumed and the inverted slip is computed varying the number of measurement points within the regular grid (Figure 6.10). The inversion method is able to retrieve accurately the slip distribution when the number of observation point is greater than 750.

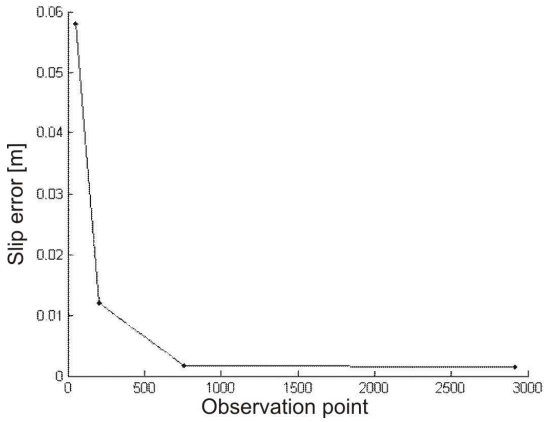

Figure 6.11. RMSE on slip distribution in function of the number of observation points.

Chapter 7

Fem-based fault slip inversion using InSAR data

The automated inversion procedure proposed in Chapter 6 was applied to estimate the heterogeneous slip distribution on Pernicana fault that could explains the ground deformation observed on Mt Etna in concomitance of the M. 3.7 earthquake occurred on 22 September 2002, which preceded of near a month the 2002-2003 eruption.

7.1 Case Study: The 22 September 2002, M 3.7 pre-eruption earthquake along Pernicana fault.

The composite deformation system that borders the northern moving flank of Mt Etna is the Pernicana Fault System (PFS). It is one of the most active tectonic structures in the Etna area, and has been very well studied in the recent decade (Bonforte et al. 2007a, Palano et

al. 2006, Acocella and Neri 2005, Neri et al. 2003, Azzaro et al. 2001). The PFS is composed of discrete segments (Figure 7.1), arranged in a right stepping en-èchelon configuration, of a near continuous left lateral shear zone. It develops eastward from the North-East Rift (NE Rift), crossing the Provenzana fault (PF) and the Pernicana fault (PeF). The long-term behavior of the slip rate of the PFS evidences a constant and continuous motion of about 2 cm/year related to the gravitational spreading of eastern flank that is occasionally accelerated by volcanic activity (Bonforte et al. 2007a). The western and central segments of the PFS are seismogenic, with frequent shallow earthquakes that can reach magnitude up to 4.2. The most recent earthquakes were recorded on 25 December 1985, 29 October 1986, and 22 September 2002 (Azzaro et al. 2001, Acocella et al., 2003).

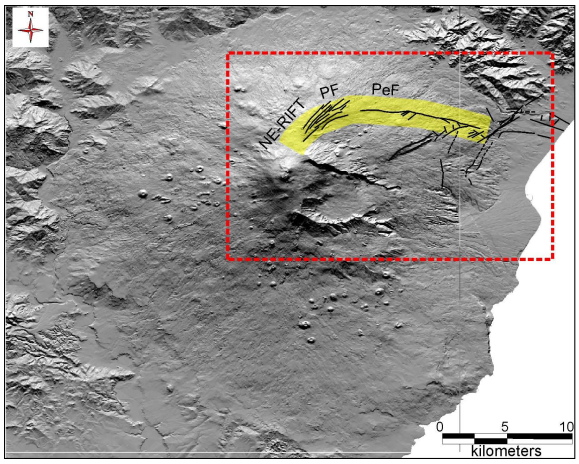

Figure 7.1. Shaded relief map of Mt Etna with the structural lineaments of the Pernicana Fault System (PFS) shown by black lines.

This structure shows a very high slip-rate (e.g. Lo Giudice and Rasà, 1992; Azzaro et al., 2001; Acocella et al., 2003; Bonforte et al., 2007b) with complex mechanisms, which are characterized from tensile (in the upper part where often the magma intrudes), to dip-strike in the intermediate zone, to pure strike in the easternmost shallow part.

The M. 3.7 earthquake, occurred on 22 September 2002 along the central part of the PFS, was accompanied by ground fracturing with left lateral movement up to 0.5 meter, propagated from west to east from the NE Rift area and then migrated to the eastern PFS (Figure 7.2).

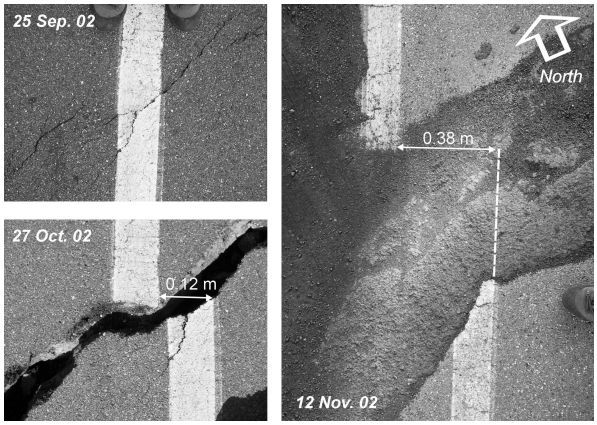

Figure 7.2 - Evolution of the horizontal displacement across a road in the central PFS as reported in Neri et al. 2004. The overall left lateral shear is clearly visible at the displaced white median strip.

The comparison between the results of the GPS survey carried out in September 2002 and in July 2002 showed a ground deformation pattern that affects the whole northeastern flank of the volcano

(Bonforte et al, 2007a). The observed direction of displacement varies along the fault (Figure 7.3). The pattern is clearly shaped by the Pernicana fault; displacements of about 2-3 cm affect all GPS stations lying on the southern side of the fault. Unexpected significant displacements, up to 2 cm, were also detected in the upper part of the NE Rift and the summit area (Bonforte et al, 2007a). The results of the geodetic surveys show a ground deformation pattern that affects the entire northeastern flank of the volcano, which couldn't be related only to the seismic event.

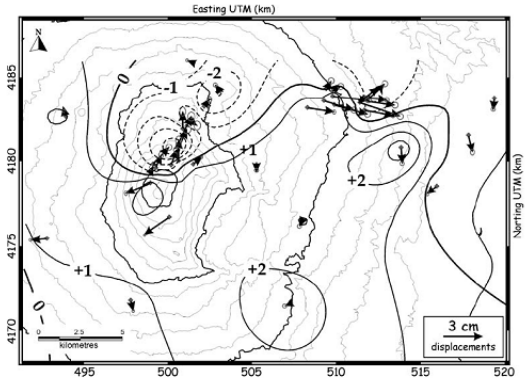

Figure 7.3. The GPS surveys carried out in September and July 2002. (from Bonforte et al.)

We also generated a differential interferogram processing two ascending ERS2 passes (31 July 2002 – 9 October 2002) by means of the ROI_PAC package developed by the JPL (Rosen, 2004) (Figure 7.4).

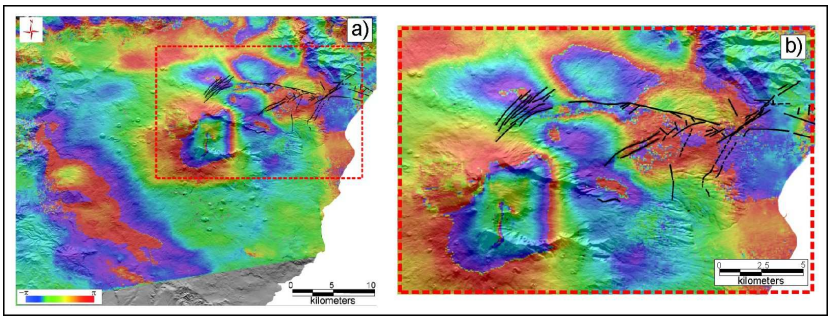

Figure 7.4. Differential interferogram for ascending scene pair 31 July 2002 to 09 October 2002: (a) phase interferogram; (b) enlargement of the PFS area. A peaked lowering is revealed in the squared area. The scale indicates the phase variation along the LOS (negative toward the radar).

The DInSAR data show a ground deformation pattern that affects the entire northeastern flank of the volcano, with a general eastward motion clearly shaped by the PFS (Bonforte et al. 2007a). The detailed ground deformation pattern in line of sight (LOS), detected by the unwrapped interferogram (Figure 7.3a), is in agreement with a transcurrent fault-system (eastward segment of PFS), a normal fault system (the central segment of PFS), and an intrusion bounding the eastward moving northeastern sector of the volcano.

The interferogram shows a high coherence due to a short perpendicular baseline (i.e. the distance between orbits) and a small temporal baseline (70 days). We have reflattened the interferogram in order to remove the orbital errors, and the final unwrapped interferogram is so affected only by instrumental and atmospheric noise. Taking into account the GPS and levelling data, Bonforte et al.

(2007b) estimated that the tropospheric noise affecting this interferogram has an uncertainty of half fringe (14 mm).

7.1.1 FEM and domain properties

In order to estimate the slip distribution along the surface ruptures we applied the FEM-based fault slip inversion, which takes into account medium heterogeneity and topography, by using the high spatial resolution DInSAR data. The numerical model is performed by using PyLith, a parallel finite element code (Williams, 2006; Aagaard et al., 2008). The computational domain is a volume extending 100 km × 100 km × 50 km to avoid artifacts in the numerical solution due to the proximity of the external boundaries. For boundary conditions, the displacements on the outermost lateral boundaries and on the bottom are fixed to zero, while the boundary at the ground surface is free. The ground surface was generated from a digital elevation model of Mt Etna from the 90 m Shuttle Radar Topography Mission (SRTM) data and a bathymetry model from the GEBCO database (http://www.gebco.net/). Using LaGriT, a 3D grid generation code from Los Alamos National Laboratory (http://lagrit.lanl.gov), the computational domain was meshed into 714012 isoparametric, and arbitrarily distorted tetrahedral elements connected by 123445 nodes. The mesh resolution is about 100 m around the sources, about 500 m in the 20 km × 20 km area around the summit craters and decreases to 2 km in the far field (Figure 7.5).

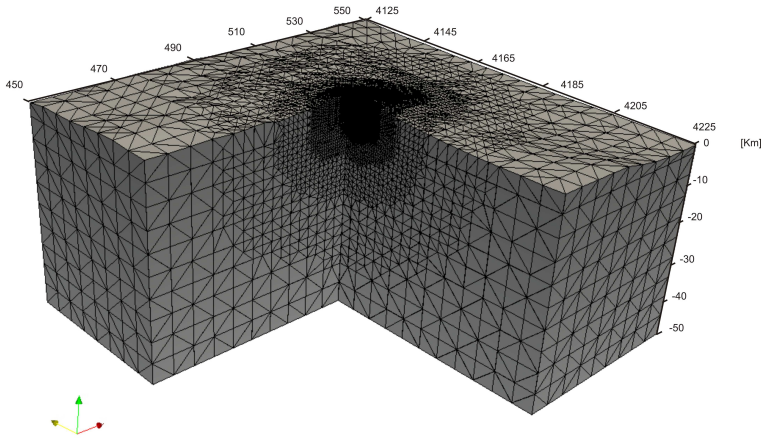

Figure 7.5. Meshed domain of the numerical model. The mesh is refined around the volcano structures and becomes coarser at greater distance.

Slip along the fault interface is implemented by means of cohesive elements. The $\mathbf{G}$ matrix is constructed by sequentially assigning a unity dislocation for each patch and null dislocations for all other patches along the faults. Therefore, the computation of the $\mathbf{G}$ matrix for M patches required M × 3 (for strike-slip, dip-slip and tensile kinematics) model runs. Since each simulation takes about 15 minutes (PE1955 Quad-Core Xeon E5310 1.6 GHz), the time for generating the $\mathbf{G}$ matrix composed of 1476 the Green's functions would have been about 8 days on a single processor. To speed-up the computational time, the procedure was parallelized to run on a cluster of 20 nodes reducing the time to about 10 hours (Figure 7.6).

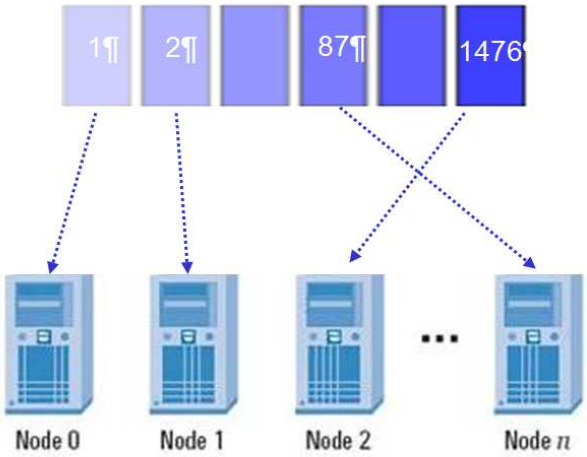

Figure 7.6. Parallelization of procedure on a cluster of 20 nodes.

The accuracy of the solutions was warranted checking the convergence of the GMRES solver. The iteration of GMRES solver is stopped when a threshold of 10^{-9} is reached or the number of iterations is higher than 300.

7.1.2 Application of Inversion algorithms

Generally, inversion of geodetic data for fault slip distribution has been based on the computations of Green's functions under the assumptions of homogeneous elastic half-space model. A kinematic slip inversion is carried out solving the linear system (6.5).

In order to account for topographic effects as well as a complex distribution of material properties, we computed the Green's functions

by using the finite-element method (FEM). The real topography is considered and the elastic parameters were estimated using the seismic P-wave and S-wave propagation velocities (V_p and V_s) inferred from tomography investigations (Patanè et al., 2006). The subsurface elastic heterogeneities of the medium were included in the numerical model by assigning to each element in the meshed domain the value of the elastic Young's modulus interpolated at the element location. Using a medium density of 2500 kg/m^3, the Young modulus varies in the range from 11.5 GPa at shallower depth to 133 GPa at greater depth.

To account for the complex geometry of the Etna's structures, the source geometry was constrained on the basis of field mapping data and previous GPS data inversion (Bonforte et al., 2007b), which infers the ground displacements and put into evidence the movements of the NE Rift, the PF and the PeF in the analyzed period (Figure 7.1). The fault surfaces extended from the free surface down to 3 km below sea level. For these three structures a left-lateral strike-slip constraint with a fault-normal expansion is imposed, whereas no restrictions are assigned on the dip-slip components. Bonforte et al. (2007b) identified also an intrusive source below the summit area. Therefore, a tensile source was also considered. To allow for a spatially heterogeneous slip, we subdivided the structures into smaller rectangular patches, whose size is 500 m × 500 m, obtaining a total number of 492 patches. These assumptions lead to an inversion problem with 1284 unknowns on the slip components. To avoid possible irregular slip values on adjacent patches, the inverse problem was regularized introducing a second-order Laplacian smoothing function and was minimized

applying a Quadratic Programming (QP) algorithm with bound constraints on slip values ranging between -0.5 m and 0.5 m.

The DInSAR data (Figure 7.7a) that provide a dense spatial resolution able to ensure a robust inversion were used to find the slip in each patch. Restricting the DInSAR data to the interested area, a set of 30080 points at a full resolution (20 m) was obtained. The image was averaged over 20 pixel (500 m resolution) resulting in a data set of 1504 points (Figure 7.7a).

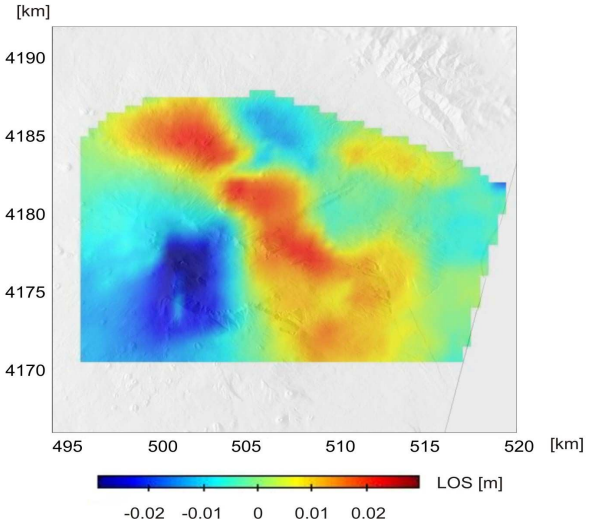

(a)

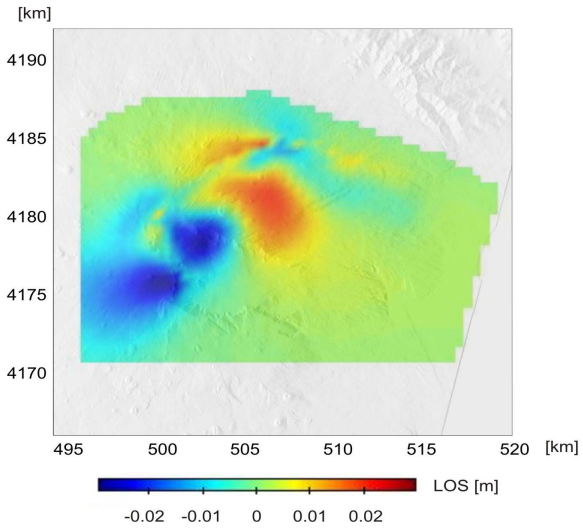

(b)

Figure 7.7. (a) Unwrapped interferogram showing the displacement in the line of sight (LOS) to the satellite. (b) Model prediction for the DInSAR observations.

The numerical inversion based on FEM model provides a complex and detailed deformation pattern (Figure 7.7b). The heterogeneous distribution of the slip along the structure is able to match the DInSAR image. The LOS residuals have an almost null mean (0.1 mm) and a Root Mean Square Error (RMSE) of about 7 mm. Misfit in the far-field could be due to atmospheric noise, whereas misfit in the near-fault may indicate that elastic assumption is inappropriate near the earthquake rupture (Figure 7.7). The resolved slip distribution along the volcanic structures is shown in Figure 7.8.

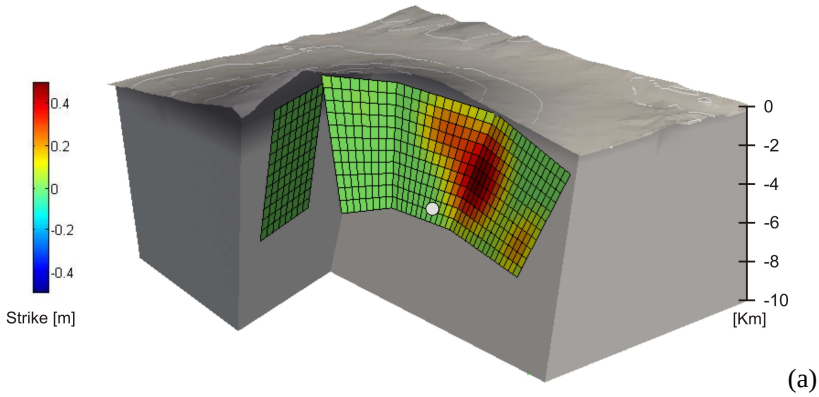

(a)

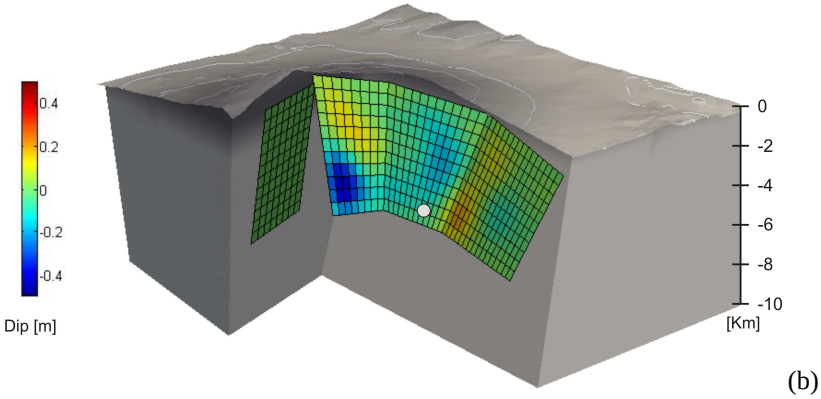

(b)

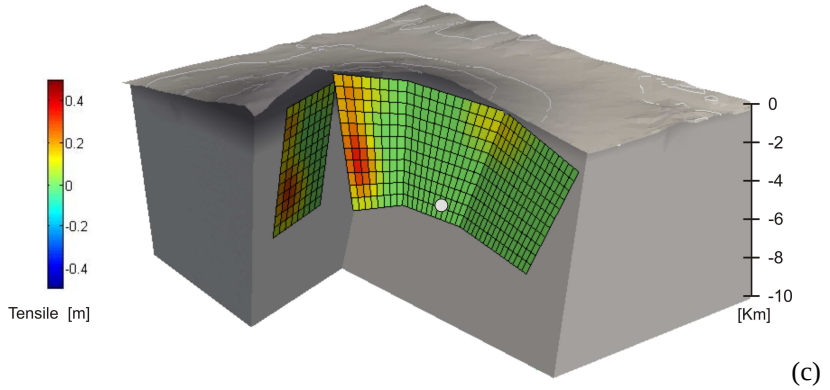

(c)

Figure 7.8 - Slip distributions along the PFS on the north-eastern flank of Mt Etna: (a) strike slip; (b) dip slip; (c) tensile opening. The earthquake hypocenter is indicated with a white circle.

The results show a complex kinematics of the north-eastern flank of the volcano involving the considered structures. The model shows the maximum strike-slip motion in the zone of the earthquake rupture. Significant tensile component are obtained not only on the intrusive source below the central summit craters but also in the upper part of the NE Rift. A variable component of dip-slip movement along the structures is also found. Considering the occurrence of the earthquake, which is associated with a limited zone of the PFS, this calculated pattern reproduces a situation more detailed than an unrealistic uniform movement of the all surfaces of the fault system.

7.1.3 Conclusions

A heterogeneous distribution of the slip along the structures is able to better justify ground deformation pattern. We implemented a general procedure through a FEM inversion, which improves the

previous results with uniform slip by considering the slip distribution of a fault embedded in a heterogeneous medium with real topography.

The presented approach proves to be a powerful tool for obtaining detailed information on fault complexities through the use of the numerous deformation data from dense geodetic networks and/or from modern satellite radar interferometry. We applied the procedure to the M. 3.7 earthquake recorded on 22 September 2002 at the PFS on Etna volcano. Our aim was to find a slip distribution along the volcanic and/or seismogenic structures, which best explains the observed inter-seismic DInSAR deformation pattern. The FEM-based inversion highlighted new important aspects and in particular a tensile mechanism, in the upper part of the fault system, interpretable as precursor of the eruption occurred a month later, and a zone of maximum shear slip coincident with the earthquake area in the central part of the PFS due to the seismic failure.

Chapter 8

Conclusions

This thesis represents a discussion on the issues relative to stress-strain processes in volcano and seismic regions yielding advances in the procedures for forward and inverse modeling of geodetic data.

The governing equation for ground deformation, an overview of the principal numerical methods and a theoretical background on volcano and seismic processes and monitoring techniques were covered in order to prepare the bases for the modeling step. The geophysical inverse problem was the unifying theme of this thesis, allowing to reveal quantitatively the structure and dynamics of the geophysical process after an evaluation of monitoring data and modeling procedures. Forward models were produced as realistic as possible employing numerical methods and an inversion procedures for FEM models were implemented. Each model was supported by a real case study as application.

Firstly, we validated the numerical method in a homogeneous elastic half-space comparing the results with those obtained from analytical models, then a comparison between analytical approaches and numerical solutions was performed. The comparison allowed to appreciate how the topography and medium heterogeneity can alter the estimate of the ground deformation with respect to the analytical solution.

Secondly numerical forward models were implemented in order to overcome the intrinsic limitation provided by the half-space assumption and give more realistic models which consider topographic effects, complicated distribution of medium properties as well as complex rheologies. In particular, a finite element model was applied to evaluate ground deformation produced by dislocation and volcanic pressurized sources. At first axi-symmetric models were solved to perform benchmark tests, and then a 3D model was implemented to obtained a more detailed analysis of the problem.

The FEM technique enabled to consider both the topography and the medium heterogeneity in modeling the intrusive event occurred at Mt Etna in July 2001. We showed as the topography significantly alters the general pattern of the ground deformation especially near the volcano summit and how, on the contrary, the medium heterogeneity does not strongly affect the expected deformation. We explored the source parameter space with a grid search, founding that, in comparison to the analytical solution, the numerical model associated with the minimum residual provides tensile source with a reduced opening and a wider extension which well matches the hypocenters of the seismic swarm occurred during the dyke intrusion. Also, we

proved that numerical and the analytical solutions are both valuable solutions given the measurement errors and the location of GPS stations. A good match between the observed and the computed deformation was achieved at most of the stations located on the summit of Etna volcano. A new model should be set up including geological structure located in the eastern flank of the volcano to better draw the complex interaction between the magmatic intrusions and the tectonic processes responsible for the kinematics of the eastern flank.

The 1993-1997 inflation phase detected at Mt. Etna by geodetic data was reviewed. The inversion of geodetic data (Bonaccorso et al. 2005) supported the presence of a pressurized spherical source beneath the summit craters which reproduced the observed displacements. A pressurized ellipsoidal source embedded in elastic medium required an exceedingly high value of pressure was needed. High overpressure values are unrealistic because the induced stresses would be such high that rocks would fracture because of the low tensile strength of common solid rocks. We demonstrated how the inclusion of a realistic anelastic behaviour could significantly lower the inferred pressure necessary to explain the observed surface deformation. Particularly, we established how the viscoelastic model enables to produce deformation comparable with those obtained from elastic model, requiring a significantly lower pressure. Nevertheless, the viscoelastic model requires a pressure increase that is still higher than crustal strength. Finally, we showed that the overpressure can be lowered to geologically satisfying values if elastoplastic behavior is taken into account. Moreover, the elastoplastic rheology is located in a

shallow broad region of low Qp that has been recognized on the west of the high rigidity body beneath the South-East flank of Etna volcano (Arevalo et al., 2005; De Gori et al., 2005; Patanè et al., 2006).

The anelastic behaviour was also investigated for describing the long term deformation following both the M. 7.3 1992 Landers and M. 7.1 1999 Hector Mine Californian earthquakes. Considering a layered viscoelastic rheology and a non-uniform slip distribution, we first simulate the Landers rupture, allow the rheology to respond to these stress changes for 7 years, then simulate the Hector Mine rupture and allow the rheology to respond for another 7 years. The simulation results were compared to those observed from GPS stations. A good match between the observed and the computed deformation was achieved at most stations in the near and middle field areas but a disregard still appears in the far field area. New models should be set up including different rheologies like power–law rheology and different mechanisms like the after-slip model in order to find a better match with the observed GPS measurement. These models could help us to discover the dominant mechanism that best explains the post-seismic deformation and to provide a better understanding of the rheological properties of the lithosphere.

As for the final target of this thesis, a numerical geophysical inverse problem was outlined and solved. We implemented a general procedure through a FEM inversion, which improves the previous results with uniform slip by considering the slip distribution of a fault embedded in a heterogeneous medium with real topography. The method allowed to invert geodetic data giving a very detailed picture of the slip distribution on fault planes involved in volcanic and

tectonic events. Furthermore it is suitable to explain the complex deformation pattern deduced from SAR interferograms.

The object of study for the FEM inversion procedure was the Pernicana fault, one of the most active structures at Mt Etna. Particularly, we studied the ground deformation observed on Mt Etna in concomitance of the M$_w$ 3.7 earthquake occurred on 22 September 2002, which preceded of near a month the 2002-2003 eruption. The FEM-based inversion highlighted new important aspects and in particular a tensile mechanism, in the upper part of the fault system, interpretable as precursor of the eruption occurred a month later, and a zone of maximum shear slip coincident with the earthquake area in the central part of the Pernicana Fault System due to the seismic failure.

The FEM inversion procedure implemented in order to retrieve the complex slip distribution on a fault surface opens new perspective in the correct interpretation of a powerful data as InSAR and in the characterization of the seismogenic structures both in volcanic and tectonic areas.

Appendix A

Assumptions for admissible mesh in FVM

Let $\mathrm{T} = (K_{i,j})_{1=1,...,N_1;\, j=1,...,N_2}$ be an admissible mesh of (0,1) X (0,1) , that is, satisfying the following assumptions.

Let $N_1 \in N^*$, $N_2 \in N^*$, $h_1,...,h_{N_1} > 0$, $k_1,...,k_{N_2} > 0$ such that

$$\sum_{i=1}^{N_1} h_i = 1,\ \sum_{i=1}^{N_2} k_i = 1, \tag{A.1}$$

and let $h_0 = 0$, $h_{N_1+1} = 0$, $k_0 = 0$, $k_{N_2+1} = 0$.

For $i = 1,...,N_1$, let

$$x_{\frac{1}{2}} = 0,\ x_{i+\frac{1}{2}} = x_{i-\frac{1}{2}} + h_i, \tag{A.2}$$

so that $x_{N_1+\frac{1}{2}} = 1$, and for $j = 1,...,N_2$,

$$y_{\frac{1}{2}} = 0,\ y_{j+\frac{1}{2}} = y_{j-\frac{1}{2}} + k_j \tag{A.3}$$

so that $y_{N_2+\frac{1}{2}} = 1$ and

$$K_{i,j} = \left[x_{i-\frac{1}{2}}, x_{i+\frac{1}{2}} \right] \times \left[y_{j-\frac{1}{2}}, y_{j+\frac{1}{2}} \right]. \tag{A.4}$$

Let $(x_i)_{i=0,N_1+1}$, and $(y_j)_{j=0,N_2+1}$, such that

$$x_{i-\frac{1}{2}} < x_i < x_{i+\frac{1}{2}}, \tag{A.5}$$

for $i = 1,...,N_1$, $x_0 = 0$, $x_{N_1+1} = 1$,

$$y_{j-\frac{1}{2}} < y_i < y_{j+\frac{1}{2}}, \tag{A.6}$$

for $j = 1,...,N_2$, , $y_0 = 0$ $y_{N_2+1} = 1$,

And let $x_{i,j} = (x_i, x_j)$, for $i = 1,...,N_1$, $j = 1,...,N_2$; set

$$h_i^- = x_i - x_{i-\frac{1}{2}}, \; h_i^+ = x_{i+\frac{1}{2}} - x_i, \tag{A.7}$$

for $i = 1,...,N_1$,

$$h_{i+\frac{1}{2}} = x_{i+1} - x_i . \tag{A.8}$$

for $i = 0,..., N_1$,

$$k_j^- = y_j - y_{j-\frac{1}{2}},\ k_j^+ = y_{j+\frac{1}{2}} - y_j , \tag{A.9}$$

for $j = 1,..., N_2$,

$$k_{j+\frac{1}{2}} = y_{j+1} - y_j , \tag{A.10}$$

for $j = 0,..., N_2$.

Let $h = \max\{(h_i, i = 1,..., N_1), (h_j, j = 1,..., N_2)\}$.

Appendix B

Fundamental solution of the 2D Laplace equation

The derivation starts out by transforming the Laplace operator to polar coordinates *(r,ϕ)*

$$G_{,ii} = \frac{1}{r}(rG_{,r})_{,r} + \frac{1}{r^2}G_{,\phi\phi}. \tag{B.1}$$

The excitation with the Dirac impulse is radial-symmetric and, since we are dealing with an infinite problem, there are no disturbances from the boundary, it is implied that the fundamental solution is radial-symmetric, too. Thus the last term in Equation (B.1) vanishes. The Dirac impulse in polar coordinates is stated as

$$\delta(|x-\xi|) = \delta(r)/2\pi r. \tag{B.2}$$

Hence, a way to solve for ***G*** is to integrate Equation (B.1). This yields

$$\frac{1}{r}(rG_{,r})_{,r} = \frac{\delta(r)}{2\pi r}. \tag{B.3}$$

$$rG_{,r} = -\int \frac{\delta(r)}{2\pi} dr = -\frac{1}{2\pi} + C_1$$

$$G_{,r} = -\frac{1}{2\pi r} + \frac{C_1}{r}$$

$$G(r) = -\frac{1}{2\pi} \ln r + C_1 \ln r + C_2 \tag{B.4}$$

with the integration constants $\boldsymbol{C_1}$ and $\boldsymbol{C_2}$. It will be shown in the following that $\boldsymbol{C_1=0}$ for Equation (B.2) being a valid solution of the Laplace equation

$$G_{,ij} = \delta(|x - \xi|)\,. \tag{B.5}$$

The constant C_2.introduces the notion of a constant potential. It is arbitrary and is generally set to zero.

The validity of a fundamental solution can be verified by evaluating the impulse condition. This condition carries out the integral over the partial differential equation over an arbitrary volume enclosing the Dirac impulse

$$\int_{\Omega_\infty} G_{,ij} d\Omega = -\int_{\Omega_\infty} \delta(x) d\Omega = -1. \tag{B.6}$$

Application of Gauss' theorem transforms the volume integral on the left to a surface integral

$$\int_{\Omega} G_{,ij} d\Omega = -\int_{\Gamma} G_{,i} n_i d\Gamma \,. \tag{B.7}$$

Since ***G*** is radial-symmetric, the gradient is also a pure function of the radius. In polar coordinates this reads as

$$G_{,i} = [G_{,r} \quad 0]^T \,. \tag{B.8}$$

Moreover, the outward normal on a circle is defined in polar coordinates as

$$n = [1 \quad 0]^T \,. \tag{B.9}$$

Choosing the surface $\boldsymbol{\Gamma}$ as a circle of arbitrary radius leads to the impulse condition

$$\int_{\Gamma} G_{,i} n_i d\Gamma = -1 \,. \tag{B.10}$$

Since ***G*** depends only on ***r*** and ***r*** is constant on a specific circle $\boldsymbol{\Gamma}$, the impulse condition is reformulated as

$$G_{,r} \int_{\Gamma} d\Gamma = -1 \,.$$

$$G_{,r} \Gamma = -1$$

$$-\frac{1}{2\pi r}2\pi r=-1 \tag{B.11}$$

which proves that Equation (B.2) is indeed a valid fundamental solution of Equation (B.4). Note that this condition also implies the $\boldsymbol{C}_1$ must be zero as stated before because otherwise the terms would not cancel to -1.

Appendix C

Fundamental solution of the 3D Laplace equation

In the 3D case a transformation on spherical coordinates of the Laplace operator is carried out

$$G_{,ii} = \frac{1}{r^2}\left[(r^2 G_{,r})_{,r} + \frac{1}{\sin^2 \vartheta} G_{,\varphi\varphi} + G_{,\vartheta\vartheta} + \frac{1}{\tan \vartheta} G_{,\vartheta}\right]. \tag{C.1}$$

Assuming radial symmetry yields

$$G_{,ii} = \frac{1}{r^2}(r^2 G_{,r})_{,r}. \tag{C.2}$$

The Dirac impulse in spherical coordinates is

$$\delta(x_1)\delta(x_2)\delta(x_3) = \frac{\delta(r)}{4\pi r^2}. \tag{C.3}$$

since

$$\int_{\Omega_\infty} \delta(x_1)\delta(x_2)\delta(x_3)d\Omega = .$$

$$= \int_{-\infty}^{+\infty} \delta(x_1)dx_1 \int_{-\infty}^{+\infty} \delta(x_2)dx_2 \int_{-\infty}^{+\infty} \delta(x_3)dx_3 = 1 \qquad \text{(C.4)}$$

and by equivalence

$$\int_{\Omega_\infty} \frac{\delta(r)}{4\pi r^2} d\Omega = \int_0^{+\infty} \frac{\delta(r)}{4\pi r^2} r^2 dr \int_0^{\pi} \sin\vartheta d\vartheta \int_0^{2\pi} d\varphi = 1. \qquad \text{(C.5)}$$

The integration of the Laplace equation yields for the 3D case

$$\frac{1}{r^2}(r^2 G_{,r})_{,r} = -\frac{\delta(r)}{4\pi r^2} .$$

$$r^2 G_{,r} = -\int \frac{\delta(r)}{4\pi} dr = -\frac{1}{4\pi} - C_1$$

$$G_{,r} = -\frac{1}{4\pi r^2} - \frac{C_1}{r^2}$$

$$G(r) = \frac{1}{4\pi r} + \frac{C_1}{r} + C_2 \qquad \text{(C.6)}$$

Again, the impulse condition will show that C_1=0. As before $\boldsymbol{C}_2$ is arbitrary and is set to zero for convenience.

The integral over the partial differential equation is transformed to the boundary. Since the solution is radial symmetric the gradient has only a component in the radial direction.

$$G_{,i} = \begin{bmatrix} G_{,r} & 0 & 0 \end{bmatrix}^T . \tag{C.7}$$

A sphere is chosen as arbitrary enclosing surface in the 3D case. The normal vector is a unit vector in spherical coordinates

$$n = \begin{bmatrix} 1 & 0 & 0 \end{bmatrix}^T . \tag{C.8}$$

With this the impulse condition is

$$\int_{\Gamma} G_{,r} d\Gamma = -1. \tag{C.9}$$

Again, $\boldsymbol{G}$ only depends on $\boldsymbol{r}$ and thus is constant on a sphere of constant radius. It follows

$$\begin{aligned} & G_{,r} \int_{\Gamma} d\Gamma = -1 . \\ & G_{,r} \Gamma = -1 \\ & -\frac{1}{4\pi r^2} 4\pi r^2 = -1 \end{aligned} \tag{C.10}$$

This shows that C_1 must be set to zero so that $\boldsymbol{G}$ fulfills this equation.

Appendix D

FEM formulation of elastic problems

Three dimensional elastic problems were the first successful examples of the application of Finite Element Method. The general finite element procedure to fully-dimensional problems of stress analysis embrace clearly all the practical cases, though for some, the various two-dimensional approximations give an adequate and more economical model.

is a triangle. In three dimensions, The simplest continuum element is a tetrahedron. It is immediately obvious that the number of simple tetrahedral elements which has to be used to achieve a given degree of accuracy has to be very large. This will be result in very large numbers of simultaneous equations in practical problems, which may place a severe limitation on the use of the method in practice. Further, the band width of the resulting equation system becomes large, leading to big computer storage requirements.

The state of displacement of a point is defined by three displacement components u, v and w, in directions of the three coordinates x, y and z. Thus

$$\mathbf{u} = \begin{Bmatrix} u \\ v \\ w \end{Bmatrix} \tag{D.1}$$

A linear variation is defined by the four nodal values,

$$u = \alpha_1 + \alpha_2 x + \alpha_3 y + \alpha_4 z \tag{D.2}$$

equating the values of displacement at the nodes we have four equations of the type

$$u_i = \alpha_1 + \alpha_2 x_i + \alpha_3 y_i + \alpha_4 z_i \tag{D.3}$$

from which α_1 to α_4 can be evaluated.
It is possible to write this solution by using a determinant form,

$$u = \frac{1}{6V}[(a_i + b_i x + c_i y + d_i z)u_i + (a_j + b_j x + c_j y + d_j z)u_j + (a_m + b_m x + c_m y + d_m z)u_m + (a_p + b_p x + c_p y + d_p z)u_p] \tag{D.4}$$

with

$$6V = \det\begin{bmatrix} 1 & x_i & y_i & z_i \\ 1 & x_j & y_j & z_j \\ 1 & x_m & y_m & z_m \\ 1 & x_p & y_p & z_p \end{bmatrix} \tag{D.5}$$

in which, incidentally, the value V represents the volume of the tetrahedron. By expanding the other relevant determinants into their co-factors we have

$$a_i = \det\begin{bmatrix} x_j & y_j & z_j \\ x_m & y_m & z_m \\ x_p & y_p & z_p \end{bmatrix} b_i = -\det\begin{bmatrix} 1 & y_j & z_j \\ 1 & y_m & z_m \\ 1 & y_p & z_p \end{bmatrix} \tag{D.6}$$

$$a_i = \det\begin{bmatrix} x_j & 1 & z_j \\ x_m & 1 & z_m \\ x_p & 1 & z_p \end{bmatrix} a_i = -\det\begin{bmatrix} x_j & y_j & 1 \\ x_m & y_m & 1 \\ x_p & y_p & 1 \end{bmatrix} \tag{D.7}$$

with the other constants defined by cyclic interchange of the subscripts in the order *p,I,j,m*.

The element displacement is defined by the 12 displacement components of the nodes as

$$\mathbf{a} = \begin{Bmatrix} \mathbf{a}_i \\ \mathbf{a}_j \\ \mathbf{a}_m \\ \mathbf{a}_p \end{Bmatrix} \tag{D.8}$$

with

$$\mathbf{a} = \begin{Bmatrix} u_i \\ v_i \\ w_i \end{Bmatrix} \text{ etc.} \tag{D.9}$$

We can write the displacement of an arbitrary points as

$$\mathbf{u} = [\mathbf{I}N_i, \mathbf{I}N_j, \mathbf{I}N_m, \mathbf{I}N_p]\mathbf{a}^e \tag{D.10}$$

with shape functions defined as

$$N_i = \frac{a_i + b_i x + c_i y + d_i z}{6V}, \text{ etc.} \tag{D.11}$$

and $\mathbf{I}$ being a three identity matrix.

The displacement functions used will obviously satisfy continuity requirements on interfaces between various elements. This fact is a direct corollary of the linear nature of the variation of displacement.

Six strain components are relevant in full three-dimensional analysis. The strain matrix can now be defined as

$$\boldsymbol{\varepsilon} = \begin{Bmatrix} \varepsilon_x \\ \varepsilon_y \\ \varepsilon_z \\ \gamma_{xy} \\ \gamma_{yz} \\ \gamma_{zx} \end{Bmatrix} = \begin{Bmatrix} \dfrac{\partial u}{\partial x} \\ \dfrac{\partial v}{\partial y} \\ \dfrac{\partial w}{\partial z} \\ \dfrac{\partial u}{\partial y} + \dfrac{\partial v}{\partial x} \\ \dfrac{\partial v}{\partial z} + \dfrac{\partial w}{\partial y} \\ \dfrac{\partial w}{\partial x} + \dfrac{\partial u}{\partial z} \end{Bmatrix} = \mathbf{Su} \tag{D.12}$$

following the standard notation of Timoshenko's elasticity text. Using Equations (D.4) to (D.10) it is an easy matter to verify that

$$\boldsymbol{\varepsilon} = \mathbf{B}\mathbf{a}^e = [\mathbf{B}_i, \mathbf{B}_j, \mathbf{B}_m, \mathbf{B}_p]\mathbf{a}^e \tag{D.13}$$

in which

$$B_i = \begin{bmatrix} \frac{\partial N_i}{\partial x}, & 0, & 0 \\ 0, & \frac{\partial N_i}{\partial y}, & 0 \\ 0, & 0, & \frac{\partial N_i}{\partial z} \\ \frac{\partial N_i}{\partial y}, & \frac{\partial N_i}{\partial x}, & 0 \\ 0, & \frac{\partial N_i}{\partial z}, & \frac{\partial N_i}{\partial y}, \\ \frac{\partial N_i}{\partial z}, & 0, & \frac{\partial N_i}{\partial x}, \end{bmatrix} = \frac{1}{6V} \begin{bmatrix} b_{i,} & 0, & 0 \\ 0, & c_{i,} & 0 \\ 0, & 0, & d_{i,} \\ c_{i,} & b_{i,} & 0 \\ 0, & d_{i,} & c_{i,} \\ d_{i,} & 0, & b_{i,} \end{bmatrix} \tag{D.14}$$

with other submatrices obtained in a similar manner simply by interchange of subscripts.

Initial strains, such as those due to thermal expansion, can be written in the usual way as a six-component vector which, for example, in an isotropic thermal expansion is simply

$$\boldsymbol{\varepsilon}_0 = \begin{Bmatrix} \alpha\theta^e \\ \alpha\theta^e \\ \alpha\theta^e \\ 0 \\ 0 \\ 0 \end{Bmatrix} \tag{D.15}$$

With α being the expansion coefficient and θ^e the average element temperature rise.

With complete anisotropy the $\mathbf{D}$ matrix relating the six stress components to the strain components can contained 21 independent constants. In general, thus,

$$\sigma = \begin{Bmatrix} \sigma_x \\ \sigma_y \\ \sigma_z \\ \tau_{xy} \\ \tau_{yz} \\ \tau_{zx} \end{Bmatrix} \tag{D.16}$$

Although no difficulty presents itself in computation when dealing with such materials, since the multiplication will never be carried out explicitly, it is convenient to recapitulate here the $\mathbf{D}$ matrix for an isotropic material. This, in terms of the usual elastic constants E (modulus) and ν (Poisson's ratio), can be written as

$$\mathbf{D} = \frac{E(1-\nu)}{(1+\nu)(1-2\nu)}.$$

$$\cdot\begin{bmatrix} 1, & \nu/(1-\nu), & \nu/(1-\nu), & 0, & 0, & 0 \\ & 1, & \nu/(1-\nu), & 0, & 0, & 0 \\ & & 1, & 0, & 0, & 0 \\ & & & \frac{1-2\nu}{2(1-\nu)}, & 0, & 0 \\ & & & & \frac{1-2\nu}{2(1-\nu)}, & 0 \\ & & & & & \frac{1-2\nu}{2(1-\nu)} \end{bmatrix}. \quad \text{(D.17)}$$

Appendix E

FEM formulation of viscoelastic problems

The phenomenon of creep is manifested by a time-dependent deformation under a constant strain. Thus, in addition to an instantaneous strain, the material develops creep strain ε_c which generally increase with duration of loading. The constitutive law of creep will usually be of a form in which the rate of creep strain is defined as some function of stresses and total creep strain

$$\dot{\boldsymbol{\varepsilon}}^c \equiv \frac{d\boldsymbol{\varepsilon}_c}{dt} = \boldsymbol{\beta}(\boldsymbol{\sigma}, \boldsymbol{\varepsilon}^c) . \tag{E.1}$$

If we consider that the instantaneous strains are elastic, the total strain can be written as

$$\boldsymbol{\varepsilon} = \boldsymbol{\varepsilon}^e + \boldsymbol{\varepsilon}^c . \tag{E.2}$$

with

$$\boldsymbol{\varepsilon}^e = \mathbf{D}^{-1}\boldsymbol{\sigma} . \tag{E.3}$$

Neglecting any initial strains or stresses. As usual the equilibrium conditions

$$\int_{\Omega} \mathbf{B}^T \boldsymbol{\sigma} d\Omega - \mathbf{f} = 0 . \tag{E.4}$$

hold at all times and, if the initial conditions of the system are known, the system of Equations (E.1)-(E.4) gives a solvable first order system of ordinary differential equations with non linear coefficients.

In particular, if we consider an interval time Δt_n at the beginning of which the state, characterized by a set of parameters $\mathbf{a}_n$, $\boldsymbol{\sigma}_n$ and forces $\mathbf{f}_n$, is known, we can write a set of non linear a set of algebraic equations linking the initial conditions with the final ones at time $t_n + \Delta t_n = t_{n+1}$. Thus we have to solve the non linear set of equilibrium equations

$$\Psi_{n+1} = \int_{\Omega} \mathbf{B}^T \boldsymbol{\sigma}_{n+1} d\Omega + \mathbf{f}_{n+1} = 0 . \tag{E.5}$$

With an appropriate constitutive relation linking the stress and strain changes. Now this can be rewritten as

$$\begin{aligned} \Delta\boldsymbol{\sigma}_n &= \mathbf{D}(\Delta\varepsilon_n - \Delta\varepsilon_n^c) . \\ \Delta\varepsilon_n^c &= \Delta t \boldsymbol{\beta}_{n+\theta} \end{aligned} \tag{E.6}$$

Where $\boldsymbol{\beta}_{n+\theta}$ is calculated as

$$\boldsymbol{\beta}_{n+\theta} = (1-\theta)\boldsymbol{\beta}_n + \theta\boldsymbol{\beta}_{n+1}. \tag{E.7}$$

On eliminating $\Delta\varepsilon_n^c$ we have simply a non linear equation

$$\mathbf{R}_{n+1} \equiv \Delta\boldsymbol{\sigma}_n - \mathbf{DB}\Delta\mathbf{a}_n + D\Delta t\boldsymbol{\beta}_{n+0} = 0. \tag{E.8}$$

This system of equations (E.5) and (E.8) can be solved iteratively using the Newton – Rapson procedure.

Viscoelastic phenomena are characterized by the fact that the rate at which creep strains develop depends not only on the current state of stress and strain but on the fully history of their development. In linear viscoelasticity it is always possible to write the stress strain relationship in a form similar to that of elasticity, with the various terms of the D matrix representing now, in place of elastic constants, suitable differential or integral operators. Typically the creep part of the strain may thus .be described by

$$\boldsymbol{\varepsilon}_c = \overline{\mathbf{D}}\boldsymbol{\sigma}. \tag{E.9}$$

with

$$\overline{\mathbf{D}}_{rs} = \frac{a_0 + a_1(d/dt) + a_2(d^2/dt^2) + \ldots}{b_0 + b_1(d/dt) + b_2(d^2/dt^2) + \ldots}. \tag{E.10}$$

Here the operators are written in the differential form. If this expansion is finite, then separating any instantaneous elastic effects one can usually rewrite Equation (E.10) in terms of partial fractions as

$$\overline{\mathbf{D}}_{rs} = \frac{A_1}{(d/dt) + B_1} + \frac{A_2}{(d/dt) + B_2} + \ldots . \tag{E.11}$$

This can be interpreted, for example, as a response of a series of Kelvin elements.

Appendix F

FEM formulation of plastic problems

Plastic behaviour of solids is characterized by a non unique stress-strain relationship. If uniaxial behaviour of a material is considered, a non-linear relationship on loading alone does not determine whether non-linear elastic or plastic behaviour is exhibited. Unloading will immediately discover the difference, with the elastic material following the same path and the plastic material showing a history-dependent path.

Many materials show an ideal plastic behaviour obeying von Mises' yielding criterion in which a limiting yield stress, σ_y, exists at which the strains are indeterminate. For all stresses below such yield a linear elasticity relationship is assumed. It is generally postulated that yielding can occur only if the stresses satisfy the general yield criterion

$$F(\boldsymbol{\sigma}, \kappa)=0, \tag{F.1}$$

where κ is a hardening parameter. This yield condition can be visualized as a surface in n-dimensional space of stress with the position of the surface dependent on the instantaneous value of the state parameter κ. The basic behaviour defining the plastic strain

increments is related to the yield surface; if $d\varepsilon_p$ denotes the increment of plastic strain then

$$d\boldsymbol{\varepsilon}^p = d\lambda \frac{\partial F}{\partial \boldsymbol{\sigma}} \tag{F.2}$$

In this $d\lambda$ is a proportionality constant, as yet undetermined. The rule is known as the normality principle because relation (F.2) can be interpreted as requiring the normality of the plastic strain increment vector to the yield surface in the space of n stress and strain dimensions. Restrictions of the above rule can be removed by specifying separately a plastic potential

$$Q = Q(\boldsymbol{\sigma}, \kappa) \tag{F.3}$$

which defines the plastic strain increment similarly to Eq. (F.2), giving this as

$$d\boldsymbol{\varepsilon}^p = d\lambda \frac{\partial Q}{\partial \boldsymbol{\sigma}} . \tag{F.4}$$

The particular case of $Q=F$ is known as associated plasticity. When this relation is not satisfied the plasticity is non-associated. In what follows this more general form will be considered.

During an infinitesimal increment of stress, changes of strain are assumed to be divisible into elastic and plastic parts. Thus

$$d\varepsilon = d\varepsilon^e + d\varepsilon^p \tag{F.5}$$

The elastic strain increments are related to stress increments by a symmetric matrix of constants **D**. We can thus write Eq. (F.5) incorporating the plastic relation as

$$d\varepsilon = \mathbf{D}^{-1} d\boldsymbol{\sigma} + \frac{\partial Q}{\partial \boldsymbol{\sigma}} d\lambda \tag{F.6}$$

The plastic increment of strain will occur only if the elastic stress increment

$$d\boldsymbol{\sigma}^e = \mathbf{D} d\varepsilon \tag{F.7}$$

tents to put the stress outside the yield surface, i.e. is then plastic loading direction. If, on the other hand, this stress change is such that unloading occurs then no plastic straining will be present. The test of the above relation is therefore crucial in differentiating between loading and unloading operations and underlines the importance of the straining path in computing stress changes.

When plastic loading is occurring the stresses are on the yield surface given by Eq. (F.1). differentiating this we can therefore write

$$dF = \frac{\partial F}{\partial \sigma_1} d\sigma_1 + \frac{\partial F}{\partial \sigma_2} d\sigma_2 + \ldots + \frac{\partial F}{\partial \kappa} d\kappa = 0 \tag{F.8}$$

$$\left\{\frac{\partial F}{\partial \boldsymbol{\sigma}}\right\}^T d\boldsymbol{\sigma} - A d\lambda = 0 \tag{F.9}$$

in which we make the substitution

$$A = -\frac{\partial F}{\partial \kappa}\frac{d\kappa}{d\lambda} \tag{F.10}$$

Equations (F.6) and (F.9) can now be written in a single matrix form as

$$\begin{Bmatrix} d\varepsilon \\ 0 \end{Bmatrix} = \begin{bmatrix} D^{-1} & \left\{\frac{\partial Q}{\partial \boldsymbol{\sigma}}\right\} \\ \left\{\frac{\partial F}{\partial \boldsymbol{\sigma}}\right\}^T & -A \end{bmatrix} \begin{Bmatrix} d\boldsymbol{\sigma} \\ d\lambda \end{Bmatrix} \tag{F.11}$$

the indeterminate constant dλ can now be eliminated. This results in an explicit expansion that determines the stress changes in terms of imposed strain changes with

$$d\boldsymbol{\sigma}^e = \mathbf{D}_{ep}^* d\varepsilon \tag{F.12}$$

and

$$\mathbf{D}_{ep}^* = \mathbf{D} - \mathbf{D}\left\{\frac{\partial Q}{\partial \boldsymbol{\sigma}}\right\}\left\{\frac{\partial F}{\partial \boldsymbol{\sigma}}\right\}^T \mathbf{D}\left[A + \left\{\frac{\partial F}{\partial \boldsymbol{\sigma}}\right\}^T \mathbf{D}\left\{\frac{\partial Q}{\partial \boldsymbol{\sigma}}\right\}\right]^{-1} \tag{F.13}$$

The elastoplastic matrix $\mathbf{D}^*_{ep}$ takes the place of the elasticity matrix $\mathbf{D}_T$ in incremental analysis. This matrix is symmetric only when the plasticity is associated. The non-associated material will present special difficulties if tangent modulus procedures other than the modified Newton-Raphson method are used. The matrix is defined even for ideal plasticity when A=0.

Clearly for ideal plasticity with no hardening, A is simply zero. If hardening is considered, attention must be given to the nature of the parameter (or parameters) κ on which the shifts of the yield surface depend. With a work hardening material κ is sometimes taken to be the amount of plastic work done during plastic deformation. Thus

$$d\kappa = \sigma_1 d\varepsilon_1^p + \sigma_2 d\varepsilon_2^p + ... = \sigma^T d\varepsilon^p \tag{F.14}$$

Using the flow rule we have alternatively

$$d\varepsilon^p = d\lambda \frac{\partial Q}{\partial \boldsymbol{\sigma}} \tag{F.15}$$

Substituting Eq. (14) into Eq. (9) we see that $d\lambda$ disappears and we can write

$$A = \frac{\partial F}{\partial \kappa} \boldsymbol{\sigma}^T \frac{\partial Q}{\partial \boldsymbol{\sigma}} \tag{F.16}$$

This assumes a determinate form if the explicit relationship between F and κ is known. A similar interpretation occurs for different hardening assumptions.

To illustrate some of the concepts consider the particular case of the well-known Huber-von Mises surface with an associated flow rule. This is given by

$$F = \left[\frac{1}{2}(\sigma_1-\sigma_2)^2+\frac{1}{2}(\sigma_2-\sigma_3)^2+\frac{1}{2}(\sigma_3-\sigma_1)^2+3\sigma_4^2+3\sigma_5^2+3\sigma_6^2\right]^{1/2}+$$

$$-\sigma_y \equiv \bar{\sigma}-Y \tag{F.17}$$

in which the suffixes 1, 2, 3 refer to the normal stress components and 4, 5, 6 to shear stress components in a general three-dimensional stress state. In the above, $\bar{\sigma}$ is the second stress invariant.
On differentiation it will be found that

$$\frac{\partial F}{\partial \sigma_1}=\frac{3s_1}{2\bar{\sigma}}, \qquad \frac{\partial F}{\partial \sigma_2}=\frac{3s_2}{2\bar{\sigma}}, \qquad \frac{\partial F}{\partial \sigma_3}=\frac{3s_3}{2\bar{\sigma}},$$
$$\frac{\partial F}{\partial \sigma_4}=\frac{3s_4}{2\bar{\sigma}}, \qquad \frac{\partial F}{\partial \sigma_5}=\frac{3s_5}{2\bar{\sigma}}, \qquad \frac{\partial F}{\partial \sigma_6}=\frac{3s_6}{2\bar{\sigma}}, \tag{F.18}$$

in which the dashes stand for deviatoric stresses:

$$s_1=\sigma_1-\frac{\sigma_1+\sigma_2+\sigma_3}{3}, \text{ etc.} \tag{F.19}$$

The quantity Y(κ) is the uniaxial stress at yield. If a plot of the uniaxial test giving $\bar{\sigma}$ versus the plastic uniaxial strain ε'_u is avaible and if simple work hardening is assumed, then

$$d\kappa = Y d\varepsilon_u^p \tag{F.20}$$

and

$$-\frac{\partial F}{\partial \kappa} = \frac{\partial Y}{\partial \kappa} = \frac{\partial Y}{\partial \varepsilon_u^p}\frac{1}{Y} = \frac{H}{Y} \tag{F.21}$$

in which H is the slope of the plot at the particular value of $\bar{\sigma}$.
On substituting into Eq. (15) we obtain, after some transformation, simply A=H where H is known as the plastic modulus. This reestabilishes the well-known Prandtl-Reuss stress-strain relations.
We have so far assumed that the parameter κ is associated with the plastic work done and this, being a scalar quantity, will obviously change the yield surface by a simple expansion or contraction (isotropic hardening). Such models are found to be deficient in reproducing the true behaviour of some materials and kinematic hardening theories have been introduced in which dependence on the direction of plastic straining is noted.

An alternative, utilizing the finite element procedure directly, is that of modeling the material by an overlay technique. In this, two or more simple, ideally plastic material are assumed to act in parallel subject to the same strain increments. This of course produces an effect of a hardening material with almost the same characteristics as

those achievable by kinematic hardening models and indeed is physically more realistic. Here the finite element model describes effectively separate material components demonstrating once again its versatility.

Plastic behaviour characterized by irreversibility of stress paths and the development of permanent strain changes after a stress cycle can be described in a variety of ways. The more general model assumes a priori the existence of the incremental relationship

$$d\boldsymbol{\sigma}^e = \mathbf{D}^* d\boldsymbol{\varepsilon} \tag{F.22}$$

in which the matrix **D*** depends not only on the stress $\boldsymbol{\sigma}$ and on the state parameter κ but also on the direction of the applied stress (or strain) increment d$\boldsymbol{\sigma}$ (or d$\boldsymbol{\varepsilon}$). If we assume the dependence of **D*** only on two directions, those of loading and unloading, we can describe plastic loading by the sign of the projection $\boldsymbol{n}^T d\boldsymbol{\sigma}$. Thus $\boldsymbol{n}^T d\boldsymbol{\sigma} > 0$ for loading, $\boldsymbol{n}^T d\boldsymbol{\sigma} < 0$ for unloading while $\boldsymbol{n}^T d\boldsymbol{\sigma} = 0$ is the neutral direction in which only elastic straining occurs. We can now write that

$$d\boldsymbol{\sigma} = \mathbf{D}_L^* d\boldsymbol{\varepsilon} \quad \text{for loading} \tag{F.23}$$

$$d\boldsymbol{\sigma} = \mathbf{D}_U^* d\boldsymbol{\varepsilon} \quad \text{for unloading} \tag{F.24}$$

where the matrices $\mathbf{D}_L$* and $\mathbf{D}_U$* depend only on the state described by $\boldsymbol{\sigma}$ and $\boldsymbol{\kappa}$. The specification of $\mathbf{D}_L$* and $\mathbf{D}_U$* must be such that in the

neutral direction of the stress increment d$\boldsymbol{\sigma}$, the strain increments corresponding to this are equal. Thus we require

$$d\varepsilon = \mathbf{D}_L^{*\,-1} d\boldsymbol{\sigma} = \mathbf{D}_U^{*\,-1} d\boldsymbol{\sigma} \quad \text{when}$$

$$n^T d\boldsymbol{\sigma} = 0 \tag{F.25}$$

The most general way of achieving this end is to write

$$\mathbf{D}_L^{*\,-1} \equiv \mathbf{D}^{-1} + \frac{n_{gL} n^T}{H_L} \tag{F.26}$$

and

$$\mathbf{D}_U^{*\,-1} \equiv \mathbf{D}^{-1} + \frac{n_{gU} n^T}{H_U} \tag{F.27}$$

where $\mathbf{D}$ is the elastic matrix, $\mathbf{n}_{gL}$ and $\mathbf{n}_{gU}$ are arbitrary unit stress vectors for loading and unloading directions and H_L and H_U are appropriate plastic moduli which in general depend on $\boldsymbol{\sigma}$ and $\boldsymbol{\kappa}$. The value of the tangent matrices $\mathbf{D}_L$* and $\mathbf{D}_U$* can be obtained by direct inversion if $H_{L/U} \neq 0$, but more generally can be written as

$$\mathbf{D}_L^{*} \equiv \mathbf{D} - \mathbf{D} n_{gL} n^T (H_L + n^T \mathbf{D} n_{gL})^{-1} \tag{F.28}$$

with a similar form for D_U. This form resembles Equation (F.13)and indeed its derivation is almost identical. Thus if we put

$$\frac{n^T d\boldsymbol{\sigma}}{H_L} \equiv d\lambda \tag{F.29}$$

and write Equation (F.25) and (F.26) as

$$d\varepsilon = \mathbf{D}_L^{*\,-1} d\boldsymbol{\sigma} = \mathbf{D}^{-1} d\boldsymbol{\sigma} + \frac{n_{gL} n^T d\boldsymbol{\sigma}}{H_L} = \mathbf{D}^{-1} d\boldsymbol{\sigma} + n_{gL} d\lambda \tag{F.30}$$

we find that a form identical to that of Equation (F.11) is obtained and indeed the same elimination would suffice to obtain DL of expression (F.28). The general description of generalized plasticity allows:

(i) the full model to be specified by a direct prescription of n, n_g and H for loading and unloading at any point of the stress space,

(ii) existence of plasticity in both loading and unloading directions,

(iii) relative simplicity for description of experimental results when these are complex and the existence of a yield surface of the kind encountered in ideal plasticity is uncertain.

For the above reasons the generalized plasticity forms have proved extremely useful in describing the complex behaviour of soils. Here other descriptions using various interpolations of n and moduli from a unique yield surface, known as bounding surface plasticity models, are indeed particular forms of the above generalization and have proved useful. It is clear that classical plasticity is indeed a special case of the generalized models. Here the yield surface $F(\boldsymbol{\sigma}, \kappa)=0$ defines of course a unit vector normal to it as

$$n = \frac{\partial F / \partial \boldsymbol{\sigma}}{\left[(\partial F / \partial \boldsymbol{\sigma})^T (\partial F / \partial \boldsymbol{\sigma})\right]^{1/2}} \tag{F.31}$$

Similarly the plastic potential defines the unit vector n_g:

$$n_g = \frac{\partial Q / \partial \boldsymbol{\sigma}}{\left[(\partial Q / \partial \boldsymbol{\sigma})^T (\partial Q / \partial \boldsymbol{\sigma})\right]^{1/2}} \tag{F.32}$$

Substitution of such values for the unit vectors into Equation (F.28) will of course retrieve the original form of Equation (F.13). however, interpretation of generalized plasticity in classical terms is more difficult.

The success of generalized plasticity in practical applications has allowed many complex phenomena of soil dynamics to be solved.

Bibliography

Aagaard, B., Kientz, S., Knepley, M., Strand, L., Williams, C., (2008) PyLith User Manual, Version 1.3, *Computational Infrastructure for Geodynamics*.URL: www.geodynamics.org/cig/software /short/pylith/pylith_ book-1.3.pdf.

Acocella. V, Neri, M. (2005). Structural features of an active strike-slip fault on the sliding flank of Mt. Etna (Italy). *Journal of Structural Geology*, 27, 2, pp. 343-355.

Acocella V., B. Behncke, M. Neri, S. D'Amico (2003). Link between major flank slip and eruptions at Mt. Etna (Italy). *Geophys. Res.Lett.*, **30**, n. 24, 2286, doi:10.1029/2003GL018642.

AGIP S.p.A., 1977. Temperature Sotterranee. Grafiche Fili Brugora, Milano, pp. 1390.

Allard, D. Froidevaux, R.; Biver, P. (2006) Conditional Simulation of Multi-Type Non Stationary Markov Object Models Respecting Specified Proportions. *Mathematical Geology*, 38, 8, pp. 959-986.

Arevalo, C.M., Patanè, D., Rietbrock, A., Ibanez, J.M., 2005. The intrusive process leading to the Mt. Etna 2001 flank eruption: constraints from 3-D attenuation tomography. *Geophys. Res. Lett.* 32, doi:10.1029/2005GL023736.

Azzaro R, Mattia M, Puglisi G (2001) Dynamics of fault creep and kinematics of the eastern segment of the Pernicana fault (Mt. Etna,

Sicily) derived from geodetic observations and their tectonic significance. *Tectonophys* **333**:401–415

Balme, M.R.; Rocchi, V.; Jones, C.; Sammonds, P.R.; Meredith, P.G.; Boon, S. (2004). Fracture toughness measurements on igneous rocks using a high-pressure, high-temperature rock fracture mechanics cell, *J. Volcanol. Geotherm. Res*, 132, 2-3, pp. 159-172.

Battaglia, M., Segall, P., 2004. The interpretation of gravity changes and crustal deformation in active volcanic areas. *Pure Appl. Geophys*. 161, 1453–1467.

Battaglia, M., Segall, P., Murray, J., Cervelli, P., Langbein, J., 2003. The mechanics of unrest at Long Valley caldera, California: 1. Modeling the geometry of the source using GPS, leveling and two-color EDM data. *J. Volcanol. Geotherm. Res*. 127,195-217.

Berrino, G., Corrado, G., Luongo, G., Toro, B., 1984. Ground deformation and gravity changes accompanying the 1982 Pozzuoli Uplift. *Bull. Volcanol*., 47–52, 187–200.

Bonaccorso, A., Davis, P.M., 1999. Models of ground deformation from vertical volcanic conduits with application to eruptions of Mount St. Helens and Mount Etna. *Geophys. Res. Lett*. 104 (B5), 10531–10542.

Bonaccorso, A. and P.M. Davis, (2004): Modeling of Ground Deformation Associated with Recent Lateral Eruptions: Mechanism of Magma Ascent and Intermediate Storage at Mt. Etna. In: “Etna Volcano Laboratory”, Bonaccorso A., Calvari S., Coltelli M., Del Negro C., Falsaperla S. (Eds), *AGU (Geophysical monograph series)*, 293-306.

Bonaccorso, A., Aloisi, M.,Mattia, M., 2002. Dike emplacement forerunning the Etna July 2001 4 eruption modelled through continuous tilt and GPS data. *Geophys. Res. Lett*. 29 (13), 1624, doi:10.1029/5292001GL014397.

Bonaccorso, A., Davis, P.M. (2004). Modeling of ground deformation associated with recent lateral eruptions: mechanics of magma ascent and intermediate storage at Mt. Etna. In: Bonaccorso, A., Calvari, S., Coltelli, M., Negro, C.D., Falsaperla, S. (Eds.), Mount Etna Volcano Laboratory, vol. 143, *American Geophysical Union Monography Series*, p. 384.

Bonaccorso, A., Cianetti, S., Giunchi, C., Trasatti, E., Bonafede, M., Boschi, E., (2005). Analytical and 3D numerical modeling of Mt. Etna (Italy) volcano inflation. *Geophys. J. Int*. 163, 852–862.

Bonafede, M. and Rivalta, E., 1999b. On tensile cracks close to and across the interface between two welded elastic half spaces, *Geophys. J. Int.*, 138, 410–434.

Bonafede, M.,Dragoni, M., Quareni, F., 1986. Displacement and stress fields produced by a centre of dilatation and by a pressure source in a viscoelastic half-space: application to the study of round deformation and seismic activity at Campi Flegrei, Italy. *Geophys. J. R. Astron. Soc*. 87, 455–485.

Bonafede, M., Parenti, B., Rivalta, E., 2002. On strike-slip faulting in layered media. *Geophys. J. Int*. 149, 698–723.

Bonforte, A., S. Gambino, F. Guglielmino, F. Obrizzo, M. Palano, G. Pugliesi (2007). Ground deformation modeling of flank dynamics prior to the 2002 eruption of Mt Etna, *Bull Volcanol*. 69: 757-768.

Bonforte, A., S. Gambino, F. Guglielmino, F. Obrizzo, M. Palano, and G. Puglisi, "Ground deformation modeling of flank dynamics prior to the 2002 eruption of Mt. Etna," *Bull. Volcanol*. 69, 757–768, DOI: 10.1007/s00445-006-0106-1, 2007b.

Bürgmann, R., P. Segall, M.Lisowski, and J. Svarc, Postseismic starin following the 1989 Loma Prieta earthquake from GPS and leveling measurements, *J. Geophys. Res.*, *102*, 4933-4955, 1997

Carbone, D., Currenti, G., Del Negro, C., 2007. Elastic model for the gravity and elevation changes 19 before the 2001 eruption of Etna volcano. *Bull. Volcanol*. 69, 553–562, doi:10.1007/s00445-006-0090-5.

Cayol, V., Cornet, H.C., 1998. Effects of topography on the interpretation of the deformation field of prominent volcanoes—application to Etna. *Geophys. Res. Lett*. 25, 1979–1982.

Cheng, C.H., Johnston, D.H., 1981. Dynamic and static moduli. *Geophys. Res. Lett*., 8, 1, 39-42.

Chiarabba, C., Amato, A., Boschi, E., Barberi, F., 2000. Recent seismicity and tomographic modeling of the Mount Etna plumbing system. J. Geophys. Res. 105, 10923–10938.

Christensen, R.M., 1971. Theory of Viscoelasticity: An Introduction. Academic Press, New York.

Christensen, R.M., 1982. Theory of Viscoelasticity: An Introduction. *Academic San Diego Calif*, pp. 364.

Ciccotti, M. and Mulargia, F. (2004) Differences between static and dynamic elastic moduli of a typical seismogenic rock. *Geophysical Journal International*, 157, 1, pp. 474-477.

Civetta, L., D'Antonio, M., De Lorenzo, S., Di Renzo, V., Gasparini, P., 2004. Thermal and geochemical constraints on the 'deep' magmatic structure of Mt. Vesuvius. *J. Volcanol. Geotherm. Res*. 133, 1–12.

Cloetingh, S., Boldreel, L.O.; Larsen, B.T.; Heinesen, M.; Mortensen, L. (1998). Tectonics of sedimentary basin formation: models and constraints. *Tectonophysics*, 300, 1-4, pp. 1-11

Comsol Multiphysics 3.3, 2008. Comsol AB, Stockholm, Sweden.

Corsaro, R. & Pompilio, M., 2003. Buoyancy-controlled eruption of magmas at Mt Etna, *TerraNova*, 16, 16–22.

Currenti, G., Del Negro, C., Fortuna, L., Ganci, G., 2007a. Integrated inversion of ground deformation and magnetic data at Etna volcano using a genetic algorithm technique. *Ann. Geophys*. 50 (1), 21–30.

Currenti, G., Del Negro, C., Ganci, G., 2007b. Modeling of ground deformation and gravity fields using finite element method: an application to Etna volcano. *Geophys. J. Int*., doi:10.1111/j.1365-246X.2007.03380.x.

Currenti, G., Del Negro, C., Ganci, G., Scandura, D., 2008a. 3D numerical deformation model of the intrusive event forerunning the 2001 Etna eruption. *Phys. Earth Planet. Interiors*, doi:10.1016/j.pepi.2008.05.004.

Davis, P. M., 1986. Surface deformation due to inflation of an arbitrarily oriented triaxial ellipsoidal cavity in an elastic half-space, with reference to Kilauea Volcano, Hawaii. *J. Geophys. Res.* 91, 7429–7438.

De Gori, P., Chiarabba, C., Patanè, D., (2005). Qp structure of Mt. Etna: constraints for the physics of the plumbing system. *J. Geophys. Res.* 110, doi:10.1029/2003JB002875.

Del Negro, C, Currenti, G., Scandura, D. (2009). Temperature-dependent viscoelastic modeling of ground deformation: Application to Etna volcano during the 1993–1997 inflation period. *Phys. Earth Planet. Interiors*, 172, 3-4, pp. 299-309.

Dokka, R. K., and C. J. Travis (1990). Role of eastern California shear zone in accommodating Pacific–North America plate motion, *Geophys. Res. Lett.* 17, No. 9, 1323–1326.

Dragoni, M., Magnanensi, C., (1989). Displacement and stress produced by a pressurized, spherical magma chamber, surrounded by a viscoelastic shell. *Phys. Earth Planet. Interiors* 56, 316–328.

Dragoni, M., Harabaglia, P., Mongelli, F., (1997). Stress field at a transcurrent plate boundary in the presence of frictional heat production at depth. *Pure Appl. Geophys*. 150, 181–201.

Drucker, D. C., (1951). A more fundamental approach to plastic stress-strain relations. *Proc. First US Congress of Applied Mechanincs*, ed. ASME, New York.

Edelsbrunner, H., (2001). Geometry and topology for mesh generation. Cambridge, ISBN: 0-521-79309-2, LC: QA377.E36.

Fernández, J., Yu, T.-T., Rundle, J.B., (1996b). Horizontal viscoelastic-gravitational displacement due to a rectangular dipping thrust fault in a layered Earth model. *Journal of Geophysical Research* 101, 13,581-13,594 (correction in Journal of Geophysical Research 103 (B12), 30283-30286, 1998).

Fernández, J., Tiampo, K.F., Rundle, J.B., 2001. Viscoelastic displacement and gravity changes due to point magmatic intrusions in a gravitational layered solid earth. *Geophys. J. Int*. 146, 155–170.

Fialko, Y. (2004b) Probing the mechanical properties of seismically active crust with space geodesy: Study of the co-seismic deformation due to the 1992 Mw7:3 Landers (southern California) earthquake. *Journal of Geophysical Research.*

Field, D., 2000. Qualitative measures for initial meshes. Int. J. Numer. Methods Eng. 47, 887–906.

Folch, A., Fernàndez, J., Rundle, J.B., Martì, J., 2000. Ground deformation in a viscoelastic medium composed of a layer overlying a half-space: a comparison between point and extended sources. *Geophys. J. Int*. 140, 37–50.

Freed, A. M., and J. Lin (2001). Delayed triggering of the 1999 Hector Mine earthquake by viscoelastic stress transfer, Nature 411, 180–183.

Freed, A., F., Burgmann, R., Herring, T. (2007). Far-reaching transient motions after Mojave earthquakes require broad mantle flow beneath a strong crust. *Geoph. Res. Lett*., 34, L19302, doi:10.1029/2007GL030959.

Fukahata, Y. and Wright, T. J., 2008. A non-linear geodetic data inversion using ABIC for slip distribution on a fault with an unknown dip angle, *Geophysical Journal International*, 173, 2, 353-364

Fung, Y.C., 1965. Foundations of Solid Mechanics. Prentice-Hall, Englewood Cliffs.

Fung, Y. C. (1977). *A First Course in Continuum Mechanics* (2nd edition ed.). Prentice-Hall, Inc.

Gabriel, A.K., Goldstein, R.M. and Zebker, H.A. (1989). Mapping Small Elevation Changes Over Large Areas: Differential Radar Interferometry, *Journal of Geophysical Research*, Vol. 94, No.B7, pp.9183-9191.

Gill, P. E., Murray, W., Wright, H., M., (1981). Practical Optimization, Academic Press, London.

Haimson, B. C., Rummel, F., (1982). Hydrofracturing stress measurements in the Iceland research drill hole at Reydarfjördur, Iceland, *Journal of Geophysical Research* 87, 6631–6649.

Hauksson, E., L. M. Jones, and K. Hutton (2002). The 1999 Mw 7.1 Hector Mine, California, earthquake sequence: complex conjugate strike-slip faulting, *Bull. Seism. Soc. Am.* 92, 1154–1170.

Ivins, E. R., Sammis, C.G., (1996). Transient creep of a composite lower crust. *J. Geophys. Res*. 101 (B12), 27981–28004.

Jaeger J. Cook, G. W., Zimmerman, R., (2007). Fundamentals of rock mechanics, Backwell.

Johnson K. M., Hsu, Y-J., Segall, P., Yu, S-B., (2001). Fault geometry and slip distribution of the 1999 Chi-Chi, Taiwan earthquake imaged from inversion of GPS data, *Geoph. Res. Lett*., 28,11, 2285-2288.

Kearey, P., Brooks, M., (1991). An introduction to geophysical exploration, second edition. Blackwell Scientific Publications, Oxford, 254.

Lanari, R., Lundgren, P. and Sansosti, E. (1998). Dynamic Deformation of Etna Volcano Observed by Satellite Radar Interferometry, *Geophys. Res. Lett.*, 25, 10, pp.1541-1544.

Lo Giudice, E., Rasà, R., (1992). Very shallow earthquakes and brittle deformations in active volcanic areas: the Etnean region as an example. *Tectonophysics*, 202, 257-268.

Lundgren, P., Berardino, P., Coltelli, M., Fornaro, G., Lanari, R., Puglisi, G., Sansosti, E., Tesauro, M., (2003). Coupled magma chamber inflation and sector collapse slip observed with synthetic aperture radar interferometry on Mt. Etna volcano. *J. Geophys. Res.* 108 (B5), 2247, doi: 10.1029/2001JB000657.

Massonet, D., Briole, P. and Arnaud, A. (1995) Deflation of Mount Etna Monitored by Spaceborne Radar Interferometry, *Nature*, 375, pp.567-570.

Masterlark, T., *J.*, (2003) *Geophys. Res.* 108, doi: 10.1029/2002JB002296.

McTigue, D. F., (1986). Thermoelastic response of fluid-saturated porous rock. *J. Geophys. Res.* 91, 9533–9542.

McTigue, D. F., (1987). Elastic stress and deformation near a finite spherical magma body: resolution of the point source paradox. *J. Geophys. Res.* 92, 12931–12940.

Megna, A., S. Barba, S. Santini, and M. Dragoni, (2008). Effects of geological complexities on coseismic displacement : hints from 2D numerical modeling, *Terra Nova*, 20, 173-179.

Mogi, K., (1958). Relations between the eruptions of various volcanoes and the deformations of the ground surfaces around them. *Bull. Earthq. Res. Inst.*, Univ. Tokyo 36, 99–134.

Murase, M., Irwan, M., Kariya, S., Tabei, T., Okuda, T.,Miyajima, R., Oikawa, J.,Watanabe, H., Kato, T., Nakao, S., Ukawa, M., Fujita, E., Okayama, M., Kimata, F., Fujii, N., (2006). Time dependent model of magma intrusion in and around Miyake and Kozu Islands, Central Japan in June-August 2000. *J. Volcanol. Geother. Res.* 150, 213–231.

Musumeci, C., Cocina, O., De Gori, P., Patane´ , D., (2004). Seismological evidence of stress induced by dike injection during the 2001 Mt. Etna eruption. *Geophys .Res. Lett.*, 31, doi: 10.1029/2003GL019367.

Napoli, R., Currenti, G., Del Negro, C., Greco, F., Scandura, D. (2008). Volcanomagnetic evidence of the magmatic intrusion on 13th May 2008 Etna eruption, *Geophys .Res. Lett*, 35, LXXXXX, doi: 10.1029/2008GL035350.

Neri, M., Acocella, V., & Behncke, B. (2003). The role of the pernicana Fault System in the spreading of Mt. Etna (Italy) during the 2002-2003 eruption. *Bulletin of Volcanology*, 66, 417-430.

Newman, A.V., Dixon, T., Ofoegbu, G., Dixon, J., (2001). Geodetic data constraints on recent activity at Long Valley Caldera. California: evidence for viscoelastic rheology. *J. Volcanol. Geotherm. Res.* 105, 183–206.

Newman, A.V., Dixon, T.H., Gourmelen, N., (2006). A four-dimensional viscoelastic deformation model for Long Valley Caldera, California, between 1995 and 2000. *J. Volcanol. Geotherm. Res.* 150, 244–269.

Obrizzo, F., Pingue, F., Troise, C., De Natale, G., (2004). Bayesian inversion of 1994–98 vertical displacements at Mt. Etna; evidence

for magma intrusion. *Geophys. J. Int*. 157 (2), 935–946, doi:10.1111/j.1365-246X.2004.02160.x.

Okada, Y., Yamamoto, Y., (1991). Dyke intrusion model for the 1989 seismovolcanic activity of Off Ito, *Central Japan. J. Geophys. Res*. 96, 10361–10376.

Okada, Y., (1985): Surface deformation due to shear and tensile faults in a half-space. *Bull. Seism. Soc. Am.* 75, 1135-1154.

Okada, Y., (1992). Internal deformation due to shear and tensile faults in a half-space. *Bull. Seism. Soc. Am.* 82, 1018–1040.

Palano, M., M. Aloisi, M. Amore , A. Bonforte , F. Calvagna, M. Cantarero, O. Consoli, S. Consoli, F. Guglielmino, M. Mattia, B. Pugliesi and G. Puglisi, (2006). Kinematics and strain analyses of the eastern segment of the Pernicana Fault (Mt. Etna, Italy) derived from geodetic techniques (1997-2005), *Ann. Geophys*., 49, 4/5,1019-1032.

Parsons, T., and D. Dreger (2000). Static-stress impact of the 1992 Landers earthquake sequence on nucleation and slip at the site of the 1999 *M* 7.1 Hector mine earthquake, southern California, *Geophys. Res. Lett.* 27, 1949–1952.

Patane`, D., Chiarabba, C., Cocina, O., De Gori, P., Moretti, M., Boschi, E., (2002). Tomographic images and 3D earthquake locations of the seismic swarm preceding the 2001 Mt. Etna eruption: Evidence for a dyke intrusion. *Geophys. Res. Lett*. 29 (10), 1497, doi: 10.1029/2001GL014391.

Patanè, D., De Gori, P., Chiarabba, C., Bonaccorso, A., (2003). Magma ascent and the pressurization of Mount Etna's volcanic system, *Science*, 299, 2061-2063

Patanè, D., Barberi, G., Cocina, O., De Gori, P., Chiarabba, C., (2006). Time-resolved seismic tomography detects magma intrusions at Mount Etna. *Science* 313, 821–823.

Peltier, W. R., (1974). The impulse response of a Maxwell earth. *Rev. Geophys. Space Phys*. 12, 649–669.

Piombo, A., Tallarico, A., Dragoni, M., (2007). Displacement, strain and stress fields due to shear and tensile dislocations in a viscoelastic half-space. *Geophys. J. Int*., doi:10.1111/j.1365-246X.2007.03283.x.

Pritchard, M. E., M. Simons, P. A. Rosen, S. Hensley, and F. H. Webb, (2002). Co-seismic slip from the 1995 July 1995 30 Mw = 8.1 Antofagusta, Chile, earthquake as constrained by InSAR and GPS observations, *Geophys. J. Int.*, 150, 362–376.

Ranalli, G., (1995). Rheology of the Earth. Chapman and Hall, London, pp. 413.

Rasà, R., Azzaro, R., Leonardi, O., (1996). Aseismic creep on faults and flank instability at Mt. Etna volcano. In: McGuire, W.J., Jones, A.P., Neuberg, J. (Eds.), *Volcano Instability on the Earth and Other Planets. Geol. Soc. Spec. Publ*., vol. 110, pp. 179–192.

Rosen, P., S. Henley, G. Peltzer, and M. Simons (2004), Update Repeat Orbit Interferometry Package Released, *Eos Trans. AGU*, 85(5), 47.

K. Rybicki, (1986). Displacements and stresses in an anisotropic medium due to non-uniform slip along a very long strike-slip fault, *Continuum Theories in solid Earth Physics*, Tesseyre, R., PWH-Polish Scientific Publishers, Warsaw, pp. 18-175.

Sansosti, E., Lanari, R. and Lundgren, P. (1998). Dynamic Deformation of Etna Volcano Observed by *Satellite Radar Interferometry*, Proceedings of IGARSS '98, Seattle, USA, pp.8113.8127.

Sato, R., (1971). Crustal deformation due to dislocation in a multi-layered medium, *J. Phys. Earth*, 19, 29-46.

Sato, R., Matsu'ura, M., (1973). Static deformation due to the fault spreading over several layers in a multi-layered medium. Part I: displacement. *Journal of Physics of the Earth* 21, 227-249.

Sauber, J., Thatcher, W. and Solomon, S. C. (1986). Geodetic measurements of deformation in the central Mojave Desert, California, J. Geophys. Res. 91, 2683–2693.

Schultz, R. A., (1995). Limits of strength and deformation properties of jointed basaltic rock masses, Rock Mechanics and Rock Engineering 28, 1–15.

Scientists of the U.S. Geological Survey, Southern California Earthquake Center, and the California Division of Mines and Geology (2000). Preliminary report on the 16 October 1999 M 7.1 Hector Mine, California, earthquake, *Seism. Res. Lett*. 71, 11–23.

Strozzi, T., Wegmüller, U.,Werner, Ch. And Wiesmann, A., (2000). Measurement of Slow Uniform Surface Displacement with mm/year Accuracy, *Proceedings of IGARSS'00*, Hawaii, USA, pp.2239-2241.

Trasatti, E., Giunchi, C., Bonafede, M., (2003). Effects of topography and rheological layering on ground deformation in volcanic regions. *J. Volcanol. Geotherm*. Res. 122, 89–110.

Treiman, J. A., K. J. Kendrick, W. A. Bryant, T. K. Rockwell, and S. F. McGill (2002). Primary surface rupture associated with the *M*w 7.1 16 October 1999 Hector Mine earthquake, San Bernardino County, California, *Bull. Seism. Soc. Am.* 92, 1171–1191 Truesdell, C., 1952, *The Mechanical foundations of elasticity and fluid dynamics*, Journal of Rational Mechanics and Analysis, vol. 1, pages 125–300.

Turcotte, D. L., Schubert, G., (1982). Geodynamics-Applications of Continuum Physics to Geological Problems. Wiley, New York.

Voight, B., Hoblitt, R.P., Clarke, A.B., Lockhart, A.B., Miller, A.D., Lynch, L., (1998). Remarkable cyclic ground deformation monitored in real time on Montserrat and its use in eruption forecasting. *Geophys. Res. Lett*., 25, 3405–3408.

Wald, D. J., and T. H. Heaton (1994). Spatial and temporal distribution of slip for the 1992 Landers, California, earthquake, *Bull. Seismol. Soc. Am.*, 84, 668– 691.

Walsh, J.B., Decker, R.W., (1971). Surface deformation associated with volcanism. *J. Geophys. Res*. 76, 3291–3302.

Wang, H. F., and M. P. Anderson (1982). Introduction to Groundwater Modeling: Finite Difference and Finite Element Methods, 237 pp., *Academic*, San Diego, Calif..

Wang, R., Martin, F.L., Roth, F., (2003). Computation of deformation induced by earthquakes in a multi-layered elastic crust-FORTRAN programs EDGRN/EDCMP. *Computer Geosci*, 29, 195–207.

Williams, C. A., Wadge, G., (2000). An accurate and efficient method for including the effects of topography in three-dimensional elastic

models of ground deformation with applications to radar interferometry. *J. Geophys. Res*. 105, 103–8120.

Williams, C.A., (2006). Development of a package for modeling stress in the lithosphere, *Eos Trans. AGU*, 87 (36), Jt. Assem. Suppl., Abstract T24A-01.

Yang, X., Davis, P.M., (1986). Deformation due to a rectangular elastic tension crack in an elastic half-space. *Bull. Seismol. Soc*. Am. 76, 865–881.

Yang, X., Davis, P.M., Delaney, P.T., Okamura, A.T., (1992). Geodetic analysis of dike intrusion and motion of the magma reservoir beneath the summit of Kilauea volcano, Hawaii: 1970–1985. J. *Geophys. Res*. 97, 3305–3324.

Zebker, H. A. and Goldstein, R. M. (1986). Topographic Mapping from Interferometric Synthetic Aperture Radar Observations, *Journal of Geophysical Research*, Vol.91, No. B5,pp. 4993-4999.

Zebker, H. A., Rosen, P. A, GoldStein, R., M., Gabriel, A., Werner, C. L. (1994). On the derivation of coseismic displacement fields using differential radar interferometry: the Landers earthquake. *International Journal of Rock Mechanics and Mining Sciences & Geomechanics*, 32, 5, pp. 206A-207A.

Zhao, S., Muller, R. D., Takahashi, Y., Kaneda, Y. (2004), 3-D finite-element modeling of deformation and stress associated with faulting: effect of inhomogeneous crustal structures. *Geophys. J. Int.*, 157, 629–644 doi: 10.1111/j.1365-246X.2004.02200.x

Zienkiewicz and Taylor, 1998. The Finite Element Method. McGraw-Hill, London.

Dissemination

This thesis collects theoretical investigations and experimental results disseminated via national and international conferences as well as peer reviewed journals; here after is presented the list of scientific publications whose content is subject of this doctoral Thesis.

International Journals

Currenti, G., Del Negro, C., **Scandura**, D. (2007). 3D numerical deformation model of the intrusive event forerunning the 2001 Etna eruption, *PEPI*, 168, 88-96.

Currenti, G., Del Negro, C., **Scandura**, D. (2008). Thermal-mechanical modeling of ground deformation in a viscoelastic medium: application to etna volcano during the 1993-1997 inflation period, *PEPI*.

Napoli, R., Currenti, G., Del Negro, C., Greco, F., **Scandura**, D. (2008). Volcanomagnetic evidence of the magmatic intrusion on 13th May 2008 Etna eruption, *Geophysical Research Letters*, 35, LXXXXX, doi:10.1029/2008GL035350.

Greco, F., Currenti, G., Del Negro, C., Napoli, R., **Scandura**, D., Budetta, G., Fedi, M., Boschi, E. (2008). Temporal gravity

tomography to look deep into the southern flank of Etna volcano, *J. Geophys. Res.*, submitted.

Currenti, G., Bonaccorso, A., Del Negro, C., Guglielmino, F., **Scandura**, D., Boschi, E. (2009). FEM-based inversion for heterogeneous fault mechanisms: application at Etna volcano by DInSAR data, *Geophysical Journal International*, minor revision.

Currenti, G., Bonaccorso, A., Del Negro, C., **Scandura**, D., Boschi, E. (2009). Elastoplastic modeling of volcano ground deformation, *EPSL*, submitted.

Monographies

Currenti, G., Del Negro, C., Ganci, G., **Scandura**, D. (2007). 3D numerical deformation model of the intrusive event forerunning the 2001 Etna eruption, UFGM Monograph Series, Unità Funzionale Gravimetria e Magnetismo, INGV-CT, 2006 Annual Report.

Currenti, G., **Scandura**, D. (2007). Thermal-mechanical coupling for modeling round deformation in a viscoelastic medium, UFGM Monograph Series, Unità Funzionale Gravimetria e Magnetismo, INGV-CT, 2006 Annual Report.

International Conferences

Currenti, G., Del Negro, C., Ganci, G., **Scandura**, D. (2007). Coulomb stress changes at Etna volcano calculated from three

dimensional finite element model, *5th* International Workshop on Statistical Seismology: Physical and Stochastic Modeling of Earthquake Occurrence and Forecasting (EMFCSC), Erice, 31 May - 6 June (poster session).

Scandura, D., Currenti, G., Del Negro, C., Ganci, G. (2007). 3D Finite Element Models of Ground Deformation and Stress Field in a Viscoelastic Medium, European Comsol Conference, Grenoble, 23-24 October (poster session).

Currenti, G., Del Negro, C., Ganci, G., **Scandura**, D. (2007*).* Thermal-mechanical modeling of ground deformation and stress field in a viscoelastic medium, Cities on Volcanoes 5, Shimabara, 22 November (poster session).

Greco, F., Currenti, G., Del Negro, C., **Scandura**, D., Ganci, G., Napoli, R., Budetta, G., Fedi, M., Boschi, E.(2007). Review of discrete gravity measurements along a 24-kilometer East - West trending profile of 19 stations on the southern slope of the Etna volcano: 1994-2007, GNGTS, Rome, 13-15 November, (oral presentation).

Napoli, R., Del Negro, C., Ganci, G., Giudice, S., Currenti, G., Greco, F., **Scandura**, D., Boschi, E., (2007). Magnetic variations observed at Stromboli Island before and during the 2007 eruption, GNGTS, Rome, 13-15 November, (oral presentation).

Scandura, D., Currenti, G., Del Negro, C. (2007). 3D Finite Element Models of Ground Deformation and Stress Field in a Viscoelastic Medium, Grid Open Days all'Università di Palermo, Palermo, 6-7 December, (poster session).

Scandura, D. (2008). Thermal-mechanical modeling of ground deformation in a viscoelastic medium: application to Etna volcano during the 1993-97 inflation period, INGV Grid Open Days, Catania, 2 April, (oral presentation).

Scandura, D., Currenti, G., Del Negro, C., Ganci, G. (2008). Thermal viscoelastic modeling of ground deformation at Etna volcano, IAVCEI, 18-22 August, (oral presentation).

Scandura, D., Currenti, G., Del Negro, C. (2008). Thermo-mechanical modeling of ground deformation in volcanic areas, SIMAI, Rome, 15-19 September, (oral presentation).

Napoli, R., Currenti, G., Del Negro, C., Greco, F., **Scandura**, D., Sicali, A. (2008). Etna volcano erupts again on 13 may 2008: and magnetic field monitoring is a key part of the picture, GNGTS, Trieste, 6-8 October (oral presentation).

Scandura, D., Currenti, G., Del Negro, C. (2008). 3D finite element models of ground deformation and stress field in a viscoelastic medium, European Comsol Conference, Hannover, 4-6 November, (poster session)

Currenti, G., Del Negro, C., **Scandura**, D., Williams, C. (2008). Automated procedure for InSAR data inversion using Finite Element Method, USEReST, Naples, 11-14 November, (oral presentation).

Scandura, D., Bonaccorso, A., Currenti, G., Del Negro, C., (2008). Effects of rheological behavior on ground deformation during the 1993-1997 inflation period at Etna volcano: insights from thermo-mechanical model, AGU Fall Meeting, San Francisco, 15-19 December, (oral presentation).

Scandura, D., Bonaccorso, A., Currenti, G., Del Negro, C., (2009). Elastoplastic modeling of 1993-97 inflation period at Mt Etna , EGU General Assembly, Vienna, 19-24 April, (oral presentation).

Currenti, G., Del Negro, C., **Scandura**, D., (2009). An InSAR ground deformation inversion scheme using a FEM-based fault slip model: an application to Etna volcano, IEEE International Geoscience and Remote Sensing Symposium, Cape Town, 12-17 July, (oral presentation).

Scandura, D., Bonaccorso, A., Currenti, G., Del Negro, C., (2009). Thermo-mechanical of ground deformation in volcanic areas, Physcon, Catania, 1-4 September, (oral presentation).

Currenti, G., Del Negro, C., **Scandura**, D., Williams, C., (2009). Ground Deformation Inversion Scheme Using A 3d Fem-Based Model: An Application To Etna Volcano, Physcon, Catania, 1-4 September, (oral presentation).

Napoli, R., Currenti, G., Di Stefano, A., Greco, F., **Scandura**, D., Del Negro, C. (2009). Integrated modeling of geophysical observations at Etna volcano, Physcon, Catania, 1-4 September, (oral presentation).

Greco, F., Currenti, G., Di Stefano, A., Napoli, R., Pistorio, A., **Scandura**, D., Budetta G., Fedi, M. (2009). Wavelet multi-resolution analysis for the local separation of microgravity anomalies at Etna volcano, Physcon, Catania, 1-4 September, (oral presentation).

Scandura, D., Bonaccorso, A., Currenti, G., Del Negro, C., (2009). 3D finite element analysis of long-term deformation after Mojave

earthquakes inferred from InSAR and GPS observations, GNGTS, Trieste, 16-19 November, (oral presentation).